ZBP1 sequesters cGAS in the cytoplasm and sustains type I interferon responses to mitochondrial DNA

Yuanjiu Lei[1], Jordyn J. VanPortfliet[1], Yi-Fan Chen[1], Joshua D. Bryant[1], Katherine B. Ragan[2], Carl W. Tong[3,4], Laura Ciaccia West[1], Marcus W. Bosenberg[5], Pingwei Li[6], Gerald S. Shadel[7], Jason W. Upton[8], and A. Phillip West[1*]

[1]Department of Microbial Pathogenesis and Immunology, College of Medicine, Texas A&M University, Bryan, TX, USA

[2]Department of Molecular Biosciences, University of Texas at Austin, Austin, TX, USA

[3]Department of Medical Physiology, College of Medicine, Texas A&M University, Bryan, TX, USA

[4]Heart Failure and Coumadin Clinic, CHI St. Joseph Health, Bryan, TX, USA

[5]Departments of Pathology, Dermatology, and Immunobiology, Yale School of Medicine, New Haven, CT, USA

[6]Department of Biochemistry and Biophysics, Texas A&M University, College Station, TX, USA

[7]Salk Institute for Biological Studies, La Jolla, CA, USA

[8]Department of Biological Sciences, Auburn University, Auburn, AL, USA

* Correspondence to: awest@tamu.edu

23 **Graphical abstract**

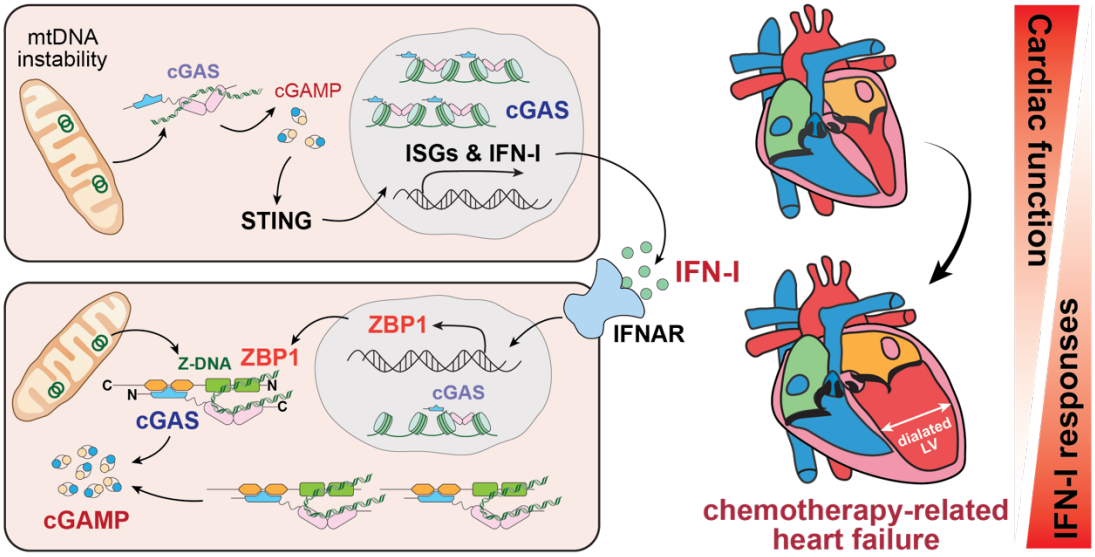

24

SUMMARY

Mitochondrial DNA (mtDNA) is a potent agonist of the cyclic GMP-AMP (cGAMP) synthase (cGAS) – Stimulator of Interferon Genes (STING) – type I interferon (IFN-I) pathway. However, the kinetics of mtDNA detection by cGAS or other nucleic acid sensors and the exact immunostimulatory features of mtDNA remain poorly defined. Here, we show that robust and sustained IFN-I responses downstream of mtDNA stress require the nucleic acid sensor Z-DNA binding protein 1 (ZBP1) in a cell death independent manner. Cells experiencing persistent mtDNA release display robust ZBP1 expression, as well as a marked increase in the cytoplasmic pool of cGAS. Biochemical and microscopy analyses reveal that the receptor-interacting protein homotypic interaction motifs (RHIMs) of ZBP1 bind the N-terminus of cGAS, leading to its entrapment in the cytoplasm. Moreover, we show that genetic and pharmacologic induction of mtDNA stress leads to the mitochondrial and cytoplasmic accumulation of Z-form DNA. Nuclease treatment or deletion of Z-DNA binding domains of ZBP1 reduce its interaction with cGAS and impair cGAMP production downstream of mtDNA stress. Finally, we uncover that ZBP1 is a novel regulator of IFN-I-mediated disease pathology, working in tandem with the cGAS-STING pathway to sense mtDNA instability and sustain IFN-I signaling that contributes to cardiac remodeling and heart failure. These results provide new insight into the molecular mechanisms of mtDNA sensing by the innate immune system and reveal that ZBP1 is a cooperative partner for cGAS. Moreover, our findings highlight ZBP1 as a potential therapeutic target in heart failure and other disorders where mtDNA instability drives disease-promoting IFN-I and inflammatory responses.

46 **INTRODUCTION**

47 The cGAS-STING axis is now recognized as key sensor of endogenous DNA and a major
48 driver of IFN-I and inflammatory responses in human disease (Decout et al., 2021; Lepelley et al.,
49 2021a; Riley and Tait, 2020; West, 2017; West and Shadel, 2017; Zierhut and Funabiki, 2020).
50 Although initially proposed as a cytoplasm-restricted sensor, several elegant studies reported that
51 cGAS is predominantly a nuclear protein (Volkman et al., 2019) that is tightly bound to chromatin
52 (Boyer et al., 2020; Cao et al., 2020; Kujirai et al., 2020; Michalski et al., 2020; Pathare et al.,
53 2020; Zhao et al., 2020). Nuclear import and export sequences in cGAS have been identified
54 (Gentili et al., 2019; Sun et al., 2021), and post-translational modifications and protein-protein
55 interactions have also been shown to regulate cGAS distribution during cell division, cancer, and
56 viral infection (Lahaye et al., 2018; Li et al., 2021; Liu et al., 2018). Although cGAS senses
57 cytosolic mtDNA and triggers IFN-I (Rongvaux et al., 2014; West et al., 2015; White et al., 2014),
58 whether cGAS re-localizes in response to mtDNA stress remains unclear. Moreover, the
59 mechanisms that sustain cGAS activity toward mtDNA in conditions of persistent cytosolic release
60 are not well understood.

61 In addition to cGAS, several other DNA sensors have been implicated in the detection of
62 mtDNA. For example, interferon gamma inducible protein 16 (IFI16) can sense mtDNA that is
63 insufficiently degraded in lysosomes, leading to elevated IFN-I responses that promote
64 cytotoxicity and Parkinson's disease phenotypes in vivo (Matsui et al., 2021). IFI16 was also
65 shown to interact with and potentiate cGAS activity in certain cellular contexts (Almine et al.,
66 2017; Jønsson et al., 2017). Moreover, the nucleic acid sensor ZBP1 has been reported to bind to
67 cytosolic mtDNA during necroptosis and trigger pro-inflammatory responses during oxidative
68 stress in vitro (Chen et al., 2018; Szczesny et al., 2018). However, the mtDNA ligand specificity

69 of ZBP1 and the physiological relevance of mtDNA sensing by ZBP1 in vivo remain unclear. In
70 addition, whether ZBP1 works independently of or in concert with cGAS to sustain IFN-I and/or
71 inflammatory signaling downstream of mtDNA release is a key open question.

72 Type I interferons (IFN-I) are pleotropic cytokines that function in antimicrobial immunity,
73 tumor immunity, and metabolic regulation. However, persistent and unrestrained IFN-I signaling
74 is linked to autoimmune diseases, type I interferonopathies, and organ system failure (Crow and
75 Stetson, 2021; Lei et al., 2021; McNab et al., 2015; Wu et al., 2016; Yu et al., 2022). We recently
76 reported that mtDNA instability and chronic activation of cGAS-STING-IFN-I signaling
77 potentiate age-related tissue pathology in the polymerase gamma (POLG) mutator model of
78 mtDNA disease (Lei et al., 2021). Elevated expression of ZBP1 and interferon-stimulated genes
79 (ISGs) were detected in the heart and other organs of POLG mutator mice compared to WT
80 littermates. Notably, ablation of IFN-I signaling dramatically reduced the development of age-
81 related cardiomyopathy in these mice, suggesting that the cGAS-STING-IFN-I axis contributes to
82 heart failure induced by mtDNA instability and mitochondrial dysfunction (Lei et al., 2021).
83 Studies in other pre-clinical models have linked mtDNA sensing by cGAS or Toll-like receptor 9
84 to heart failure after ischemic injury and myocardial infarction (Cao et al., 2018; King et al., 2017;
85 Nakayama and Otsu, 2018; Oka et al., 2012; Zhang et al., 2015). However, the mechanisms
86 governing IFN-I-mediated cardiac damage and the role of additional mtDNA sensors in promoting
87 heart failure are unclear.

88 Anthracycline chemotherapeutic regimens, including Doxorubicin (Doxo) and epirubicin,
89 are leading causes of cancer therapy-related heart failure, and despite numerous cardiovascular
90 side effects, the widespread use of these agents has persisted for over fifty years due to their
91 potency against a number of solid tumors and hematologic malignancies (Lipshultz et al., 2013;

92 Mehta et al., 2018; Vejpongsa and Yeh, 2014; Volkova and Russell, 2011). In fact, a majority of
93 adult breast and childhood cancer patients receive Doxo or another anthracycline, highlighting the
94 large number of individuals at risk for cardiotoxicity (Giordano et al., 2012; Lindsey et al., 2014;
95 Mancilla et al., 2019; Nathan et al., 2016). Anthracyclines can cause arrhythmia, myocarditis,
96 cardiomyopathy, and congestive heart failure, and symptoms can manifest immediately or years
97 after treatment (Moudgil and Yeh, 2016; Raj et al., 2014). Although risk factors such as underlying
98 cardiovascular disease, female gender, and young or old age have been identified (Burridge et al.,
99 2016; Meléndez et al., 2018; Vejpongsa and Yeh, 2014), at present, it remains impossible to predict
100 which patients will experience Doxorubicin-induced cardiotoxicity (DIC), or to adequately protect
101 at-risk patients. Thus, there is an urgent need to advance mechanistic understanding of DIC to
102 illuminate novel therapeutic avenues for afflicted patients. The molecular and cellular mechanisms
103 responsible for DIC remain elusive, although mitochondrial dysfunction and mtDNA damage are
104 hypothesized to be major drivers of cardiotoxicity (Berthiaume and Wallace, 2007; Carvalho et al.,
105 2014; Serrano et al., 1999; Wallace et al., 2020; Yen et al., 1999; Zhou et al., 2001). Elevated
106 levels of cardiac pro-inflammatory cytokines (i.e. TNFα, IL-6, and IL-1β) have been observed in
107 some rodent DIC models (Frantz et al., 2018); however, the cardiac innate immune ligands,
108 receptors, and downstream signaling pathways driving immune responses to Doxo are largely
109 unknown. Doxo is a potent inducer of mtDNA stress and IFN-I in vitro (Sistigu et al., 2014; Wu
110 et al., 2019), yet whether mtDNA stress engages cGAS and/or other cytosolic DNA sensors in the
111 heart during DIC, and the effects of prolonged Doxo-dependent IFN-I signaling in cardiac cells,
112 remain unclear.

113 Here, we report that a novel cytoplasmic complex of ZBP1 and cGAS forms in response
114 to mtDNA stress to sustain IFN-I responses in vitro and in vivo. Via biochemical and cell-based

115 analyses, we identify the domains of ZBP1 required for robust binding to cGAS, finding that this
116 interaction is mediated largely via the ZBP1 RHIM domains and the DNA binding domains of
117 both proteins. Finally, we show that ZBP1 is highly expressed in cardiac cells and tissues, and we
118 reveal that the ZBP1-cGAS-STING axis governs Doxo-induced IFN-I responses in vivo. Ablation
119 of this innate immune pathway limits cardiotoxicity and improves heart function during and after
120 Doxo-chemotherapy, providing new insight into the molecular mechanisms of DIC.
121

122 **RESULTS**

123 **ZBP1 is required for robust IFN-I activation downstream of mtDNA stress**

124 Multiple cytosolic DNA sensors have been associated with IFN-I signaling (Keating et al.,
125 2011), and several of them have been shown to bind mtDNA (Matsui et al., 2021; Oka et al., 2012;
126 Rodríguez-Nuevo et al., 2018; Szczesny et al., 2018). Many of these DNA sensors are IFN-I-
127 regulated, suggesting a feed forward loop (Schneider et al., 2014). To explore the role of induced
128 DNA sensors in the detection of mtDNA, we performed RNA sequencing (RNA-seq) analysis in
129 the TFAM heterozygous knockout model (*Tfam*$^{+/-}$), which exhibits persistent mtDNA nucleoid
130 instability, cytosolic mtDNA release, and sustained IFN-I signaling (West et al., 2015). Analysis
131 of mouse embryonic fibroblasts (MEFs) revealed elevated expression of additional nucleic acid
132 sensors, including DNA sensors interferon-inducible IFI200 family members, ZBP1, and several
133 RNA sensors in *Tfam*$^{+/-}$ compared to wild-type (WT) controls (Figure S1A). MEFs lacking STING
134 were significantly impaired in ISG responses after *Tfam* silencing, while Mitochondrial Antiviral
135 Aignaling (MAVS) knockout MEFs were still able to mount high levels of IFN-I responses,
136 suggesting that RNA sensing pathways are not engaged in our system (Figure S1B). Although the
137 human IFI200 homolog IFI16 can potentiate cGAS signaling in response to exogenous and viral

138 DNA (Almine et al., 2017; Jønsson et al., 2017), siRNA knockdown of IFI200 members *Ifi203*
139 and *Ifi204* did not reduce elevated ISG expression in *Tfam*$^{+/-}$ cells (Figures S1C and S1D). qRT-
140 PCR and western blotting of *Tfam*$^{+/-}$ cells revealed that ZBP1 was increased at the RNA and
141 protein levels (Figures S1E and S1F). Strikingly, knockdown of *Zbp1* markedly attenuated ISG
142 expression in *Tfam*$^{+/-}$ cells (Figure S1G). Silencing of *Zbp1* had no effect on *Ifnb1* or ISG
143 expression in WT cells transfected with interferon stimulatory DNA (ISD) (Figure S1H, gray bars),
144 consistent with prior reports indicating that ZBP1 is not required for immediate sensing of short
145 B-form DNA (Ishii et al., 2008; Maelfait et al., 2017; Wang et al., 2008). In contrast, silencing of
146 *Zbp1* reduced the potentiated expression of ISGs in *Tfam*$^{+/-}$ cells after ISD transfection (Figure
147 S1H, blue bars). Taken together, these data suggest that ZBP1 is necessary to sustain IFN-I
148 'priming' in response to mtDNA stress, a phenotype required for potentiated ISG expression in
149 *Tfam*$^{+/-}$ cells after secondary ISD challenge.

150 To expand our analysis of ZBP1 in mtDNA stress responses, we obtained ZBP1-null mice
151 (Ishii et al., 2008) and crossed them onto the *Tfam*$^{+/-}$ background. RNA-seq analysis indicated that
152 in contrast to MEFs from *Tfam*$^{+/-}$ mice, *Tfam*$^{+/-}$*Zbp1*$^{-/-}$ cells did not sustain the elevated ISG
153 expression profile triggered by mtDNA instability (Figure 1A). Additional qRT-PCR and western
154 blotting experiments confirmed that loss of ZBP1 was sufficient to largely abrogate the IFN-I
155 priming of *Tfam*$^{+/-}$ cells (Figures 1B and 1C). In line with our siRNA knockdown data, ZBP1
156 ablation did not affect ISD-induced IFN-I responses in WT MEFs, but significantly reduced the
157 potentiated ISG expression of *Tfam*$^{+/-}$ cells after secondary ISD challenge (Figure 1D).
158 Immunofluorescence microscopy revealed no changes in mtDNA abundance or mitochondrial
159 morphology in *Zbp1*$^{-/-}$ knockout MEFs (Figure 1E). Moreover, we observed that mtDNA nucleoid
160 aggregation and mitochondrial hyperfusion in *Tfam*$^{+/-}$ MEFs, which we previously showed are

161 linked to mtDNA release (West et al., 2015), were not altered by ZBP1 depletion (Figure 1E). This
162 indicates that reduced IFN-I priming in *Tfam*$^{+/-}$*Zbp1*$^{-/-}$ cells is not due to the alleviation of mtDNA
163 stress, but instead results from impaired sensing and/or signaling downstream of mtDNA release.

164 Consistent with our prior work (Wu et al., 2019), we observed that a non-lethal dose of
165 Doxo, a widely used anthracycline chemotherapeutic that induces mtDNA damage and
166 mitochondrial dysfunction (Berthiaume and Wallace, 2007; Wallace et al., 2020), also promoted
167 nucleoid aggregation, cytosolic mtDNA release, and IFN-I signaling (Figures 1F-1H and S1I).
168 Similar to *Tfam*$^{+/-}$ cells, low dose Doxo treatment markedly enhanced ZBP1 protein levels (Figure
169 1H), and robust Doxo-induced ISG expression required ZBP1 (Figures 1I and 1J). Notably, the
170 Doxo-induced expression of ISG was heavily reliant on signaling via the type I interferon receptor
171 (IFNAR), but entirely independent of MAVS and RNA sensing (Figures 1K). Collectively, these
172 results indicate that ZBP1 is an essential sensor mediating the IFN-I program triggered by acute
173 (Doxo-induced) and persistent (*Tfam*$^{+/-}$) mtDNA stress.

174 ZBP1 is a well-appreciated driver of receptor-interacting protein kinase 3 (RIPK3)-mixed
175 lineage kinase domain-like pseudokinase (MLKL)-dependent necroptosis, an inflammatory form
176 of cell death that can be induced by interferon that can feed forward to potentiate IFN-I and pro-
177 inflammatory responses (Baik et al., 2021; Devos et al., 2020; Ingram et al., 2019; Jiao et al., 2020;
178 Sridharan et al., 2017; Yang et al., 2021). Although MLKL was slightly increased, other
179 necroptosis factors were not elevated in *Tfam*$^{+/-}$ MEFs (Figure S1J). To exclude the possibility that
180 MLKL promotes mtDNA instability and release or IFN-I priming in *Tfam*$^{+/-}$ cells, we silenced
181 MLKL by siRNA (Figure S1K). Notably, *Tfam*$^{+/-}$ MEFs depleted of MLKL continued to show
182 mtDNA nucleoid aggregation, and also maintained elevated ISG expression (Figures 1L, S1L and
183 S1M). Moreover, WT and *Tfam*$^{+/-}$ MEFs exhibited similar cell death kinetics in response to

184 necroptosis induced by TNFα+zVAD+CHX treatment (Figure 1M). Cell death triggered by high
185 dose Doxo treatment was also equivalent between WT and *Zbp1*$^{-/-}$ MEFs (Figure 1N). In sum,
186 these results suggest that ZBP1 regulates the mtDNA stress-mediated IFN-I program in *Tfam*$^{+/-}$
187 and Doxo-treated cells independently of MLKL and a feed forward loop of cell death.
188
189 **ZBP1 regulates cGAS localization via direct interactions in the cytosol during mtDNA stress**
190 Unlike cGAS, ZBP1 is predominantly expressed in the cytosol (Figure S2A), although it
191 has been shown to sense viral RNA in the nucleus (Zhang et al., 2020). Interestingly, we observed
192 a significant increase in the proportion of cytosolic cGAS in *Tfam*$^{+/-}$ MEFs (Figures S2A and S2B),
193 where ZBP1 is highly induced, relative to WT. IFNβ treatment increased the overall expression as
194 well as the cytosolic proportion of cGAS in both WT and *Tfam*$^{+/-}$ cells, suggesting that the presence
195 of cytosolic mtDNA and IFN-I signaling promote cGAS redistribution during mtDNA stress
196 (Figures S2A and S2B). TFAM depletion in human skin fibroblasts (HFFs) also induced interferon
197 stimulated gene (ISG) expression and drove cGAS into the cytosol (Figures S2C, 2A and 2B).
198 Similar to TFAM-depletion, low dose Doxo triggered robust cGAS re-localization, with roughly
199 half of the cellular cGAS protein accumulating in the cytosol after exposure (Figures S2D and
200 S2E). Therefore, cGAS undergoes a dynamic redistribution to the cytoplasm during both genetic
201 and pharmacologic induction of mtDNA stress, which is likely necessary to sustain IFN-I signaling
202 in response to cytosolic mtDNA.
203 Our prior data indicated that the mtDNA stress-triggered IFN-I program involves the
204 nucleic acid sensor ZBP1 induction and cGAS redistribution. We further observed significantly
205 less cytoplasmic cGAS in *Tfam*$^{+/-}$*Zbp1*$^{-/-}$ cells compared to *Tfam*$^{+/-}$ cells (Figures 2C and 2D),
206 suggesting that high ZBP1 levels influence cGAS localization. Loss of ZBP1 and cytoplasmic

207 cGAS in *Tfam*$^{+/-}$*Zbp1*$^{-/-}$ cells also led to markedly lower ISG expression (Figures 1C and 2C),
208 which led us to hypothesize that ZBP1 and cGAS might work cooperatively to sustain the IFN-I
209 program triggered by mtDNA stress. To explore this possibility, we first investigated whether these
210 two mtDNA sensors interact in cells. Endogenous co-immunoprecipitation (co-IP) experiments in
211 *Tfam*$^{+/-}$ cells using anti-cGAS antibody revealed strong interactions between cGAS and ZBP1 in
212 cytosolic, but not nuclear, extracts (Figure 2E). Recombinant mouse IFNβ treatment, which
213 substantially enhanced the expression of ZBP1, triggered strong interactions of cGAS and ZBP1
214 in both WT and *Tfam*$^{+/-}$ cells (Figure 2E). Similarly, Doxo induced the upregulation of ZBP1, re-
215 localization of cGAS to the cytosolic fraction, and increased the co-immunoprecipitation of
216 cytosolic cGAS-ZBP1 complexes (Figure 2F). Next, to define the domains of ZBP1 necessary for
217 interaction with cGAS, we generated ZBP1 constructs lacking the first or both Z-form nucleic acid
218 (Z-NA) binding domains at the N-terminus (ΔZα1, ΔZα1ΔZα2), RHIM domain mutants (mRA,
219 mRB) or deletions (ΔRA, ΔRB), and a C-terminal signaling domain deletion that also lacks a third
220 putative RHIM sequence (Kaiser et al., 2008; Kuriakose and Kanneganti, 2018; Takaoka et al.,
221 2007) (Figure 2G). Upon transient expression of ZBP1-FLAG and cGAS-HA constructs, we noted
222 that ZBP1-FLAG lacking both Z-NA binding domains was attenuated in pulling down cytosolic
223 cGAS compared to full length ZBP1 (Figure 2H, compare lane 3 to 1). ZBP1-FLAG lacking the
224 C-terminus was more attenuated in pulling down cGAS (Figure 2H, compare lane 6 to 1). However,
225 ZBP1-FLAG constructs possessing mutated (mRA, mRB; Figure 2H) or wholly deleted (ΔRA,
226 ΔRB; Figure 2I) RHIM motifs were unable to pulldown cytosolic cGAS. Finally, we generated a
227 ZBP1 construct of roughly 100 amino acids containing the RHIM A and B domains (RA+RB;
228 Figure 2G) and found that this small construct was sufficient to immunoprecipitate cGAS in
229 cytosolic co-IP experiments (Figure 2J).

230 Additional co-IP experiments to identify the domains of cGAS mediating binding to ZBP1
231 revealed that full-length ZBP1 was able to interact with both the N-terminal 148 aa of cGAS
232 (cGAS N-term), as well as a construct lacking the first 147 amino acids (ΔN-term) (Figures S2F
233 and S2G), suggesting that at least two interaction sites bridge cGAS and ZBP1. However, the small
234 ZBP1 RA+RB fragment more strongly co-immunoprecipitated with the cGAS N-term construct
235 (Figures S2H). Taken together, our data suggest that ZBP1 and cGAS interact in the cytosol during
236 mtDNA stress to sustain IFN-I responses. Furthermore, multiple interacting mechanisms are
237 required for full ZBP1-cGAS binding, but the strongest interactions between the two cytosolic
238 sensors are bridged by the ZBP1 RHIM domains and cGAS N-terminus (Figure 2K).
239
240 **ZBP1 restrains cGAS in the cytosol and potentiates its activity during mtDNA stress**
241 Recent work has revealed that cGAS re-localizes to the cytosol in response to DNA
242 transfection (Michalski et al., 2020; Sun et al., 2021), and our data has revealed this also occurs
243 after IFNβ treatment or induction of mtDNA stress. Because ZBP1 is strongly induced by mtDNA
244 stress and interacts with cGAS, we reasoned that ZBP1 might enhance cytosolic retention of cGAS.
245 Consistent with the endogenous expression pattern in most cells (Volkman et al., 2019), cGAS
246 primarily localized to the nucleus after transient transfection (Figures 3A and 3B). In contrast, cells
247 co-expressing cGAS and full length ZBP1 (ZBP1 FL) or the small ZBP1 RA+RB fragment
248 exhibited an increased abundance of cGAS in the cytoplasm (Figures 3A and 3B), suggesting that
249 interactions through the ZBP1 RHIM domains are critical for cytosolic cGAS accumulation. Co-
250 expression of ZBP1 mutants lacking the Z-NA binding domains or the C-terminus were also able
251 to increase the cytosolic abundance of cGAS (Figures S3A). However, co-expression of the ZBP1

252 ΔRA construct, which cannot bind cGAS, failed to drive cGAS into the cytosol of COS-7 cells
253 (Figures 3A and 3B).

254 We next examined whether binding of ZBP1 affects the enzymatic activity of cGAS during
255 mtDNA stress. We first confirmed that *Tfam*$^{+/-}$ MEFs produced more cGAMP compared to WT
256 cells, indicative of enhanced cGAS activity (Figure S3B). Then, we expressed cGAS alone or
257 cGAS and ZBP1 together in 293FT cells reconstituted with STING (293FT-STING) and examined
258 ISG expression. ZBP1 alone or cGAS and ZBP1 co-expression did not potentiate ISG expression
259 in cells without mtDNA instability (siCtrl). However, silencing of TFAM in cells expressing cGAS
260 elevated ISG expression, with the highest ISG expression being observed in TFAM-depleted cells
261 co-expressing cGAS and ZBP1 (Figures S3C and S3D). Similar trends were observed in Doxo-
262 treated cells expressing cGAS and ZBP1 (Figures 3C and 3D). The findings suggest that: 1) ZBP1
263 alone is not sufficient to trigger IFN-I signaling in response to transfected plasmid DNA, TFAM-
264 depletion, or Doxo-induced mtDNA stress; and 2) cGAS and ZBP1 work cooperatively to sense
265 mtDNA stress and fully activate and sustain IFN-I responses. In agreement, *Zbp1*$^{-/-}$ MEFs
266 produced less cGAMP after Doxo exposure compared to WT (Figure S3E). Finally, we explored
267 which domains of ZBP1 were essential for maximizing cGAS activity by transfecting 293FT with
268 cGAS and various ZBP1 constructs (Figure 3E). Interestingly, the Z-NA domains (Zα1Zα2),
269 RHIM motifs (RA and RB), and the C-terminus of ZBP1 were all required to potentiate cGAS
270 production of cGAMP upon Doxo-mediated mtDNA stress (Figure 3F).

271 Since the loss of both Z-NA binding domains (ΔZα1Zα2) of ZBP1 weakens its ability to
272 bind cGAS (Figure 2H) and limits cGAS activation (Figure 3F), we then explored whether nucleic
273 acids facilitate cGAS-ZBP1 interactions, and therefore potentiate cGAS activity. We developed a
274 nuclease assay where benzonase was utilized to significantly degrade cytosolic nucleic acids

275 before co-IP (Figure 3G). Real time qPCR analysis of mtDNA abundance in 1% NP-40 cellular
276 extracts revealed that benzonase treatment was effective at degrading over 99% of mtDNA (Figure
277 3H). After benzonase treatment, ZBP1 was less efficient at pulling down cGAS (Figure 3I),
278 mirroring weaker interactions between cGAS and ZBP1 ΔZα1Zα2 constructs (Figure 2H). Taken
279 together, our data suggest two distinct interactions bridge cGAS-ZBP1 complexes in cells, which
280 together retain cGAS in the cytosol and potentiate and/or sustain cGAMP production and IFN-I
281 responses to cytosolic mtDNA. We propose that the RHIM domains of ZBP1 bind strongly with
282 the N-terminus of cGAS, whereas the DNA binding domains of both proteins also interact and are
283 likely bridged by DNA (Figure 3J).
284
285 **mtDNA stress promotes the accumulation of Z-form DNA that potentiates IFN-I responses**
286 Viral and endogenous Z-form RNA are key ligands nucleating ZBP1-mediated necroptosis
287 and inflammation (Devos et al., 2020; Jiao et al., 2020; Kesavardhana and Kanneganti, 2020;
288 Kesavardhana et al., 2020; Koehler et al., 2021; Maelfait et al., 2017; Zhang et al., 2020); however,
289 ZBP1 can also bind oxidized mtDNA (Saada et al., 2022) and stabilize Z-form DNA (Deigendesch
290 et al., 2006; Ha et al., 2006, 2008; Schwartz et al., 2001). We have previously shown that cGAS
291 activation in *Tfam*$^{+/-}$ cells requires mtDNA release (West et al., 2015; Wu et al., 2019), although
292 *Tfam*$^{+/-}$ cells do not display enhanced steady-state reactive oxygen species production (Woo et al.,
293 2012). This argues against a role for oxidized mtDNA, so we next explored whether Z-form DNA
294 accumulated during mtDNA stress using an antibody specific for left-handed Z-DNA (Buzzo et
295 al., 2021; Möller et al., 1982). We first validated the specificity of anti-Z-DNA antibody for
296 immunofluorescence assay by transfecting poly(dA:dT) (high propensity to form B-DNA) and
297 poly(dG:dC) (high propensity to form Z-DNA) with polyethylenimine (PEI), a polyamine polymer

298 that has been shown to induce/stabilize Z-DNA formation with poly(dG:dC) sequences (Thomas
299 et al., 1991). We confirmed that this antibody specifically stained PEI complexed poly(dG:dC),
300 while SYTOX DNA stain labeled both forms of DNA uniformly (Figure 4A). Utilizing the same
301 antibody and quantitative immunofluorescence microscopy, we next screened for the presence of
302 Z-DNA in situ. Notably, we observed increased cytosolic and mitochondrial Z-DNA accumulation
303 in TFAM-deficient cells (Figures 4B and 4C). Additional Z-DNA accumulation in both
304 compartments was detected in *Tfam*$^{+/-}$ MEFs exposed to Hydralazine, a vasodilator that can
305 stabilize Z-form DNA and is linked to drug-induced lupus (Thomas et al., 1993; Timlin et al., 2019)
306 (Figures 4B and 4C). qRT-PCR analysis revealed potentiated ISG expression in Hydralazine-
307 treated *Tfam*$^{+/-}$ MEFs, indicating that Z-form DNA species generated during mtDNA stress
308 contribute to the IFN-I program (Figure 4D). Remarkably, ZBP1 was necessary for the
309 Hydralazine-mediated potentiation of ISGs in TFAM-depleted cells, as IFN-I responses were
310 drastically reduced in *Zbp1*$^{-/-}$ MEFs (Figure 4D). Doxo also enriched Z-DNA abundance
311 colocalizing with the mitochondrial marker TOMM20, as well as in the cytosol (Figures 4E and
312 4F), further supporting the notion that generalized mtDNA instability promotes the accumulation
313 of Z-DNA.

314 To further investigate the immunostimulatory properties of DNA from different subcellular
315 pools, we isolated cytosolic (Cyto.), mitochondrial (Mito.) and nuclear (Nuc.) fractions from
316 vehicle- or Doxo-treated MEFs and transfected the purified DNA from each into primary mouse
317 fibroblasts (Figure 4G). After confirming that the anti-Z-DNA antibody is suitable for detecting
318 Z-DNA by immunoblotting (Figure 4H), we next investigated the presence of Z-DNA from each
319 cellular fraction. In agreement with immunofluorescence analyses, slot blotting of pure DNA from
320 all fractions revealed elevated Z-DNA accumulation in the mitochondrial and cytosolic

321 compartments after Doxo (Figure 4I). Notably, mtDNA, followed by cytosolic DNA, isolated from
322 Doxo-exposed cells was significantly more stimulatory than comparable fractions from vehicle-
323 treated cells. However, nuclear DNA from both groups activated IFN-I responses to the same level
324 (Figure 4J). Collectively, these results indicate that mtDNA stress induces mitochondrial and
325 cytosolic Z-DNA accumulation, which is then stabilized by elevated ZBP1 to potentiate IFN-I
326 signaling.
327
328 **Doxorubicin induces a robust cardiac IFN-I response that induces mitochondrial and**
329 **cardiomyocyte dysfunction**
330 Earlier work and our own data revealed that Doxo drives mtDNA nucleoid aggregation and
331 cytosolic mtDNA release in cancer cells and fibroblasts (Ashley and Poulton, 2009; Wu et al.,
332 2019) (Figures 1F and 1G). We therefore hypothesized that Doxo might trigger mtDNA stress and
333 cytosolic release in cardiomyocytes (CMs), leading to elevated innate immune signaling and CM
334 dysfunction. In agreement, low dose Doxo exposure to human induced pluripotent stem cell-
335 derived CMs (hiPSC-CMs) caused pronounced mtDNA nucleoid aggregation, mitochondrial
336 network hyperfusion, and the accumulation of cytosolic DNA, indicative of mtDNA stress and
337 mitochondrial dysfunction (Figure 5A). Unbiased transcriptomic and bioinformatic approaches
338 also revealed innate immune signatures in adult murine hearts and hiPSC-CMs challenged with
339 Doxo. Gene set enrichment analysis showed that Doxo repressed OXPHOS transcripts, but
340 increased multiple innate immune and inflammatory genes, including those associated with
341 interferons, TNFα, and DNA damage (Figure 5B). Furthermore, analysis of 261 differentially
342 expressed genes across all three datasets (Burridge et al., 2016; Zhang et al., 2012) indicated that
343 type I interferon signaling (Interferon Alpha Response) was the most heavily represented network

344 (Figure 5C). Additional pathway analysis predicted robust activation of upstream regulators
345 governing IFN-I responses, including interferon regulatory transcription factors (IRF1/3/7 and
346 STAT1) and type I interferon cytokines (IFNα and β) (Figure S4A). Moreover, robust enrichment
347 of STING-dependent *Zbp1* and other ISGs (*Ifit3*, *Cmpk2*, *Cxcl10*) was observed in both Doxo-
348 exposed murine hearts and hiPSC-CMs (Figure S4A). In line with bioinformatic analyses, Doxo
349 strongly upregulated type I interferons, ZBP1, and other ISGs in hiPSC-CMs and murine neonatal
350 CMs (Figures 5D-5F). Blocking the IFN-I receptor with anti-IFNAR antibody significantly
351 suppressed Doxo-induced ISGs (Figure 5G). Moreover, Doxo failed to induce robust ISG
352 responses in *Ifnar*$^{-/-}$, *Sting*$^{-/-}$, and *Zbp1*$^{-/-}$ CMs, indicating that their expression is mediated by the
353 ZBP1-cGAS axis and autocrine/paracrine IFNAR signaling (Figure 5H).

354 Clinical case reports have linked IFNα immunotherapy to cardiomyopathy and other
355 serious cardiac complications (Angulo et al., 1999; Benjamini et al., 2007; Khakoo et al., 2005;
356 Kuwata et al., 2002; Zhao et al., 2014; Zimmerman et al., 1994), yet the direct effects of prolonged
357 IFN-I on CM function have not been characterized. Interestingly, we observed that hiPSC-CMs
358 are highly responsive to IFN-I (Figure S4B) and that prolonged exposure increased expression of
359 genes correlating with CM dysfunction (natriuretic peptides (*Nppa/Nppb*) and β myosin heavy
360 chain (*Myh7*)) (Figure S4C). Consistent with bioinformatic analyses, prolonged IFN-I also
361 decreased expression of mtDNA-encoded OXPHOS genes, while elevating some nuclear DNA-
362 encoded transcripts, suggestive of respiratory chain dysfunction (Figure S4D). Reduced mtDNA-
363 encoded OXPHOS gene expression was also observed in murine neonatal CMs exposed to acute
364 IFNβ or Doxo (Figure S4E). In addition, Doxo or IFN-I exposure shortened the beat periodicity
365 of iPSC-CMs and caused significant CM vacuolization and arrhythmic contractions when
366 combined (Figure S4F). Together, these results indicate that Doxo-induced mtDNA stress triggers

367 CM IFN-I responses in vitro and in vivo, and also suggest that prolonged IFN-I signaling has
368 cardiotoxic effects by enhancing CM mitochondrial dysfunction and contractility defects.
369

370 **Adjuvant IFNα synergizes with Doxorubicin to enhance cardiac and mitochondrial**
371 **dysfunction in tumor-bearing mice**

372 In order to expand our in vitro findings and advance mechanistic understanding of
373 cardiotoxic synergy between Doxo and IFN-I, we merged an autochthonous melanoma model
374 (Damsky et al., 2011; Dankort et al., 2009) with an extended Doxo protocol that more closely
375 resembles clinical timelines in late DIC (Figures 6A and 6B). Doxo chemotherapy significantly
376 restricted melanoma growth, with adjuvant IFNα providing a modest synergistic effect (Figure
377 6B). Consistent with the clinical studies, Doxo treatment reduced left ventricular ejection fraction
378 (EF), fractional shortening (FS) and left ventricle (LV) mass (Figure 6C), while inducing left
379 ventricle dilation, wall thinning and cardiac fibrosis (Figure 6D-6F). Interestingly, ZBP1 and other
380 ISGs were elevated in Doxo-exposed hearts relative to mice receiving vehicle only (Figure 6G).
381 Mice receiving Doxo plus adjuvant IFNα exhibited more pronounced left ventricular dysfunction,
382 elevated cardiac fibrosis, and higher cardiac ISG expression compared to the Doxo only group
383 (Figures 6C-6G). Finally, melanoma bearing mice receiving Doxo and IFNα showed reduced
384 cardiac mtDNA abundance and OXPHOS protein expression (Figures 6H and 6I). These results
385 suggest that IFN-I signaling synergizes with Doxo to enhance mitochondrial dysfunction, cardiac
386 fibrosis, and heart failure in vivo.
387

388 **mtDNA stress triggers a ZBP1-STING-IFNAR-dependent IFN-I program that contributes**
389 **to Doxorubicin-induced cardiotoxicity**

390 To dissect the cardiac IFN-I signaling pathway downstream of Doxo-induced mtDNA
391 stress in vivo, we applied our Doxo dosing regimen (Figure 7A) to multiple genetically modified
392 mouse stains that are deficient in cytosolic mtDNA sensing and IFN-I signaling. Doxo was
393 administered for four weeks to adult mice, and cardiac function was assessed by serial
394 transthoracic echocardiography pre-Doxo exposure (week -1) and every two weeks thereafter until
395 week ten when animals were sacrificed. Transthoracic echocardiography of WT mice revealed
396 marked impairments in cardiac functional measures of left ventricular EF (parasternal long axis
397 B-mode) and FS (short axis M-mode) after Doxo (Figure 7B, black lines). In contrast, mice lacking
398 ZBP1, STING or IFNAR exhibited higher EF and FS compared to WT throughout the longitudinal
399 study (Figure 7B, maroon, green and blue lines). In depth analysis of longitudinal
400 echocardiographic measurements showed that *Zbp1*$^{-/-}$, *Sting*$^{-/-}$ and *Ifnar*$^{-/-}$ mice exhibited lower
401 Doxo-induced wall thinning, left ventricle dilation, and weight loss compared to WT controls
402 (Figures 7C and S5A-S5C). To link cardiac dysfunction with sustained IFN-I signaling, we
403 examined transcript and protein abundance of ISGs seven weeks after the cessation of Doxo
404 injection. WT mice exhibited sustained expression of ISGs assayed at the week 10 timepoint post-
405 Doxo. In contrast, ZBP1 and other ISGs were not significantly upregulated in Doxo-exposed *Zbp1*$^{-}$
406 $^{/-}$, *Sting*$^{-/-}$ and *Ifnar*$^{-/-}$ mice compared to vehicle controls (Figures 7E, S6A and S6B). Moreover, all
407 knockout strains exhibited reduced cardiac expression of genes expressed in the failing heart
408 (Figures 7F and S6C). In agreement with cardiac transcript expression, histologic analyses of
409 Doxo-challenged *Zbp1*$^{-/-}$, *Sting*$^{-/-}$ and *Ifnar*$^{-/-}$ mice revealed significantly less CM dropout and
410 cytoplasmic vacuolization at week 10 compared to WT controls (Figures 7G, S6D and S6E), and
411 all knockout strains had markedly lower cardiac fibrosis as revealed by Sirius Red staining
412 (Figures 7H and S6F). Finally, Doxo-induced mtDNA instability and OXPHOS subunit loss was

413 also significantly lessened in cardiac extracts from *Sting*$^{-/-}$ and *Ifnar*$^{-/-}$ mice (Figure S6G-S6I). In
414 summary, our data reveal a that the ZBP1-STING signaling axis contributes to cardiotoxic IFN-I
415 signaling that contributes significantly to the pathobiology of chemotherapy-related heart failure.
416

417 **DISCUSSION**

418 ZBP1/DLM-1/DAI was initially identified as an ISG in activated macrophages, and later a
419 cytosolic DNA sensor that binds TBK1 and IRF3 to induce IFN-I responses (Fu et al., 1999;
420 Takaoka et al., 2007). Subsequent knockdown studies confirmed a role for ZBP1 in the induction
421 of IFN-I responses in L929 fibroblasts transfected with long B-form DNA, skin fibroblasts infected
422 with human cytomegalovirus (HCMV), and vaginal epithelial cells infected with herpes simplex
423 virus 2 (HSV-2) or transfected with HSV-2 DNA (DeFilippis et al., 2010; Triantafilou et al., 2014;
424 Wang et al., 2008). In contrast, experiments in knockout MEFs, macrophages, and dendritic cells
425 revealed that ZBP1 is dispensable for IFN-I and pro-inflammatory cytokine induction after
426 poly(dA:dT) B-form DNA transfection (Ishii et al., 2008) or mouse cytomegalovirus infection
427 (Maelfait et al., 2017). Thus, the roles of ZBP1 in cytosolic DNA sensing and IFN-I induction
428 have remained controversial. Our prior work revealed that mtDNA stress and release in *Tfam*$^{+/-}$
429 and Doxo-treated cells engages the cGAS-STING pathway, leading to an IFN-I signature
430 characterized by the high level expression of many ISGs, including ZBP1 (West et al., 2015; Wu
431 et al., 2019). In this study, we have uncovered that loss of ZBP1 ablates the steady state elevation
432 of ISGs in *Tfam*$^{+/-}$ cells and severely attenuates IFN-I responses after Doxo treatment. However,
433 in line with studies from Ishii et al. 2008 and Maelfait et al. 2017, we find that *Zbp1*$^{-/-}$ cells are
434 fully responsive to B-DNA transfection and exhibit no impairment in ISG expression compared to
435 controls. More recent work has shown that ZBP1 is a sentinel of endogenous and microbial RNA

436 during infection, leading to inflammatory responses and necroptotic cell death (Guo et al., 2018;
437 Jiao et al., 2020; Kuriakose et al., 2018; Maelfait et al., 2017; Upton et al., 2012; Zhang et al.,
438 2020). Although mitochondrial dsRNA release can trigger IFN-I responses (Dhir et al., 2018;
439 Tigano et al., 2021), we find that cytosolic RNA sensing via the RIG-I-like receptor (RLR)-
440 Mitochondrial antiviral signaling (MAVS) pathway is not required for IFN-I signaling in *Tfam*$^{+/-}$
441 or Doxo treated cells. Therefore, our data highlight ZBP1 an innate immune sentinel for mtDNA
442 that is uniquely required for the maintenance of steady state ISG expression and IFN-I priming
443 phenotypes triggered by mtDNA stress and release.

444 Recent work has shown that cGAS predominately resides in the nucleus tightly bound to
445 histones 2A and 2B, which is critical to restrain cGAS and limit autoreactivity against endogenous
446 DNA (Volkman et al., 2019; Zhao et al., 2020). However, the mechanisms governing cGAS
447 distribution and the interacting partners that influence cGAS compartmentalization remain largely
448 unclear. We have found that mtDNA stress and release increases the cytosolic pool of cGAS in a
449 ZBP1-dependent manner. Our data indicate that ZBP1 complexes with and retains cGAS in the
450 cytoplasm to sustain IFN-I responses to mtDNA. Furthermore, we show that binding of the two
451 proteins is mediated predominately via the RHIM A (RA) of ZBP1 and the N-terminus of cGAS,
452 as RHIM mutants fail to immunoprecipitate cGAS or re-localize it to the cytoplasm. The N-
453 terminus of cGAS contains a nuclear localization sequence (NLS) (Liu et al., 2018), and our data
454 indicate that the RHIM domains of ZBP1 preferentially interact with this region of cGAS.
455 Therefore, we posit that during persistent mtDNA stress and elevated ZBP1 expression, ZBP1
456 RHIM domains obscure the N-terminal NLS of cGAS, leading to cGAS entrapment in the cytosol
457 for sustained sensing of mtDNA. Our data revealing that a minimal RA+RB construct interacts
458 most strongly with the cGAS N-terminus and is sufficient to increase cytosolic cGAS intensity is

459 consistent with this hypothesis. However, our experiments cannot exclude that another protein or
460 a protein complex links ZBP1 to cGAS, and future experiments are required to define the ZBP1-
461 cGAS complexosome.

462 ZBP1 forms homotypic interactions with the RHIM domain-containing proteins RIPK1
463 and RIPK3 to mediate NF-κB activation and innate immune signaling, as well as promote RIPK3-
464 MLKL-dependent necroptosis (Kaiser et al., 2008; Kuriakose and Kanneganti, 2018). We
465 observed that ZBP1 and cGAS interact both endogenously and upon overexpression, although we
466 did not identify an obvious canonical or degenerate RHIM motif in cGAS. It is possible that the
467 ZBP1 RHIM domains interact with cGAS in a non-homotypic manner; however, our data cannot
468 exclude that a second RHIM containing protein bridges the ZBP1-cGAS complex. RIPK3 is a
469 likely candidate, as DNA sensing by cGAS can activate RIPK3 to trigger necroptosis (Brault et
470 al., 2018; Sarhan et al., 2019). Recently, ZBP1/RIPK1/RIPK3 was shown to induce a subset of
471 ISGs in cortical neurons during ZIKA virus infection (Daniels et al., 2019). ZIKA virus induces
472 mitochondrial damage (Ledur et al., 2020; Yau et al., 2021), and the closely related Dengue
473 flavivirus can trigger mtDNA release and promote cGAS-STING signaling (Aguirre et al., 2017;
474 Sun et al., 2017). Therefore, it is possible that RIPK1 and/or RIPK3 participate in the ZBP1-cGAS
475 complex and help sustain IFN-I signaling and ISG expression downstream of mitochondrial stress.
476 Although deletion of ZBP1 is sufficient to abrogate IFN-I responses in cells exhibiting mtDNA
477 instability, we found that ablation of MLKL does not blunt IFN-I responses in TFAM-deficient
478 cells. In contrast, loss of ZBP1 was sufficient to nearly abolish IFN-I responses in cells exhibiting
479 mtDNA instability. Thus, cGAS and ZBP1 form a novel complex and function cooperatively to
480 maintain the IFN-I program downstream of mtDNA release, independently of necroptotic cell
481 death and a feedforward release of cell-free mtDNA.

482 Our results also suggest that ZBP1 augments the enzymatic activity of cGAS in response
483 to mtDNA release, leading to elevated ISG expression. This is not altogether surprising, given that
484 ZBP1 RHIM-cGAS binding enhances the cytosolic localization of cGAS where it can more readily
485 sense liberated mtDNA. However, we observed that the ZBP1 DNA binding domains and cytosolic
486 DNA are also needed for the full binding of both proteins. Moreover, ΔZα1Zα2 mutants are unable
487 to potentiate cGAMP production after Doxo-induced mtDNA stress. This suggests that ZBP1 may
488 stabilize short fragments of cytosolic mtDNA and enhance or prolong detection by cGAS.
489 Alternatively, ZBP1 may promote cGAS dimerization by interacting with its N-terminus (Hooy
490 and Sohn, 2018) or alter the conformation of mtDNA fragments to promote cGAS laddering
491 (Andreeva et al., 2017). ZBP1 can also localize to GTPase-activating protein-(SH3 domain)–
492 binding protein 1 (G3BP1) positive stress granules, and G3BP1 primes cGAS for activation
493 (Deigendesch et al., 2006; Zhao et al., 2022). Follow-up biochemical studies are required to clarify
494 these possibilities and define the molecular basis of the ZBP1-cGAS-mtDNA complex, which may
495 lead to the development of novel compounds to inhibit IFN-I activation by mtDNA in human
496 disease.

497 Prior work has shown that the Zα domains of ZBP1 can bind and stabilize Z-form DNA
498 (Brown et al., 2000; Ha et al., 2008). Left-handed Z-DNA was identified in 1979 and is a higher
499 energy, and therefore less common, conformation than right-handed B-DNA (Herbert and Rich,
500 1996; Wang et al., 1979). This unique DNA conformation is more resistant to nuclease degradation
501 and is more immunogenic/antigenic than B-DNA (Ravichandran et al., 2019). Recently,
502 extracellular Z-DNA was revealed as a structural component of the bacterial biofilm matrix that
503 functions to stabilize biofilms from nuclease degradation, thus impairing innate immunity and
504 promoting infection (Buzzo et al., 2021). Other studies have linked intracellular Z-DNA to various

505 human diseases including cancer, neurodegeneration, and autoimmunity (Ravichandran et al.,
506 2019; Wang and Vasquez, 2007). Interestingly, G-C rich DNA with the propensity to form Z-DNA
507 is elevated in the serum of patients with systemic lupus erythematosus (SLE) (Helden, 1985).
508 Moreover, anti-Z-DNA antibodies have been observed in patients with SLE and rheumatoid
509 arthritis (RA) (Lafer et al., 1983; Sibley et al., 1984; Suram et al., 2002), as well as in Lupus-prone,
510 MRL/lpr mice (Bergen et al., 1987). These observations strongly link Z-DNA to IFN-I-mediated
511 autoimmune disease; however, the upstream signals that provoke Z-DNA formation and the
512 cellular sources of Z-DNA remain unclear. Computational analysis has revealed that sequences in
513 the noncoding displacement loop (D-loop) region of mtDNA are competent to form Z-DNA
514 (Oliveira et al., 2013). Our prior work revealed that the most abundant cytosolic mtDNA sequences
515 in TFAM-deficient cells are derived from the D-Loop (West et al., 2015). Therefore, we propose
516 that pharmacological or genetic induction of mtDNA stress increases mitochondrial D-loop
517 derived Z-DNA and cytosolic release. Interestingly, we noted that hydralazine, an anti-
518 hypertensive drug that stabilizes Z-DNA and induces Lupus-like disease in 5-10% of patients,
519 robustly stabilized mitochondrial Z-DNA in TFAM-deficient cells. Moreover, hydralazine
520 treatment increased IFN-I responses only in presence of ZBP1. These data provide further
521 evidence that mitochondrial Z-DNA is immunostimulatory, and they suggest that high levels of
522 ZBP1 serve to stabilize mitochondrial Z-DNA and/or bring it into a complex with cGAS to
523 potentiate cGAMP production and sustain IFN-I responses. Future research is warranted to define
524 the precise Z-DNA sequences in the mitochondrial genome and to clarify how the ZBP1-cGAS
525 complex is uniquely tuned to sense this mitochondrial alarmin.

526 Anthracycline chemotherapeutics, such as Doxo, are among the most effective and widely
527 used antineoplastic drugs, however their clinical application is limited by adverse cardiac side

528 effects that occur in many patients (Henriksen, 2018). The molecular mechanisms responsible for
529 DIC remain elusive, although recent evidence suggests CM-specific Doxo-topoisomerase 2 beta
530 (Top2β) cleavage complexes induce DNA damage leading to mitochondrial dysfunction and
531 reactive oxygen species (ROS) generation (Zhang et al., 2012). This is hypothesized to trigger a
532 self-propagating cycle of ROS and mitochondrial oxidative damage that continues after Doxo
533 therapy ends and ultimately leads to CM cell death, cardiac remodeling, and heart failure (Lebrecht
534 et al., 2003). Persistent mitochondrial dysfunction may also synergize with other maladaptive
535 responses, such as inflammation, to accelerate cardiac damage. We have uncovered that Doxo
536 induces hallmark mtDNA instability iPSC-CMs and triggers a robust IFN-I signature in CMs and
537 murine hearts that is dependent on ZBP1, STING, and IFNAR. Expanding on transcriptional
538 profiling data, we employed a Doxo dosing protocol that more closely resembles clinical timelines
539 in late DIC. Using this protocol, we observe that ZBP1 and other IFN-I-dependent ISGs remain
540 elevated in the heart for seven weeks after the last Doxo dose, suggestive of a self-propagating
541 IFN-I cycle. Moreover, ZBP1, STING, and IFNAR knockout mice are significantly protected from
542 DIC and display marked improvements in multiple longitudinal echocardiographic measures of
543 LV function and cardiac output. Finally, mutant mice exhibit reduced cardiomyocyte damage,
544 cardiac fibrosis, mtDNA damage, and mitochondrial dysfunction. Taken together, we conclude
545 that the ZBP1-cGAS axis is a key sentinel of cardiac mtDNA stress and Z-DNA, which propagates
546 cardiotoxic IFN-I responses and enhances cardiac remodeling and heart failure after Doxo
547 exposure.

548 IFNα is an FDA-approved immunotherapy for malignant melanoma, AIDS-related
549 Kaposi's sarcoma, follicular lymphoma, and hairy cell leukemia. IFNα may also be combined with
550 traditional chemotherapies such as cisplatin, fluorouracil, and Doxo for the treatment of malignant

551 mesothelioma, unresectable hepatocellular carcinoma, and renal cell carcinoma (Kuwata et al.,
552 2002; Parra et al., 2001; Yeo et al., 2005). However, as with other chemo- and immunotherapies,
553 noted cardiac side effects limit the clinical utility of IFNα. In fact, multiple case reports have linked
554 IFNα immunotherapy to cardiomyopathy and other serious cardiac complications (Angulo et al.,
555 1999; Benjamini et al., 2007; Khakoo et al., 2005; Kuwata et al., 2002; Zhao et al., 2014;
556 Zimmerman et al., 1994). Notably, two studies reported significant cardiac dysfunction in patients
557 who received both Doxo chemotherapy and IFNα (Benjamini et al., 2007; Zimmerman et al.,
558 1994). Moreover, a study of 15 metastatic melanoma patients treated with high dose IFNα revealed
559 that 44% exhibited myocardial injury, with biopsies showing significant interstitial edema, CM
560 vacuolization, mitochondrial swelling, and loss of cristae (Kruit et al., 1994). Collectively, these
561 findings link IFN-I to myocardial dysfunction, but the mechanisms by which IFNα causes
562 cardiomyopathy and how it synergizes with Doxo to promote DIC remain open questions of high
563 clinical significance. Surprisingly, we find that CMs are exquisitely sensitive to interferon, and we
564 observe that prolonged treatment of iPSC-CMs with recombinant IFN-I enhances the expression
565 of cardiac damage genes and induces changes in beat rate. Moreover, exposure of CMs to IFN-I
566 is sufficient to reduce expression of mtDNA-encoded OXPHOS transcripts. These data are
567 consistent with our prior work showing that elevated IFN-I signaling represses mtDNA
568 transcription and OXPHOS activity (Lei et al., 2021), and highlight the novel finding that Doxo
569 impairs mitochondrial function in CMs and cardiac tissue through elevated and sustained IFN-I
570 signaling. Moreover, we substantiate findings in non-tumor bearing mice and reveal that adjuvant
571 IFNα therapy synergizes with Doxo to enhance cardiac dysfunction in a physiologically relevant,
572 autochthonous model of melanoma. We reveal that IFNα significantly potentiates DIC by

573 exacerbating mitochondrial dysfunction, increasing fibrosis, and reducing cardiac output,
574 providing new insight into the cardiotoxic mechanisms of type I interferon.

575 Our in vitro and in vivo evidence collectively suggest that Doxo-induced mtDNA damage
576 triggers the ZBP1-STING-dependent production of IFN-I in cardiac cells and tissues, which in
577 turn drives a feed-forward loop of mitochondrial dysfunction that contributes to cardiac
578 remodeling and failure. Cardiac complications are frequently associated with both inherited
579 mitochondrial disorders and autoimmune diseases such type I interferonopathies and Lupus (Crow
580 et al., 2015; Frazier et al., 2021; Kim et al., 2017; Meyers et al., 2013). Recently, mutations in the
581 mtDNA maintenance factor ATAD3A have been demonstrated to cause a novel type I
582 interferonopathy characterized by mtDNA release and enhanced cGAS-STING signaling
583 (Lepelley et al., 2021b). Cardiac failure has been observed in some patients with ATAD3-mediated
584 mitochondrial disease, as well as in other interferonopathies (Crow and Stetson, 2021; Frazier et
585 al., 2021; Lei et al., 2021; Lepelley et al., 2021b, 2021a). Our data raises the interesting possibility
586 that persistent ZBP1-cGAS signaling and elevated IFN-I responses in CMs may directly promote
587 heart failure in mitochondrial diseases and interferonopathies characterized by mtDNA stress and
588 release. mtDNA-driven cGAS activation is also linked to IFN-I-mediated immunopathology in
589 COVID-19 (Di Domizio et al., 2022). Clinical manifestations of SARS-CoV-2 infected individuals
590 include acute cardiac damage as well as long-term cardiovascular sequelae in both hospitalized
591 and non-hospitalized individuals, yet the underlying mechanisms are largely unknown (Long et
592 al., 2020; Nalbandian et al., 2021; Xie et al., 2022). Our findings warrant the consideration of
593 cardiac mitochondrial damage and mtDNA release as a trigger of cGAS- and possibly ZBP1-
594 dependent IFN-I responses in myocarditis and other cardiac pathology in COVID-19.

595 In conclusion, we have uncovered ZBP1 as a key sensor of mtDNA stress that works
596 cooperatively with cGAS to sustain IFN-I responses in vitro and in vivo. Mechanistically, ZBP1
597 increases the cytosolic to nuclear cGAS ratio and amplifies cGAS activity in response to mtDNA
598 stress, likely via its ability to sense cytosolic Z-form DNA. Recent evidence has linked cGAS and
599 IFN-I to heart failure (Chen et al., 2019; King et al., 2017; Oka et al., 2012), yet a role for ZBP1
600 has not been explored. Our findings in two clinically relevant animal models 1) indicate the
601 presence of a previously uncharacterized IFN-I signaling program in cardiac cells and tissues
602 exposed to Doxo; 2) connect ZBP1-cGAS cytosolic DNA sensing to Doxo-induced IFN-I
603 responses in vivo; and 3) support the novel premise that the ZBP1-cGAS-IFNAR axis is a key
604 innate immune regulator of cardiotoxicity and heart dysfunction following Doxo chemotherapy.
605 ZBP1 may therefore represent a novel therapeutic target in chemotherapy-related cardiac
606 dysfunction, as well as other cardiovascular disorders where mtDNA stress sustains disease-
607 promoting IFN-I and inflammatory responses.
608

609 **ACKNOWLEDGEMENTS**

610 We thank Dr. Ken Ishii and Dr. Bill Kaiser for providing *Zbp1*$^{-/-}$ mice and members of the Tong,
611 Shadel, Upton, and West labs for helpful discussions and feedback on the manuscript. This work
612 was supported by NIH grants to A.P.W. (R01HL148153), C.W.T. (R01HL145534), P.L.
613 (R01AI145287), G.S.S. (R01AR069876 and R01CA216101) and J.W.U. (R21AI135709). G.S.S.
614 is the Audrey Geisel Chair in Biomedical Science. Y.L. was supported by an American Heart
615 Association Pre-Doctoral Fellowship (Grant 825908).
616

617 **AUTHOR CONTRIBUTIONS**

618 Y.L. and A.P.W. designed the experiments, analyzed the data, and wrote the manuscript. Y.L.
619 carried out most of the in vivo and in vitro assays, performed statistical analysis, and generated
620 figures. A.P.W. processed the RNA-Seq data and performed bioinformatic analyses. J.J.V. assisted
621 with molecular, biochemical, and immunofluorescence assays. Y.C. assisted with transcriptional
622 analysis of hiPSC-CMs and animal experiments. J.D.B. assisted with in vivo Doxo challenges.
623 K.B.R. and J.W.U. provided ZBP1 plasmids and advised on in vitro ZBP1 assays. C.W.T. provided
624 expertise and advice on cardiac measurements. L.C.W. performed melanoma induction and tumor
625 monitoring. P.L. provided expertise and reagents on cGAS studies. M.W.B. provided the inducible
626 melanoma model and advice on tumor induction and monitoring. G.S.S. provided the *Tfam*$^{+/-}$
627 mouse model and provided guidance on mtDNA assays. A.P.W. conceived the project and
628 provided overall supervision. All authors read and approved the manuscript.
629

630 **DECLARATION OF INTERESTS**

631 The authors declare that they have no competing interests.

632

633 **DATA AVAILABILITY**

634 All data needed to evaluate the conclusions drawn herein are present in the paper and/or the
635 Extended Data figures. Raw data will be provided upon request. RNA-Seq datasets will be
636 deposited to GEO upon acceptance of the manuscript.

637 **METHOD DETAILS**

638 **Mouse strains**

639 C57BL/6J (strain 000664), *Sting*$^{-/-}$ (*Sting1*^{gt}; strain 017537) and *Ifnar1*$^{-/-}$ (MMRRC Strain
640 #032045-JAX) mice were purchased from The Jackson Laboratory. *Mavs*$^{-/-}$ (strain 008634) mice
641 were purchased from The Jackson Laboratory and were backcrossed onto the C57BL/6J
642 background for 10 generations before use. *Tfam*$^{+/-}$ mice were previously reported (West et al.,
643 2015; Wu et al., 2019). *Zbp1*$^{-/-}$ mice (Ishii et al., 2008) were obtained collaboratively from Dr. Ken
644 Ishii. Breeding colonies of all strains were established and maintained on a pure C57BL/6J
645 background at Texas A&M University. Mice were group-housed in humidity-controlled
646 environments maintained at 22 °C on 12-hour light–dark cycles (600–1800). Food and water were
647 available ad libitum. All animal procedures were approved by the Texas A&M Animal Care and
648 Use Committee (TAMU IACUC) (Animal Use Protocol (AUP) 2017–0124). The euthanasia
649 methods employed in the study are consistent with the recommendations of the American
650 Veterinary Medical Association (AVMA).

651

652 **Reagents**

653 Doxorubicin (Adriamycin) HCl (S1208, Selleck Chemicals); Hydralazine Hydrochloride (H1289,
654 Spectrum); ISD (tlrl-isdn), poly(dA:dT) (tlrl-patn), poly(dG:dC) (tlrl-pgcn) (InvivoGen);
655 polyethylenimine, PEI (43896, Alfa Aesar); Human IFN Alpha Hybrid Protein (11200-1, PBL
656 Assay Science); Recombinant Human IFN-beta Protein (8499-IF-010), Recombinant Mouse IFN-
657 beta Protein (8234-MB-010) (R&D Systems); Recombinant Mouse IFN-α (752806, Biolegend);
658 *InVivo*Plus mouse IgG1 isotype control (BP0083), *InVivo*MAb anti-mouse IFNAR-1 (BE0241)

659 (Bio X Cell); 4-Hydroxytamoxifen (HB6040, hellobio); 2'3'-cGAMP ELISA Kit (501700,
660 Cayman); LDH Cytotoxicity Detection Kit (MK401, TaKaRa).
661
662 **Cell culture**
663 Primary WT, *Tfam*$^{+/-}$, *Zbp1*$^{-/-}$, and *Tfam*$^{+/-}$*Zbp1*$^{-/-}$ MEFs were generated from E12.5–14.5
664 embryos, maintained in DMEM (D5796, Sigma-Aldrich) supplemented with 10% FBS (97068-
665 085, VWR), and sub-cultured no more than five passages before experiments. Murine neonatal
666 cardiomyocytes were isolated from 2-3 day old neonates with Neonatal Cardiomyocyte Isolation
667 Kit (130-098-373, Miltenyi Biotec). Human iPSC-derived cardiomyocytes were purchased from
668 Fujifilm Cellular Dynamics (R1117) and cultured as described in the manual. 293FT was
669 purchased from Invitrogen (R70007), and COS-7 was purchased from ATCC (CRL-1651). siRNA
670 transfection was performed with 25 nM siRNA duplexes (Integrated DNA Techonologies) and 3
671 μL of Lipofectamine RNAiMAX reagent (13778150, ThermoFisher Scientific) according to the
672 manufacturer's protocol. DNA transfection was performed with Lipofectamine 2000 (11668019,
673 ThermoFisher Scientific) at a ratio of 2:1 Lipofectamine 2000 to nucleic acid according to the
674 manufacturer's protocol. All siRNA sequences used for transfection can be found in Table 1.
675
676 **Cloning and retroviral transduction**
677 Murine STING-His (InvivoGen) was subcloned into the pMXs-IRES-Puro vector and replication
678 incompetent retroviruses were packaged using Platinum-A cells (Cell Biolabs, RV-102) according
679 to the manufacturer's instructions. 293FT were exposed to supernatants containing pMXs-IRES-
680 Blast-STING-His retroviruses and 4 μg/mL polybrene (TR-1003-G, Millipore). Two days post
681 transduction, 10 μg/mL blasticidin was added to select a stable expression population.

682 Supernatants containing pWZL-hTERT-IRES-Blast retroviruses and 4 μg/mL polybrene were
683 incubated with human fibroblast (SCRC-1041, ATCC). Two days post transduction, 3 μg/mL
684 blasticidin was added to select a stable expression population. Mouse ZBP1 FL, ΔZα1, ΔZα1Zα2,
685 mRA, mRB and ΔC plasmids were previous described (Sridharan et al., 2017). All primer
686 sequences used for cloning in this study can be found in Table 2.
687
688 **Co-immunoprecipitation**
689 For Figures 2E and 2F, MEFs were treated with 10 ng/mL of mouse IFNβ for 6 hrs or in 50 nM
690 of Doxo for 48 hrs, respectively, before co-IP. The cytosolic fraction was obtained by lysing the
691 cells with NP-40 lysis buffer (50 mM Tris pH7.5, 0.15 M NaCl, 1 mM EDTA, 1% NP-40 and 10%
692 Glycerol), and nuclear fraction was acquired using Nuclear Complex co-IP kit (54001, Active
693 Motif), which allows a gentle release of DNA-bound protein complexes in the nucleus. Rabbit
694 TrueBlot® Set (88-1688-31, Rockland) was used for both pre-cleaning and co-IP from both
695 fractions. For co-IPs of cGAS and ZBP1 constructs in 293FT (Figures 2H, 2I, 2J, 3I and S2G,
696 S2H), Pierce™ Control Agarose Resin (26150, ThermoFisher Scientific) and Anti-DYKDDDDK
697 Tag (L5) Affinity Gel Antibody (651502, Biolegend) are used for pre-cleaning and IP, respectively.
698 Due to different subcellular localizations of cGAS mutants, the cytosolic fraction and nuclear
699 fraction were obtained as described above, combined and then used for co-IPs of cGAS mutants
700 and ZBP1 in 293FT (Figures S4G and S4H). To degrade cytosolic DNA in Figure 3H-I before co-
701 IP, samples were treated with 10 U/μL of benzonase (71205-3, Millipore) and incubated at 4 °C
702 for 4 hrs. BSA was added to the samples that were not treated with benzonase to even protein
703 concentration. 20 μL of sample was separated and the benzonase was inactivated by adding 0.5 μL

704 of 0.5 M EDTA and heating to 95 °C for 15 min. 10 ng/µL DNA from this portion was used in
705 qPCR to amplify mtDNA using primers against mt-ND1.
706
707 **Subcellular fractionation, DNA isolation and slot blotting**
708 3 x 10^6 MEFs were seeded in 15 cm dishes overnight and treated with vehicle or 500 nM of Doxo
709 for 24 hrs. Subcellular fractionation and DNA isolation were performed as previously described
710 (Bryant et al., 2022). In brief, cells were lysed in digitonin lysis buffer (150 mM NaCl, 50 mM
711 HEPES pH 7.4, and 5 µg/mL digitonin), incubated end over end for 10 min at 4 °C, and centrifuged
712 at 950 x g for 5 min at 4 °C. The cytosolic supernatants were transferred into a new tube and saved
713 as cytosolic fraction, and the pellets were lysed in NP-40 lysis buffer (50 mM Tris pH 7.5, 0.15 M
714 NaCl, 1 mM EDTA, 1% NP-40 and 10% Glycerol). After centrifugation of NP-40 lysates at 21130
715 x g for 10 min at 4 °C, the supernatants were transferred and saved as mitochondrial fraction, and
716 the nuclei pellets were further lysed in and SDS lysis buffer (20 mM Tris pH 8 and 1% SDS). SDS
717 lysates were boiled at 95 °C for 5 min and centrifuged at 21130 x g for 5 min at RT. The
718 supernatants were transferred and saved as nuclear fraction. All fractions were treated with 50
719 µg/mL of RNase A for 1.5 hrs at 37 °C and 200 µg/mL of Proteinase K for 1 h at 55 °C before
720 being subjected to Phenol-Chloroform based DNA isolation. After DNA isolation, 200 µg of
721 cytosolic DNA, 1 mg of mitochondrial DNA and 50 µg of nuclear DNA were blotted onto 0.45
722 µm Nylon membranes (10416230, Whatman). After air drying, membranes were incubated in
723 primary antibodies at 4 °C overnight in 1X PBS containing 1% casein, HRP-conjugated secondary
724 antibody at room temperature for 1 h, and then developed with Luminata Crescendo Western HRP
725 Substrate (WBLUR0500, Millipore).
726

727 **Quantitative PCR**

728 To measure relative gene expression by qRT–PCR in cells and tissues, total cellular RNA was
729 isolated using Quick-RNA microprep kit (R1051, Zymo Research). Approximately 0.5-1 μg RNA
730 was isolated, and cDNA was generated using the qScript cDNA Synthesis Kit (95047-100, Quanta).
731 cDNA was then subjected to qPCR using PerfeCTa SYBR Green FastMix (84069, Quanta).
732 Technical triplicates were run each biological sample, and average expression values were
733 normalized against *Rpl37* cDNA using the $2^{-\Delta\Delta CT}$ method (Bryant et al., 2022). For mtDNA
734 abundance assessment, 10 ng/μL of template DNA was used for qPCR, and expression values of
735 each replicate were normalized against nuclear-encoded *Tert or RNA18S* (Bryant et al., 2022). All
736 primer sequences used for qRT-PCR and qPCR can be found in Table 3 and 4.

737

738 **Immunoblotting**

739 Cells and tissues were lysed in NP-40 lysis buffer or SDS lysis buffer supplemented with protease
740 inhibitor (04693159001, Roche) and then centrifuged at 4 °C to obtain cellular lysate. After BCA
741 protein assay (23235, ThermoFisher Scientific), equal amounts of protein (10–40 μg) were loaded
742 into 10-20% SDS–PAGE gradient gels and transferred onto 0.22 μM PVDF membranes (1620177,
743 Bio-Rad). After air drying to return to a hydrophobic state, membranes were incubated in primary
744 antibodies at 4 °C overnight in 1X PBS containing 1% casein, HRP-conjugated secondary antibody
745 at room temperature for 1 h, and then developed with Luminata Crescendo Western HRP Substrate
746 (WBLUR0500, Millipore). All antibodies used for Immunoblotting can be found in Table 5. For
747 cGAS quantifications in Figures 2D, S2B and S2E, cytosolic cGAS expression was normalized to
748 GAPDH, and nuclear cGAS was normalized to LMNB1. These normalized values were used to

749 calculate the percentage of cGAS in the cytosolic (cytosolic cGAS/ total cGAS) and nuclear
750 (nuclear cGAS/ total cGAS) compartments.
751
752 **Immunofluorescence microscopy**
753 Cells were grown on coverslips and treated as described. After washing in PBS, cells were fixed
754 with 4% paraformaldehyde for 20 min, permeabilized with 0.1% Triton X-100 in PBS for 5 min,
755 blocked with PBS containing 5% FBS for 30 min, stained with primary antibodies for 1 h, and
756 stained with secondary antibodies for 1 h . Cells were washed with PBS containing 5% FBS
757 between each step. Coverslips were exposed to 200 ng/mL DAPI (62247, ThermoFisher Scientific)
758 for 2 min to label nuclei, then mounted with ProLong Diamond Antifade Mountant (P36961,
759 Invitrogen) and sealed with clear nail polish. For experiments requiring cytosolic signal
760 quantification, HSC CellMask Green (H32714, Invitrogen) was added to coverslips at 2 μg/mL
761 for 30 min, then washed several times in PBS, before DAPI staining. For Figure 4A, SYTOX
762 (MP33025, Invitrogen) was added to coverslips at 0.17 μM for 15 min, then washed in PBS. For
763 Figure 1F, images were acquired on a LSM 780 confocal microscope (Zeiss) with a 40x oil-
764 immersed objective and ZEN 3.3 software. For Figures 1E, 2A, 3A, 4A, 4B, 4E, 5A and S1M,
765 images were acquired on an ECLIPSE Ti2 (Nikon) with a 60x oil-immersed objective and NIS-
766 Elements AR 5.21.02 software. Representative images shown in Figures 1E, 2A, 4A-B, 4E, 5A
767 and S1M were imported into Huygens Essential software (v21.4.0) and deconvolved using the
768 'aggressive' profile in the Deconvolution Express application. Fluorescence intensity profiles in
769 Figures 2A and 3A were obtained from the NIS .nd2 files using the intensity analysis tool in NIS-
770 Elements AR 5.21.02. In Figures 2B, 3B and S3A, the nuclear cGAS intensity in each cell was
771 quantified within the DAPI positive area, and cytosolic cGAS intensity per cell was quantified in

772 the CellMask positive area minus the DAPI positive area. In Figures 4C and 4F, the non-nuclear
773 Z-DNA intensity per cell (cytosolic plus mitochondrial) was calculated from the CellMask positive
774 area minus the DAPI positive area. Z-DNA signals colocalizing with TOMM20 signals were
775 quantified as mitochondrial Z-DNA, while the remaining non-nuclear Z-DNA staining was
776 quantified as cytosolic Z-DNA. cGAS and Cellular Z-DNA intensity were quantified from
777 Nikon .nd2 files using NIS-Elements AR 5.21.02. All antibodies used for Immunofluorescence
778 microscopy can be found in Table 5.
779
780 **Doxorubicin administration**
781 Male and female mice between 8-10 weeks of age housed in a standard 12-hour light/dark cycle
782 with unlimited access to food and water. Doxorubicin stock solution (10 mg/mL) was prepared in
783 cell culture grade water (82007-330, VWR) and used within 28 days. Further dilutions were made
784 in DPBS (D8537, Sigma-Aldrich) on the day of injection. Intraperitoneal (i.p.) injection of
785 Doxorubicin (5 mg/kg body weight, 100 μL injection volume) was performed weekly for four
786 continuous weeks (cumulative dose 20 mg/kg body weight).
787
788 **Mouse melanoma induction, Doxorubicin and adjuvant IFNα therapy**
789 An autochthonous model of melanoma was utilized in Figures 6, and melanomas were induced on
790 21-day old mice as described in Dankort et al. 2009 (Dankort et al., 2009). First, mice were
791 anesthetized by isoflurane, then a commercial topical depilatory cream was applied to remove hair
792 from a 2 centimeter squared region on the lower dorsal region of mice approximately 2 centimeters
793 from the base of the tail. The next day, mice were anesthetized with isoflurane and 1 μL of a 20
794 mM solution of 4-hydroxytamoxifen dissolved in ethanol was applied topically to the exposed skin.

795 Four weeks after melanoma induction, hair was removed from the lower dorsal region of the mice
796 using hair trimmers to allow confirmation of tumor induction and monitoring of tumor growth.
797 Tumors were measured for width, length, and height every 2-4 days using digital calipers in order
798 to calculate tumor volume. Mice received vehicle (PBS) or Doxorubicin (5 mg/kg body weight,
799 100 μL i.p. injection volume) weekly for four consecutive weeks (cumulative dose 20 mg/kg body
800 weight). Adjuvant IFNα (20,000 units) was co-administrated together with Doxorubicin in a total
801 volume of 100 μL or diluted with PBS in a total volume of 50 μL and i.p. injected alone as
802 indicated in Figure 6B.
803
804 **Echocardiography**
805 Mice were depilated at the chest area the day before echocardiography measurements. Anesthesia
806 was induced by placing mice in a box with inhaled isoflurane at 2-3%. Afterwards, light anesthesia
807 was maintained using a nose cone with inhaled isoflurane at 0.5-1%. Mice were immobilized on a
808 heated stage, and continuous electric cardiogram (ECG), respiration, and temperature (via rectal
809 probe) were monitored. Light anesthesia and core temperature were maintained to ensure near
810 physiological status with heart rate at range of 470-520 beats per minute. Transthoracic
811 echocardiography was performed using a VisualSonics Vevo 3100 system with a MX550D
812 imaging transducer (center frequency of 40MHz). Parasternal long-axis (B-mode) and parasternal
813 short-axis (M-mode) views of each animal were taken. Vevo LAB cardiac analysis package was
814 used to analyze the data.
815
816 **Histology**

817 Mice were euthanized and tissues were washed in PBS and incubated for 24 h in 10% formalin
818 and then transferred to 70% ethanol. Tissue embedding, sectioning, and staining were performed
819 at AML Laboratories in St. Augustine, FL. Images of the H&E staining slides were acquired on
820 ECLIPSE Ts2 (Nikon) with a 20x or 40x objective. Blinded scoring of 9 independent fields of
821 view from 6 hearts per genotype and treatment was performed to determine percent of
822 cardiomyocytes exhibiting vacuolization post-Doxo. Collagen area was quantified using ImageJ.
823

824 **RNA sequencing and bioinformatic analyses**

825 Total cellular RNA from WT, *Tfam*$^{+/-}$, *Zbp1*$^{-/-}$ and *Tfam*$^{+/-}$*Zbp1*$^{-/-}$ MEFs was prepared using Quick-
826 RNA microprep kit (R1051, Zymo Research) and used for the Next-generation RNA sequencing
827 procedure at Texas A&M University Bioinformatics Core. RNA sequencing data were analyzed
828 using BaseSpace Sequence Hub (Illmina). In brief, STAR algorithm of RNAseq Alignment V2.0.0
829 software was utilized to align the results to reference genome Mus musculus/mm10 (RefSeq), then
830 RNA-seq Differential Expression V1.0.0 software was used to obtain raw gene expression files
831 and determine statistically significant changes in gene expression in *Tfam*$^{+/-}$, *Zbp1*$^{-/-}$ and *Tfam*$^{+/-}$
832 *Zbp1*$^{-/-}$ MEFs relative to WT. Heat maps were generated using GraphPad Prism. For Figures 5B,
833 5C and S4A, GSE40289 and GSE79413 datasets from the Gene Expression Omnibus (GEO) were
834 analyzed using Gene Set Enrichment Analysis software (Broad Institute) to identify differentially
835 regulated pathways, Set Comparison Appyter (Clarke et al., 2021) and Enrichr (Chen et al., 2013;
836 Kuleshov et al., 2016; Xie et al., 2021) to identify the interactions between datasets and
837 overlapping genes, or Ingenuity Pathway Analysis software (QIAGEN) to identify putative
838 upstream regulators and STING target genes in the datasets. Additional raw and analyzed datasets
839 will be deposited into the NCBI GEO upon acceptance of the manuscript.

840

841 **Statistical analyses**

842 Error bars displayed throughout the manuscript represent standard error of the mean (s.e.m.) and
843 were calculated from triplicates unless otherwise indicated. For ex vivo experiments, error bars
844 were calculated from the average of duplicate or triplicate technical replicates of at least 5 animals
845 per point. For microscopy quantification, images were taken throughout the slide of each sample
846 using the DAPI channel to avoid bias of selection. To reduce potential experimental bias, samples
847 for cardiac function (EF, FS, IVS;s, LVID;s, LVPW;s, LVPW;d and LV mass) and histological
848 analyses were blinded to researchers when performing analysis. The identities were only revealed
849 at the final data analysis stage. No randomization or blinding was used for all other animal studies.
850 No statistical method was used to predetermine sample size. Data shown are representative of at
851 least 3 independent experiments, including microscopy images, western blots, gene expression
852 analyses and all other cellular assays.

853 Aguirre, S., Luthra, P., Sanchez-Aparicio, M.T., Maestre, A.M., Patel, J., Lamothe, F.,
854 Fredericks, A.C., Tripathi, S., Zhu, T., Pintado-Silva, J., et al. (2017). Dengue virus NS2B
855 protein targets cGAS for degradation and prevents mitochondrial DNA sensing during infection.
856 Nat. Microbiol. *2*, 17037. https://doi.org/10.1038/nmicrobiol.2017.37.

857 Almine, J.F., O'Hare, C.A.J., Dunphy, G., Haga, I.R., Naik, R.J., Atrih, A., Connolly, D.J.,
858 Taylor, J., Kelsall, I.R., Bowie, A.G., et al. (2017). IFI16 and cGAS cooperate in the activation
859 of STING during DNA sensing in human keratinocytes. Nat. Commun. *8*, 14392.
860 https://doi.org/10.1038/ncomms14392.

861 Andreeva, L., Hiller, B., Kostrewa, D., Lässig, C., de Oliveira Mann, C.C., Jan Drexler, D.,
862 Maiser, A., Gaidt, M., Leonhardt, H., Hornung, V., et al. (2017). cGAS senses long and
863 HMGB/TFAM-bound U-turn DNA by forming protein-DNA ladders. Nature *549*, 394–398.
864 https://doi.org/10.1038/nature23890.

865 Angulo, M.P., Navajas, A., Galdeano, J.M., Astigarraga, I., and Fernández-Teijeiro, A. (1999).
866 Reversible cardiomyopathy secondary to alpha-interferon in an infant. Pediatr. Cardiol. *20*, 293–
867 294. https://doi.org/10.1007/s002469900467.

868 Ashley, N., and Poulton, J. (2009). Anticancer DNA intercalators cause p53-dependent
869 mitochondrial DNA nucleoid re-modelling. Oncogene *28*, 3880–3891.
870 https://doi.org/10.1038/onc.2009.242.

871 Baik, J.Y., Liu, Z., Jiao, D., Kwon, H.-J., Yan, J., Kadigamuwa, C., Choe, M., Lake, R., Kruhlak,
872 M., Tandon, M., et al. (2021). ZBP1 not RIPK1 mediates tumor necroptosis in breast cancer.
873 Nat. Commun. *12*, 1–14. https://doi.org/10.1038/s41467-021-23004-3.

874 Benjamini, O., Kimhi, O., and Lishner, M. (2007). Severe pleuropericarditis and cardiomyopathy
875 induced by high dose interferon alpha-2b. Isr. Med. Assoc. J. IMAJ *9*, 486–487. .

876 Bergen, H.R., Losman, M.J., O'Connor, T., Zacharias, W., Larson, J.E., Accavitti, M.A., Wells,
877 R.D., and Koopman, W.J. (1987). Specificity of monoclonal anti-Z-DNA antibodies from
878 unimmunized MRL/Mp-lpr/lpr mice. J. Immunol. Baltim. Md 1950 *139*, 743–748. .

879 Berthiaume, J.M., and Wallace, K.B. (2007). Adriamycin-induced oxidative mitochondrial
880 cardiotoxicity. Cell Biol. Toxicol. *23*, 15–25. https://doi.org/10.1007/s10565-006-0140-y.

881 Boyer, J.A., Spangler, C.J., Strauss, J.D., Cesmat, A.P., Liu, P., McGinty, R.K., and Zhang, Q.
882 (2020). Structural basis of nucleosome-dependent cGAS inhibition. Science *370*, 450–454.
883 https://doi.org/10.1126/science.abd0609.

884 Brault, M., Olsen, T.M., Martinez, J., Stetson, D.B., and Oberst, A. (2018). Intracellular nucleic
885 acid sensing triggers necroptosis through synergistic type-I interferon and TNF signaling. J.
886 Immunol. Baltim. Md 1950 *200*, 2748–2756. https://doi.org/10.4049/jimmunol.1701492.

887 Brown, B.A., Lowenhaupt, K., Wilbert, C.M., Hanlon, E.B., and Rich, A. (2000). The Zα
888 domain of the editing enzyme dsRNA adenosine deaminase binds left-handed Z-RNA as well as
889 Z-DNA. Proc. Natl. Acad. Sci. U. S. A. *97*, 13532–13536. .

890 Bryant, J.D., Lei, Y., VanPortfliet, J.J., Winters, A.D., and West, A.P. (2022). Assessing
891 Mitochondrial DNA Release into the Cytosol and Subsequent Activation of Innate Immune-
892 related Pathways in Mammalian Cells. Curr. Protoc. *2*, e372. https://doi.org/10.1002/cpz1.372.

893 Burridge, P.W., Li, Y.F., Matsa, E., Wu, H., Ong, S.-G., Sharma, A., Holmström, A., Chang,
894 A.C., Coronado, M.J., Ebert, A.D., et al. (2016). Human induced pluripotent stem cell-derived
895 cardiomyocytes recapitulate the predilection of breast cancer patients to doxorubicin-induced
896 cardiotoxicity. Nat. Med. *22*, 547–556. https://doi.org/10.1038/nm.4087.

897 Buzzo, J.R., Devaraj, A., Gloag, E.S., Jurcisek, J.A., Robledo-Avila, F., Kesler, T., Wilbanks,
898 K., Mashburn-Warren, L., Balu, S., Wickham, J., et al. (2021). Z-form extracellular DNA is a
899 structural component of the bacterial biofilm matrix. Cell *184*, 5740-5758.e17.
900 https://doi.org/10.1016/j.cell.2021.10.010.

901 Cao, D., Han, X., Fan, X., Xu, R.-M., and Zhang, X. (2020). Structural basis for nucleosome-
902 mediated inhibition of cGAS activity. Cell Res. *30*, 1088–1097. https://doi.org/10.1038/s41422-
903 020-00422-4.

904 Cao, D.J., Schiattarella, G.G., Villalobos, E., Jiang, N., May, H.I., Li, T., Chen, Z.J., Gillette,
905 T.G., and Hill, J.A. (2018). Cytosolic DNA Sensing Promotes Macrophage Transformation and
906 Governs Myocardial Ischemic Injury. Circulation *137*, 2613–2634.
907 https://doi.org/10.1161/CIRCULATIONAHA.117.031046.

908 Carvalho, F.S., Burgeiro, A., Garcia, R., Moreno, A.J., Carvalho, R.A., and Oliveira, P.J. (2014).
909 Doxorubicin-induced cardiotoxicity: from bioenergetic failure and cell death to cardiomyopathy.
910 Med. Res. Rev. *34*, 106–135. https://doi.org/10.1002/med.21280.

911 Chen, D., Tong, J., Yang, L., Wei, L., Stolz, D.B., Yu, J., Zhang, J., and Zhang, L. (2018).
912 PUMA amplifies necroptosis signaling by activating cytosolic DNA sensors. Proc. Natl. Acad.
913 Sci. *115*, 3930–3935. https://doi.org/10.1073/pnas.1717190115.

914 Chen, E.Y., Tan, C.M., Kou, Y., Duan, Q., Wang, Z., Meirelles, G.V., Clark, N.R., and Ma'ayan,
915 A. (2013). Enrichr: interactive and collaborative HTML5 gene list enrichment analysis tool.
916 BMC Bioinformatics *14*, 128. https://doi.org/10.1186/1471-2105-14-128.

917 Chen, H.-J., Tas, S.W., and de Winther, M.P.J. (2019). Type-I interferons in atherosclerosis. J.
918 Exp. Med. *217*, e20190459. https://doi.org/10.1084/jem.20190459.

919 Clarke, D.J.B., Jeon, M., Stein, D.J., Moiseyev, N., Kropiwnicki, E., Dai, C., Xie, Z.,
920 Wojciechowicz, M.L., Litz, S., Hom, J., et al. (2021). Appyters: Turning Jupyter Notebooks into
921 data-driven web apps. Patterns *2*, 100213. https://doi.org/10.1016/j.patter.2021.100213.

922 Crow, Y.J., and Stetson, D.B. (2021). The type I interferonopathies: 10 years on. Nat. Rev.
923 Immunol. 1–13. https://doi.org/10.1038/s41577-021-00633-9.

924 Crow, Y.J., Chase, D.S., Lowenstein Schmidt, J., Szynkiewicz, M., Forte, G.M.A., Gornall,
925 H.L., Oojageer, A., Anderson, B., Pizzino, A., Helman, G., et al. (2015). Characterization of
926 human disease phenotypes associated with mutations in TREX1, RNASEH2A, RNASEH2B,

927 RNASEH2C, SAMHD1, ADAR, and IFIH1. Am. J. Med. Genet. A. *167A*, 296–312.
928 https://doi.org/10.1002/ajmg.a.36887.

929 Damsky, W.E., Curley, D.P., Santhanakrishnan, M., Rosenbaum, L.E., Platt, J.T., Gould
930 Rothberg, B.E., Taketo, M.M., Dankort, D., Rimm, D.L., McMahon, M., et al. (2011). β-catenin
931 signaling controls metastasis in Braf-activated Pten-deficient melanomas. Cancer Cell *20*, 741–
932 754. https://doi.org/10.1016/j.ccr.2011.10.030.

933 Daniels, B.P., Kofman, S.B., Smith, J.R., Norris, G.T., Snyder, A.G., Kolb, J.P., Gao, X.,
934 Locasale, J.W., Martinez, J., Gale, M., et al. (2019). The Nucleotide Sensor ZBP1 and Kinase
935 RIPK3 Induce the Enzyme IRG1 to Promote an Antiviral Metabolic State in Neurons. Immunity
936 *50*, 64-76.e4. https://doi.org/10.1016/j.immuni.2018.11.017.

937 Dankort, D., Curley, D.P., Cartlidge, R.A., Nelson, B., Karnezis, A.N., Damsky, W.E., You,
938 M.J., DePinho, R.A., McMahon, M., and Bosenberg, M. (2009). BRafV600E cooperates with
939 Pten silencing to elicit metastatic melanoma. Nat. Genet. *41*, 544–552.
940 https://doi.org/10.1038/ng.356.

941 Decout, A., Katz, J.D., Venkatraman, S., and Ablasser, A. (2021). The cGAS–STING pathway
942 as a therapeutic target in inflammatory diseases. Nat. Rev. Immunol. *21*, 548–569.
943 https://doi.org/10.1038/s41577-021-00524-z.

944 DeFilippis, V.R., Alvarado, D., Sali, T., Rothenburg, S., and Früh, K. (2010). Human
945 Cytomegalovirus Induces the Interferon Response via the DNA Sensor ZBP1. J. Virol. *84*, 585–
946 598. https://doi.org/10.1128/JVI.01748-09.

947 Deigendesch, N., Koch-Nolte, F., and Rothenburg, S. (2006). ZBP1 subcellular localization and
948 association with stress granules is controlled by its Z-DNA binding domains. Nucleic Acids Res.
949 *34*, 5007–5020. https://doi.org/10.1093/nar/gkl575.

950 Devos, M., Tanghe, G., Gilbert, B., Dierick, E., Verheirstraeten, M., Nemegeer, J., de Reuver,
951 R., Lefebvre, S., De Munck, J., Rehwinkel, J., et al. (2020). Sensing of endogenous nucleic acids
952 by ZBP1 induces keratinocyte necroptosis and skin inflammation. J. Exp. Med. *217*, e20191913.
953 https://doi.org/10.1084/jem.20191913.

954 Dhir, A., Dhir, S., Borowski, L.S., Jimenez, L., Teitell, M., Rötig, A., Crow, Y.J., Rice, G.I.,
955 Duffy, D., Tamby, C., et al. (2018). Mitochondrial double-stranded RNA triggers antiviral
956 signalling in humans. Nature *560*, 238–242. https://doi.org/10.1038/s41586-018-0363-0.

957 Di Domizio, J., Gulen, M.F., Saidoune, F., Thacker, V.V., Yatim, A., Sharma, K., Nass, T.,
958 Guenova, E., Schaller, M., Conrad, C., et al. (2022). The cGAS-STING pathway drives type I
959 IFN immunopathology in COVID-19. Nature 1–9. https://doi.org/10.1038/s41586-022-04421-w.

960 Frantz, S., Falcao-Pires, I., Balligand, J.-L., Bauersachs, J., Brutsaert, D., Ciccarelli, M.,
961 Dawson, D., de Windt, L.J., Giacca, M., Hamdani, N., et al. (2018). The innate immune system
962 in chronic cardiomyopathy: a European Society of Cardiology (ESC) scientific statement from
963 the Working Group on Myocardial Function of the ESC. Eur. J. Heart Fail. *20*, 445–459.
964 https://doi.org/10.1002/ejhf.1138.

965 Frazier, A.E., Compton, A.G., Kishita, Y., Hock, D.H., Welch, A.E., Amarasekera, S.S.C., Rius,
966 R., Formosa, L.E., Imai-Okazaki, A., Francis, D., et al. (2021). Fatal Perinatal Mitochondrial
967 Cardiac Failure Caused by Recurrent De Novo Duplications in the ATAD3 Locus. Med *2*, 49-
968 73.e10. https://doi.org/10.1016/j.medj.2020.06.004.

969 Fu, Y., Comella, N., Tognazzi, K., Brown, L.F., Dvorak, H.F., and Kocher, O. (1999). Cloning
970 of DLM-1, a novel gene that is up-regulated in activated macrophages, using RNA differential
971 display. Gene *240*, 157–163. https://doi.org/10.1016/S0378-1119(99)00419-9.

972 Gentili, M., Lahaye, X., Nadalin, F., Nader, G.P.F., Puig Lombardi, E., Herve, S., De Silva, N.S.,
973 Rookhuizen, D.C., Zueva, E., Goudot, C., et al. (2019). The N-Terminal Domain of cGAS
974 Determines Preferential Association with Centromeric DNA and Innate Immune Activation in
975 the Nucleus. Cell Rep. *26*, 2377-2393.e13. https://doi.org/10.1016/j.celrep.2019.01.105.

976 Giordano, S.H., Lin, Y.-L., Kuo, Y.F., Hortobagyi, G.N., and Goodwin, J.S. (2012). Decline in
977 the use of anthracyclines for breast cancer. J. Clin. Oncol. Off. J. Am. Soc. Clin. Oncol. *30*,
978 2232–2239. https://doi.org/10.1200/JCO.2011.40.1273.

979 Guo, H., Gilley, R.P., Fisher, A., Lane, R., Landsteiner, V.J., Ragan, K.B., Dovey, C.M., Carette,
980 J.E., Upton, J.W., Mocarski, E.S., et al. (2018). Species-independent contribution of
981 ZBP1/DAI/DLM-1-triggered necroptosis in host defense against HSV1. Cell Death Dis. *9*, 1–11.
982 https://doi.org/10.1038/s41419-018-0868-3.

983 Ha, S.C., Van Quyen, D., Hwang, H.-Y., Oh, D.-B., Brown, B.A., Lee, S.M., Park, H.-J., Ahn,
984 J.-H., Kim, K.K., and Kim, Y.-G. (2006). Biochemical characterization and preliminary X-ray
985 crystallographic study of the domains of human ZBP1 bound to left-handed Z-DNA. Biochim.
986 Biophys. Acta *1764*, 320–323. https://doi.org/10.1016/j.bbapap.2005.12.012.

987 Ha, S.C., Kim, D., Hwang, H.-Y., Rich, A., Kim, Y.-G., and Kim, K.K. (2008). The crystal
988 structure of the second Z-DNA binding domain of human DAI (ZBP1) in complex with Z-DNA
989 reveals an unusual binding mode to Z-DNA. Proc. Natl. Acad. Sci. *105*, 20671–20676.
990 https://doi.org/10.1073/pnas.0810463106.

991 Helden, P.D.V. (1985). Potential Z-DNA-forming elements in serum DNA from human systemic
992 lupus erythematosus. J. Immunol. *134*, 177–179. .

993 Henriksen, P.A. (2018). Anthracycline cardiotoxicity: an update on mechanisms, monitoring and
994 prevention. Heart *104*, 971–977. https://doi.org/10.1136/heartjnl-2017-312103.

995 Herbert, A., and Rich, A. (1996). The Biology of Left-handed Z-DNA (∗). J. Biol. Chem. *271*,
996 11595–11598. https://doi.org/10.1074/jbc.271.20.11595.

997 Hooy, R.M., and Sohn, J. (2018). The allosteric activation of cGAS underpins its dynamic
998 signaling landscape. ELife *7*, e39984. https://doi.org/10.7554/eLife.39984.

999 Ingram, J.P., Thapa, R.J., Fisher, A., Tummers, B., Zhang, T., Yin, C., Rodriguez, D.A., Guo, H.,
1000 Lane, R., Williams, R., et al. (2019). ZBP1/DAI Drives RIPK3-Mediated Cell Death Induced by

1001 IFNs in the Absence of RIPK1. J. Immunol. *203*, 1348–1355.
1002 https://doi.org/10.4049/jimmunol.1900216.

1003 Ishii, K.J., Kawagoe, T., Koyama, S., Matsui, K., Kumar, H., Kawai, T., Uematsu, S., Takeuchi,
1004 O., Takeshita, F., Coban, C., et al. (2008). TANK-binding kinase-1 delineates innate and
1005 adaptive immune responses to DNA vaccines. Nature *451*, 725–729.
1006 https://doi.org/10.1038/nature06537.

1007 Jiao, H., Wachsmuth, L., Kumari, S., Schwarzer, R., Lin, J., Eren, R.O., Fisher, A., Lane, R.,
1008 Young, G.R., Kassiotis, G., et al. (2020). Z-nucleic-acid sensing triggers ZBP1-dependent
1009 necroptosis and inflammation. Nature *580*, 391–395. https://doi.org/10.1038/s41586-020-2129-8.

1010 Jønsson, K.L., Laustsen, A., Krapp, C., Skipper, K.A., Thavachelvam, K., Hotter, D., Egedal,
1011 J.H., Kjolby, M., Mohammadi, P., Prabakaran, T., et al. (2017). IFI16 is required for DNA
1012 sensing in human macrophages by promoting production and function of cGAMP. Nat.
1013 Commun. *8*, 14391. https://doi.org/10.1038/ncomms14391.

1014 Kaiser, W.J., Upton, J.W., and Mocarski, E.S. (2008). Receptor-interacting protein homotypic
1015 interaction motif-dependent control of NF-kappa B activation via the DNA-dependent activator
1016 of IFN regulatory factors. J. Immunol. Baltim. Md 1950 *181*, 6427–6434.
1017 https://doi.org/10.4049/jimmunol.181.9.6427.

1018 Keating, S.E., Baran, M., and Bowie, A.G. (2011). Cytosolic DNA sensors regulating type I
1019 interferon induction. Trends Immunol. *32*, 574–581. https://doi.org/10.1016/j.it.2011.08.004.

1020 Kesavardhana, S., and Kanneganti, T.-D. (2020). ZBP1: A STARGΛTE to decode the biology of
1021 Z-nucleic acids in disease. J. Exp. Med. *217*, e20200885. https://doi.org/10.1084/jem.20200885.

1022 Kesavardhana, S., Malireddi, R.K.S., Burton, A.R., Porter, S.N., Vogel, P., Pruett-Miller, S.M.,
1023 and Kanneganti, T.-D. (2020). The Zα2 domain of ZBP1 is a molecular switch regulating
1024 influenza-induced PANoptosis and perinatal lethality during development. J. Biol. Chem. *295*,
1025 8325–8330. https://doi.org/10.1074/jbc.RA120.013752.

1026 Khakoo, A.Y., Halushka, M.K., Rame, J.E., Rodriguez, E.R., Kasper, E.K., and Judge, D.P.
1027 (2005). Reversible cardiomyopathy caused by administration of interferon alpha. Nat. Clin.
1028 Pract. Cardiovasc. Med. *2*, 53–57. https://doi.org/10.1038/ncpcardio0069.

1029 Kim, C.H., Al-Kindi, S.G., Jandali, B., Askari, A.D., Zacharias, M., and Oliveira, G.H. (2017).
1030 Incidence and risk of heart failure in systemic lupus erythematosus. Heart Br. Card. Soc. *103*,
1031 227–233. https://doi.org/10.1136/heartjnl-2016-309561.

1032 King, K.R., Aguirre, A.D., Ye, Y.-X., Sun, Y., Roh, J.D., Ng, R.P., Kohler, R.H., Arlauckas,
1033 S.P., Iwamoto, Y., Savol, A., et al. (2017). IRF3 and type I interferons fuel a fatal response to
1034 myocardial infarction. Nat. Med. *23*, 1481–1487. https://doi.org/10.1038/nm.4428.

1035 Koehler, H., Cotsmire, S., Zhang, T., Balachandran, S., Upton, J.W., Langland, J., Kalman, D.,
1036 Jacobs, B.L., and Mocarski, E.S. (2021). Vaccinia virus E3 prevents sensing of Z-RNA to block

1037 ZBP1-dependent necroptosis. Cell Host Microbe *29*, 1266-1276.e5.
1038 https://doi.org/10.1016/j.chom.2021.05.009.

1039 Kruit, W.H., Punt, K.J., Goey, S.H., de Mulder, P.H., van Hoogenhuyze, D.C., Henzen-
1040 Logmans, S.C., and Stoter, G. (1994). Cardiotoxicity as a dose-limiting factor in a schedule of
1041 high dose bolus therapy with interleukin-2 and alpha-interferon. An unexpectedly frequent
1042 complication. Cancer *74*, 2850–2856. https://doi.org/10.1002/1097-
1043 0142(19941115)74:10<2850::aid-cncr2820741018>3.0.co;2-t.

1044 Kujirai, T., Zierhut, C., Takizawa, Y., Kim, R., Negishi, L., Uruma, N., Hirai, S., Funabiki, H.,
1045 and Kurumizaka, H. (2020). Structural basis for the inhibition of cGAS by nucleosomes. Science
1046 *370*, 455–458. https://doi.org/10.1126/science.abd0237.

1047 Kuleshov, M.V., Jones, M.R., Rouillard, A.D., Fernandez, N.F., Duan, Q., Wang, Z., Koplev, S.,
1048 Jenkins, S.L., Jagodnik, K.M., Lachmann, A., et al. (2016). Enrichr: a comprehensive gene set
1049 enrichment analysis web server 2016 update. Nucleic Acids Res. *44*, W90-97.
1050 https://doi.org/10.1093/nar/gkw377.

1051 Kuriakose, T., and Kanneganti, T.-D. (2018). ZBP1: Innate Sensor Regulating Cell Death and
1052 Inflammation. Trends Immunol. *39*, 123–134. https://doi.org/10.1016/j.it.2017.11.002.

1053 Kuriakose, T., Zheng, M., Neale, G., and Kanneganti, T.-D. (2018). IRF1 Is a Transcriptional
1054 Regulator of ZBP1 Promoting NLRP3 Inflammasome Activation and Cell Death during
1055 Influenza Virus Infection. J. Immunol. https://doi.org/10.4049/jimmunol.1701538.

1056 Kuwata, A., Ohashi, M., Sugiyama, M., Ueda, R., and Dohi, Y. (2002). A case of reversible
1057 dilated cardiomyopathy after alpha-interferon therapy in a patient with renal cell carcinoma. Am.
1058 J. Med. Sci. *324*, 331–334. https://doi.org/10.1097/00000441-200212000-00008.

1059 Lafer, E.M., Valle, R.P., Möller, A., Nordheim, A., Schur, P.H., Rich, A., and Stollar, B.D.
1060 (1983). Z-DNA-specific antibodies in human systemic lupus erythematosus. J. Clin. Invest. *71*,
1061 314–321. https://doi.org/10.1172/JCI110771.

1062 Lahaye, X., Gentili, M., Silvin, A., Conrad, C., Picard, L., Jouve, M., Zueva, E., Maurin, M.,
1063 Nadalin, F., Knott, G.J., et al. (2018). NONO Detects the Nuclear HIV Capsid to Promote cGAS-
1064 Mediated Innate Immune Activation. Cell *175*, 488-501.e22.
1065 https://doi.org/10.1016/j.cell.2018.08.062.

1066 Lebrecht, D., Setzer, B., Ketelsen, U.-P., Haberstroh, J., and Walker, U.A. (2003). Time-
1067 dependent and tissue-specific accumulation of mtDNA and respiratory chain defects in chronic
1068 doxorubicin cardiomyopathy. Circulation *108*, 2423–2429.
1069 https://doi.org/10.1161/01.CIR.0000093196.59829.DF.

1070 Ledur, P.F., Karmirian, K., Pedrosa, C. da S.G., Souza, L.R.Q., Assis-de-Lemos, G., Martins,
1071 T.M., Ferreira, J. de C.C.G., de Azevedo Reis, G.F., Silva, E.S., Silva, D., et al. (2020). Zika
1072 virus infection leads to mitochondrial failure, oxidative stress and DNA damage in human iPSC-
1073 derived astrocytes. Sci. Rep. *10*, 1218. https://doi.org/10.1038/s41598-020-57914-x.

1074 Lei, Y., Martinez, C.G., Torres-Odio, S., Bell, S.L., Birdwell, C.E., Bryant, J.D., Tong, C.W.,
1075 Watson, R.O., West, L.C., and West, A.P. (2021). Elevated type I interferon responses potentiate
1076 metabolic dysfunction, inflammation, and accelerated aging in mtDNA mutator mice. Sci. Adv.
1077 *7*, eabe7548. https://doi.org/10.1126/sciadv.abe7548.

1078 Lepelley, A., Wai, T., and Crow, Y.J. (2021a). Mitochondrial Nucleic Acid as a Driver of
1079 Pathogenic Type I Interferon Induction in Mendelian Disease. Front. Immunol. *12*. .

1080 Lepelley, A., Della Mina, E., Van Nieuwenhove, E., Waumans, L., Fraitag, S., Rice, G.I., Dhir,
1081 A., Frémond, M.-L., Rodero, M.P., Seabra, L., et al. (2021b). Enhanced cGAS-STING-
1082 dependent interferon signaling associated with mutations in ATAD3A. J. Exp. Med. *218*,
1083 e20201560. https://doi.org/10.1084/jem.20201560.

1084 Li, T., Huang, T., Du, M., Chen, X., Du, F., Ren, J., and Chen, Z.J. (2021). Phosphorylation and
1085 chromatin tethering prevent cGAS activation during mitosis. Science *371*, eabc5386.
1086 https://doi.org/10.1126/science.abc5386.

1087 Lindsey, M.L., Lange, R.A., Parsons, H., Andrews, T., and Aune, G.J. (2014). The tell-tale heart:
1088 molecular and cellular responses to childhood anthracycline exposure. Am. J. Physiol. - Heart
1089 Circ. Physiol. *307*, H1379–H1389. https://doi.org/10.1152/ajpheart.00099.2014.

1090 Lipshultz, S.E., Cochran, T.R., Franco, V.I., and Miller, T.L. (2013). Treatment-related
1091 cardiotoxicity in survivors of childhood cancer. Nat. Rev. Clin. Oncol. *10*, 697–710.
1092 https://doi.org/10.1038/nrclinonc.2013.195.

1093 Liu, H., Zhang, H., Wu, X., Ma, D., Wu, J., Wang, L., Jiang, Y., Fei, Y., Zhu, C., Tan, R., et al.
1094 (2018). Nuclear cGAS suppresses DNA repair and promotes tumorigenesis. Nature *563*, 131–
1095 136. https://doi.org/10.1038/s41586-018-0629-6.

1096 Long, B., Brady, W.J., Koyfman, A., and Gottlieb, M. (2020). Cardiovascular complications in
1097 COVID-19. Am. J. Emerg. Med. *38*, 1504–1507. https://doi.org/10.1016/j.ajem.2020.04.048.

1098 Maelfait, J., Liverpool, L., Bridgeman, A., Ragan, K.B., Upton, J.W., and Rehwinkel, J. (2017).
1099 Sensing of viral and endogenous RNA by ZBP1/DAI induces necroptosis. EMBO J. *36*, 2529–
1100 2543. https://doi.org/10.15252/embj.201796476.

1101 Mancilla, T.R., Iskra, B., and Aune, G.J. (2019). Doxorubicin-Induced Cardiomyopathy in
1102 Children. Compr. Physiol. *9*, 905–931. https://doi.org/10.1002/cphy.c180017.

1103 Matsui, H., Ito, J., Matsui, N., Uechi, T., Onodera, O., and Kakita, A. (2021). Cytosolic dsDNA
1104 of mitochondrial origin induces cytotoxicity and neurodegeneration in cellular and zebrafish
1105 models of Parkinson's disease. Nat. Commun. *12*, 3101. https://doi.org/10.1038/s41467-021-
1106 23452-x.

1107 McNab, F., Mayer-Barber, K., Sher, A., Wack, A., and O'Garra, A. (2015). Type I interferons in
1108 infectious disease. Nat. Rev. Immunol. *15*, 87–103. https://doi.org/10.1038/nri3787.

1109 Mehta, L.S., Watson, K.E., Barac, A., Beckie, T.M., Bittner, V., Cruz-Flores, S., Dent, S.,
1110 Kondapalli, L., Ky, B., Okwuosa, T., et al. (2018). Cardiovascular Disease and Breast Cancer:
1111 Where These Entities Intersect: A Scientific Statement From the American Heart Association.
1112 Circulation *137*, e30–e66. https://doi.org/10.1161/CIR.0000000000000556.

1113 Meléndez, G.C., Jordan, J.H., D'Agostino, R.B., Lesnefsky, E.J., and Hundley, W.G. (2018).
1114 Accelerated Left Ventricular Interstitial Collagen Deposition After Receiving Doxorubicin
1115 in Hypertension. J. Am. Coll. Cardiol. *72*, 1555–1557.
1116 https://doi.org/10.1016/j.jacc.2018.07.028.

1117 Meyers, D.E., Basha, H.I., and Koenig, M.K. (2013). Mitochondrial Cardiomyopathy. Tex. Heart
1118 Inst. J. *40*, 385–394. .

1119 Michalski, S., de Oliveira Mann, C.C., Stafford, C.A., Witte, G., Bartho, J., Lammens, K.,
1120 Hornung, V., and Hopfner, K.-P. (2020). Structural basis for sequestration and autoinhibition of
1121 cGAS by chromatin. Nature *587*, 678–682. https://doi.org/10.1038/s41586-020-2748-0.

1122 Möller, A., Gabriels, J.E., Lafer, E.M., Nordheim, A., Rich, A., and Stollar, B.D. (1982).
1123 Monoclonal antibodies recognize different parts of Z-DNA. J. Biol. Chem. *257*, 12081–12085. .

1124 Moudgil, R., and Yeh, E.T.H. (2016). Mechanisms of Cardiotoxicity of Cancer
1125 Chemotherapeutic Agents: Cardiomyopathy and Beyond. Can. J. Cardiol. *32*, 863-870.e5.
1126 https://doi.org/10.1016/j.cjca.2016.01.027.

1127 Nakayama, H., and Otsu, K. (2018). Mitochondrial DNA as an inflammatory mediator in
1128 cardiovascular diseases. Biochem. J. *475*, 839–852. https://doi.org/10.1042/BCJ20170714.

1129 Nalbandian, A., Sehgal, K., Gupta, A., Madhavan, M.V., McGroder, C., Stevens, J.S., Cook,
1130 J.R., Nordvig, A.S., Shalev, D., Sehrawat, T.S., et al. (2021). Post-acute COVID-19 syndrome.
1131 Nat. Med. *27*, 601–615. https://doi.org/10.1038/s41591-021-01283-z.

1132 Nathan, P.C., Amir, E., and Abdel-Qadir, H. (2016). Cardiac Outcomes in Survivors of Pediatric
1133 and Adult Cancers. Can. J. Cardiol. *32*, 871–880. https://doi.org/10.1016/j.cjca.2016.02.065.

1134 Oka, T., Hikoso, S., Yamaguchi, O., Taneike, M., Takeda, T., Tamai, T., Oyabu, J., Murakawa,
1135 T., Nakayama, H., Nishida, K., et al. (2012). Mitochondrial DNA that escapes from autophagy
1136 causes inflammation and heart failure. Nature *485*, 251–255.
1137 https://doi.org/10.1038/nature10992.

1138 Oliveira, P.H., Lobato da Silva, C., and Cabral, J.M.S. (2013). An Appraisal of Human
1139 Mitochondrial DNA Instability: New Insights into the Role of Non-Canonical DNA Structures
1140 and Sequence Motifs. PLoS ONE *8*, e59907. https://doi.org/10.1371/journal.pone.0059907.

1141 Parra, H.S., Tixi, L., Latteri, F., Bretti, S., Alloisio, M., Gravina, A., Lionetto, R., Bruzzi, P.,
1142 Dani, C., Rosso, R., et al. (2001). Combined regimen of cisplatin, doxorubicin, and alpha-2b
1143 interferon in the treatment of advanced malignant pleural mesothelioma: a Phase II multicenter
1144 trial of the Italian Group on Rare Tumors (GITR) and the Italian Lung Cancer Task Force

1145 (FONICAP). Cancer *92*, 650–656. https://doi.org/10.1002/1097-0142(20010801)92:3<650::aid-
1146 cncr1366>3.0.co;2-0.

1147 Pathare, G.R., Decout, A., Glück, S., Cavadini, S., Makasheva, K., Hovius, R., Kempf, G.,
1148 Weiss, J., Kozicka, Z., Guey, B., et al. (2020). Structural mechanism of cGAS inhibition by the
1149 nucleosome. Nature *587*, 668–672. https://doi.org/10.1038/s41586-020-2750-6.

1150 Raj, S., Franco, V.I., and Lipshultz, S.E. (2014). Anthracycline-Induced Cardiotoxicity: A
1151 Review of Pathophysiology, Diagnosis, and Treatment. Curr. Treat. Options Cardiovasc. Med.
1152 *16*, 315. https://doi.org/10.1007/s11936-014-0315-4.

1153 Ravichandran, S., Subramani, V.K., and Kim, K.K. (2019). Z-DNA in the genome: from
1154 structure to disease. Biophys. Rev. *11*, 383–387. https://doi.org/10.1007/s12551-019-00534-1.

1155 Riley, J.S., and Tait, S.W. (2020). Mitochondrial DNA in inflammation and immunity. EMBO
1156 Rep. *21*. https://doi.org/10.15252/embr.201949799.

1157 Rodríguez-Nuevo, A., Díaz-Ramos, A., Noguera, E., Díaz-Sáez, F., Duran, X., Muñoz, J.P.,
1158 Romero, M., Plana, N., Sebastián, D., Tezze, C., et al. (2018). Mitochondrial DNA and TLR9
1159 drive muscle inflammation upon Opa1 deficiency. EMBO J. *37*.
1160 https://doi.org/10.15252/embj.201796553.

1161 Rongvaux, A., Jackson, R., Harman, C.C.D., Li, T., West, A.P., de Zoete, M.R., Wu, Y., Yordy,
1162 B., Lakhani, S.A., Kuan, C.-Y., et al. (2014). Apoptotic caspases prevent the induction of type I
1163 interferons by mitochondrial DNA. Cell *159*, 1563–1577.
1164 https://doi.org/10.1016/j.cell.2014.11.037.

1165 Saada, J., McAuley, R.J., Marcatti, M., Tang, T.Z., Motamedi, M., and Szczesny, B. (2022).
1166 Oxidative stress induces Z-DNA-binding protein 1–dependent activation of microglia via
1167 mtDNA released from retinal pigment epithelial cells. J. Biol. Chem. *298*.
1168 https://doi.org/10.1016/j.jbc.2021.101523.

1169 Sarhan, J., Liu, B.C., Muendlein, H.I., Weindel, C.G., Smirnova, I., Tang, A.Y., Ilyukha, V.,
1170 Sorokin, M., Buzdin, A., Fitzgerald, K.A., et al. (2019). Constitutive interferon signaling
1171 maintains critical threshold of MLKL expression to license necroptosis. Cell Death Differ. *26*,
1172 332–347. https://doi.org/10.1038/s41418-018-0122-7.

1173 Schneider, W.M., Chevillotte, M.D., and Rice, C.M. (2014). Interferon-Stimulated Genes: A
1174 Complex Web of Host Defenses. Annu. Rev. Immunol. *32*, 513–545.
1175 https://doi.org/10.1146/annurev-immunol-032713-120231.

1176 Schwartz, T., Behlke, J., Lowenhaupt, K., Heinemann, U., and Rich, A. (2001). Structure of the
1177 DLM-1–Z-DNA complex reveals a conserved family of Z-DNA-binding proteins. Nat. Struct.
1178 Biol. *8*, 761–765. https://doi.org/10.1038/nsb0901-761.

1179 Serrano, J., Palmeira, C.M., Kuehl, D.W., and Wallace, K.B. (1999). Cardioselective and
1180 cumulative oxidation of mitochondrial DNA following subchronic doxorubicin administration.
1181 Biochim. Biophys. Acta *1411*, 201–205. https://doi.org/10.1016/s0005-2728(99)00011-0.

1182 Sibley, J.T., Lee, J.S., and Decoteau, W.E. (1984). Left-handed "Z" DNA antibodies in
1183 rheumatoid arthritis and systemic lupus erythematosus. J. Rheumatol. *11*, 633–637. .

1184 Sistigu, A., Yamazaki, T., Vacchelli, E., Chaba, K., Enot, D.P., Adam, J., Vitale, I., Goubar, A.,
1185 Baracco, E.E., Remédios, C., et al. (2014). Cancer cell-autonomous contribution of type I
1186 interferon signaling to the efficacy of chemotherapy. Nat. Med. *20*, 1301–1309.
1187 https://doi.org/10.1038/nm.3708.

1188 Sridharan, H., Ragan, K.B., Guo, H., Gilley, R.P., Landsteiner, V.J., Kaiser, W.J., and Upton,
1189 J.W. (2017). Murine cytomegalovirus IE3-dependent transcription is required for DAI/ZBP1-
1190 mediated necroptosis. EMBO Rep. *18*, 1429–1441. https://doi.org/10.15252/embr.201743947.

1191 Sun, B., Sundström, K.B., Chew, J.J., Bist, P., Gan, E.S., Tan, H.C., Goh, K.C., Chawla, T.,
1192 Tang, C.K., and Ooi, E.E. (2017). Dengue virus activates cGAS through the release of
1193 mitochondrial DNA. Sci. Rep. *7*, 3594. https://doi.org/10.1038/s41598-017-03932-1.

1194 Sun, H., Huang, Y., Mei, S., Xu, F., Liu, X., Zhao, F., Yin, L., Zhang, D., Wei, L., Wu, C., et al.
1195 (2021). A Nuclear Export Signal Is Required for cGAS to Sense Cytosolic DNA. Cell Rep. *34*,
1196 108586. https://doi.org/10.1016/j.celrep.2020.108586.

1197 Suram, A., Rao, J.K.S., Latha, K.S., and Viswamitra, M.A. (2002). First evidence to show the
1198 topological change of DNA from B-DNA to Z-DNA conformation in the hippocampus of
1199 Alzheimer's brain. NeuroMolecular Med. *2*, 289–297. https://doi.org/10.1385/NMM:2:3:289.

1200 Szczesny, B., Marcatti, M., Ahmad, A., Montalbano, M., Brunyánszki, A., Bibli, S.-I.,
1201 Papapetropoulos, A., and Szabo, C. (2018). Mitochondrial DNA damage and subsequent
1202 activation of Z-DNA binding protein 1 links oxidative stress to inflammation in epithelial cells.
1203 Sci. Rep. *8*, 914. https://doi.org/10.1038/s41598-018-19216-1.

1204 Takaoka, A., Wang, Z., Choi, M.K., Yanai, H., Negishi, H., Ban, T., Lu, Y., Miyagishi, M.,
1205 Kodama, T., Honda, K., et al. (2007). DAI (DLM-1/ZBP1) is a cytosolic DNA sensor and an
1206 activator of innate immune response. Nature *448*, 501–505. https://doi.org/10.1038/nature06013.

1207 Thomas, T.J., Gunnia, U.B., and Thomas, T. (1991). Polyamine-induced B-DNA to Z-DNA
1208 conformational transition of a plasmid DNA with (dG-dC)n insert. J. Biol. Chem. *266*, 6137–
1209 6141. https://doi.org/10.1016/S0021-9258(18)38095-5.

1210 Thomas, T.J., Seibold, J.R., Adams, L.E., and Hess, E.V. (1993). Hydralazine induces Z-DNA
1211 conformation in a polynucleotide and elicits anti(Z-DNA) antibodies in treated patients.
1212 Biochem. J. *294*, 419–425. .

1213 Tigano, M., Vargas, D.C., Tremblay-Belzile, S., Fu, Y., and Sfeir, A. (2021). Nuclear sensing of
1214 breaks in mitochondrial DNA enhances immune surveillance. Nature *591*, 477–481.
1215 https://doi.org/10.1038/s41586-021-03269-w.

1216 Timlin, H., Wu, M., Crespo-Bosque, M., Geetha, D., Ingolia, A., Haque, U., Towns, M.C., and
1217 Grader-Beck, T. (2019). Clinical Characteristics of Hydralazine-induced Lupus. Cureus *11*,
1218 e4996. https://doi.org/10.7759/cureus.4996.

1219 Triantafilou, K., Eryilmazlar, D., and Triantafilou, M. (2014). Herpes simplex virus 2-induced
1220 activation in vaginal cells involves Toll-like receptors 2 and 9 and DNA sensors DAI and IFI16.
1221 Am. J. Obstet. Gynecol. *210*, 122.e1-122.e10. https://doi.org/10.1016/j.ajog.2013.09.034.

1222 Upton, J.W., Kaiser, W.J., and Mocarski, E.S. (2012). DAI/ZBP1/DLM-1 complexes with RIP3
1223 to mediate virus-induced programmed necrosis that is targeted by murine cytomegalovirus vIRA.
1224 Cell Host Microbe *11*, 290–297. https://doi.org/10.1016/j.chom.2012.01.016.

1225 Vejpongsa, P., and Yeh, E.T.H. (2014). Prevention of anthracycline-induced cardiotoxicity:
1226 challenges and opportunities. J. Am. Coll. Cardiol. *64*, 938–945.
1227 https://doi.org/10.1016/j.jacc.2014.06.1167.

1228 Volkman, H.E., Cambier, S., Gray, E.E., and Stetson, D.B. (2019). Tight nuclear tethering of
1229 cGAS is essential for preventing autoreactivity. ELife *8*, e47491.
1230 https://doi.org/10.7554/eLife.47491.

1231 Volkova, M., and Russell, R. (2011). Anthracycline Cardiotoxicity: Prevalence, Pathogenesis
1232 and Treatment. Curr. Cardiol. Rev. *7*, 214–220. https://doi.org/10.2174/157340311799960645.

1233 Wallace, K.B., Sardão, V.A., and Oliveira, P.J. (2020). Mitochondrial Determinants of
1234 Doxorubicin-Induced Cardiomyopathy. Circ. Res. *126*, 926–941.
1235 https://doi.org/10.1161/CIRCRESAHA.119.314681.

1236 Wang, G., and Vasquez, K.M. (2007). Z-DNA, an active element in the genome. Front. Biosci. J.
1237 Virtual Libr. *12*, 4424–4438. https://doi.org/10.2741/2399.

1238 Wang, A.H.-J., Quigley, G.J., Kolpak, F.J., Crawford, J.L., van Boom, J.H., van der Marel, G.,
1239 and Rich, A. (1979). Molecular structure of a left-handed double helical DNA fragment at
1240 atomic resolution. Nature *282*, 680–686. https://doi.org/10.1038/282680a0.

1241 Wang, Z., Choi, M.K., Ban, T., Yanai, H., Negishi, H., Lu, Y., Tamura, T., Takaoka, A.,
1242 Nishikura, K., and Taniguchi, T. (2008). Regulation of innate immune responses by DAI (DLM-
1243 1/ZBP1) and other DNA-sensing molecules. Proc. Natl. Acad. Sci. *105*, 5477–5482.
1244 https://doi.org/10.1073/pnas.0801295105.

1245 West, A.P. (2017). Mitochondrial dysfunction as a trigger of innate immune responses and
1246 inflammation. Toxicology *391*, 54–63. https://doi.org/10.1016/j.tox.2017.07.016.

1247 West, A.P., and Shadel, G.S. (2017). Mitochondrial DNA in innate immune responses and
1248 inflammatory pathology. Nat. Rev. Immunol. *17*, 363–375. https://doi.org/10.1038/nri.2017.21.

1249 West, A.P., Khoury-Hanold, W., Staron, M., Tal, M.C., Pineda, C.M., Lang, S.M., Bestwick, M.,
1250 Duguay, B.A., Raimundo, N., MacDuff, D.A., et al. (2015). Mitochondrial DNA stress primes
1251 the antiviral innate immune response. Nature *520*, 553–557. https://doi.org/10.1038/nature14156.

1252 White, M.J., McArthur, K., Metcalf, D., Lane, R.M., Cambier, J.C., Herold, M.J., van Delft,
1253 M.F., Bedoui, S., Lessene, G., Ritchie, M.E., et al. (2014). Apoptotic Caspases Suppress

1254 mtDNA-Induced STING-Mediated Type I IFN Production. Cell *159*, 1549–1562.
1255 https://doi.org/10.1016/j.cell.2014.11.036.

1256 Woo, D.K., Green, P.D., Santos, J.H., D'Souza, A.D., Walther, Z., Martin, W.D., Christian, B.E.,
1257 Chandel, N.S., and Shadel, G.S. (2012). Mitochondrial Genome Instability and ROS Enhance
1258 Intestinal Tumorigenesis in APCMin/+ Mice. Am. J. Pathol. *180*, 24–31.
1259 https://doi.org/10.1016/j.ajpath.2011.10.003.

1260 Wu, D., Sanin, D.E., Everts, B., Chen, Q., Qiu, J., Buck, M.D., Patterson, A., Smith, A.M.,
1261 Chang, C.-H., Liu, Z., et al. (2016). Type 1 interferons induce changes in core metabolism that
1262 are critical for immune function. Immunity *44*, 1325–1336.
1263 https://doi.org/10.1016/j.immuni.2016.06.006.

1264 Wu, Z., Oeck, S., West, A.P., Mangalhara, K.C., Sainz, A.G., Newman, L.E., Zhang, X.-O., Wu,
1265 L., Yan, Q., Bosenberg, M., et al. (2019). Mitochondrial DNA stress signalling protects the
1266 nuclear genome. Nat. Metab. *1*, 1209–1218. https://doi.org/10.1038/s42255-019-0150-8.

1267 Xie, Y., Xu, E., Bowe, B., and Al-Aly, Z. (2022). Long-term cardiovascular outcomes of
1268 COVID-19. Nat. Med. *28*, 583–590. https://doi.org/10.1038/s41591-022-01689-3.

1269 Xie, Z., Bailey, A., Kuleshov, M.V., Clarke, D.J.B., Evangelista, J.E., Jenkins, S.L., Lachmann,
1270 A., Wojciechowicz, M.L., Kropiwnicki, E., Jagodnik, K.M., et al. (2021). Gene Set Knowledge
1271 Discovery with Enrichr. Curr. Protoc. *1*, e90. https://doi.org/10.1002/cpz1.90.

1272 Yang, Y., Wu, M., Cao, D., Yang, C., Jin, J., Wu, L., Hong, X., Li, W., Lu, L., Li, J., et al.
1273 (2021). ZBP1-MLKL necroptotic signaling potentiates radiation-induced antitumor immunity via
1274 intratumoral STING pathway activation. Sci. Adv. *7*, eabf6290.
1275 https://doi.org/10.1126/sciadv.abf6290.

1276 Yau, C., Low, J.Z.H., Gan, E.S., Kwek, S.S., Cui, L., Tan, H.C., Mok, D.Z.L., Chan, C.Y.Y.,
1277 Sessions, O.M., Watanabe, S., et al. (2021). Dysregulated metabolism underpins Zika-virus-
1278 infection-associated impairment in fetal development. Cell Rep. *37*, 110118.
1279 https://doi.org/10.1016/j.celrep.2021.110118.

1280 Yen, H.C., Oberley, T.D., Gairola, C.G., Szweda, L.I., and St Clair, D.K. (1999). Manganese
1281 superoxide dismutase protects mitochondrial complex I against adriamycin-induced
1282 cardiomyopathy in transgenic mice. Arch. Biochem. Biophys. *362*, 59–66.
1283 https://doi.org/10.1006/abbi.1998.1011.

1284 Yeo, W., Mok, T.S., Zee, B., Leung, T.W.T., Lai, P.B.S., Lau, W.Y., Koh, J., Mo, F.K.F., Yu,
1285 S.C.H., Chan, A.T., et al. (2005). A randomized phase III study of doxorubicin versus
1286 cisplatin/interferon alpha-2b/doxorubicin/fluorouracil (PIAF) combination chemotherapy for
1287 unresectable hepatocellular carcinoma. J. Natl. Cancer Inst. *97*, 1532–1538.
1288 https://doi.org/10.1093/jnci/dji315.

1289 Yu, R., Zhu, B., and Chen, D. (2022). Type I interferon-mediated tumor immunity and its role in
1290 immunotherapy. Cell. Mol. Life Sci. *79*, 191. https://doi.org/10.1007/s00018-022-04219-z.

1291 Zhang, S., Liu, X., Bawa-Khalfe, T., Lu, L.-S., Lyu, Y.L., Liu, L.F., and Yeh, E.T.H. (2012).
1292 Identification of the molecular basis of doxorubicin-induced cardiotoxicity. Nat. Med. *18*, 1639–
1293 1642. https://doi.org/10.1038/nm.2919.

1294 Zhang, T., Yin, C., Boyd, D.F., Quarato, G., Ingram, J.P., Shubina, M., Ragan, K.B., Ishizuka,
1295 T., Crawford, J.C., Tummers, B., et al. (2020). Influenza Virus Z-RNAs Induce ZBP1-Mediated
1296 Necroptosis. Cell *180*, 1115-1129.e13. https://doi.org/10.1016/j.cell.2020.02.050.

1297 Zhang, Z., Meng, P., Han, Y., Shen, C., Li, B., Hakim, M.A., Zhang, X., Lu, Q., Rong, M., and
1298 Lai, R. (2015). Mitochondrial DNA-LL-37 Complex Promotes Atherosclerosis by Escaping from
1299 Autophagic Recognition. Immunity *43*, 1137–1147.
1300 https://doi.org/10.1016/j.immuni.2015.10.018.

1301 Zhao, B., Xu, P., Rowlett, C.M., Jing, T., Shinde, O., Lei, Y., West, A.P., Liu, W.R., and Li, P.
1302 (2020). The molecular basis of tight nuclear tethering and inactivation of cGAS. Nature *587*,
1303 673–677. https://doi.org/10.1038/s41586-020-2749-z.

1304 Zhao, M., Xia, T., Xing, J.-Q., Yin, L.-H., Li, X.-W., Pan, J., Liu, J.-Y., Sun, L.-M., Wang, M.,
1305 Li, T., et al. (2022). The stress granule protein G3BP1 promotes pre-condensation of cGAS to
1306 allow rapid responses to DNA. EMBO Rep. *23*, e53166.
1307 https://doi.org/10.15252/embr.202153166.

1308 Zhao, W., Ji, F., Yu, S., Li, Z., and Deng, H. (2014). Dilated cardiomyopathy and
1309 hypothyroidism associated with pegylated interferon and ribavirin treatment for chronic hepatitis
1310 C: case report and literature review. Braz. J. Infect. Dis. Off. Publ. Braz. Soc. Infect. Dis. *18*,
1311 110–113. https://doi.org/10.1016/j.bjid.2013.05.014.

1312 Zhou, S., Palmeira, C.M., and Wallace, K.B. (2001). Doxorubicin-induced persistent oxidative
1313 stress to cardiac myocytes. Toxicol. Lett. *121*, 151–157. https://doi.org/10.1016/s0378-
1314 4274(01)00329-0.

1315 Zierhut, C., and Funabiki, H. (2020). Regulation and Consequences of cGAS Activation by Self-
1316 DNA. Trends Cell Biol. *30*, 594–605. https://doi.org/10.1016/j.tcb.2020.05.006.

1317 Zimmerman, S., Adkins, D., Graham, M., Petruska, P., Bowers, C., Vrahnos, D., and Spitzer, G.
1318 (1994). Irreversible, severe congestive cardiomyopathy occurring in association with interferon
1319 alpha therapy. Cancer Biother. *9*, 291–299. https://doi.org/10.1089/cbr.1994.9.291.

1320

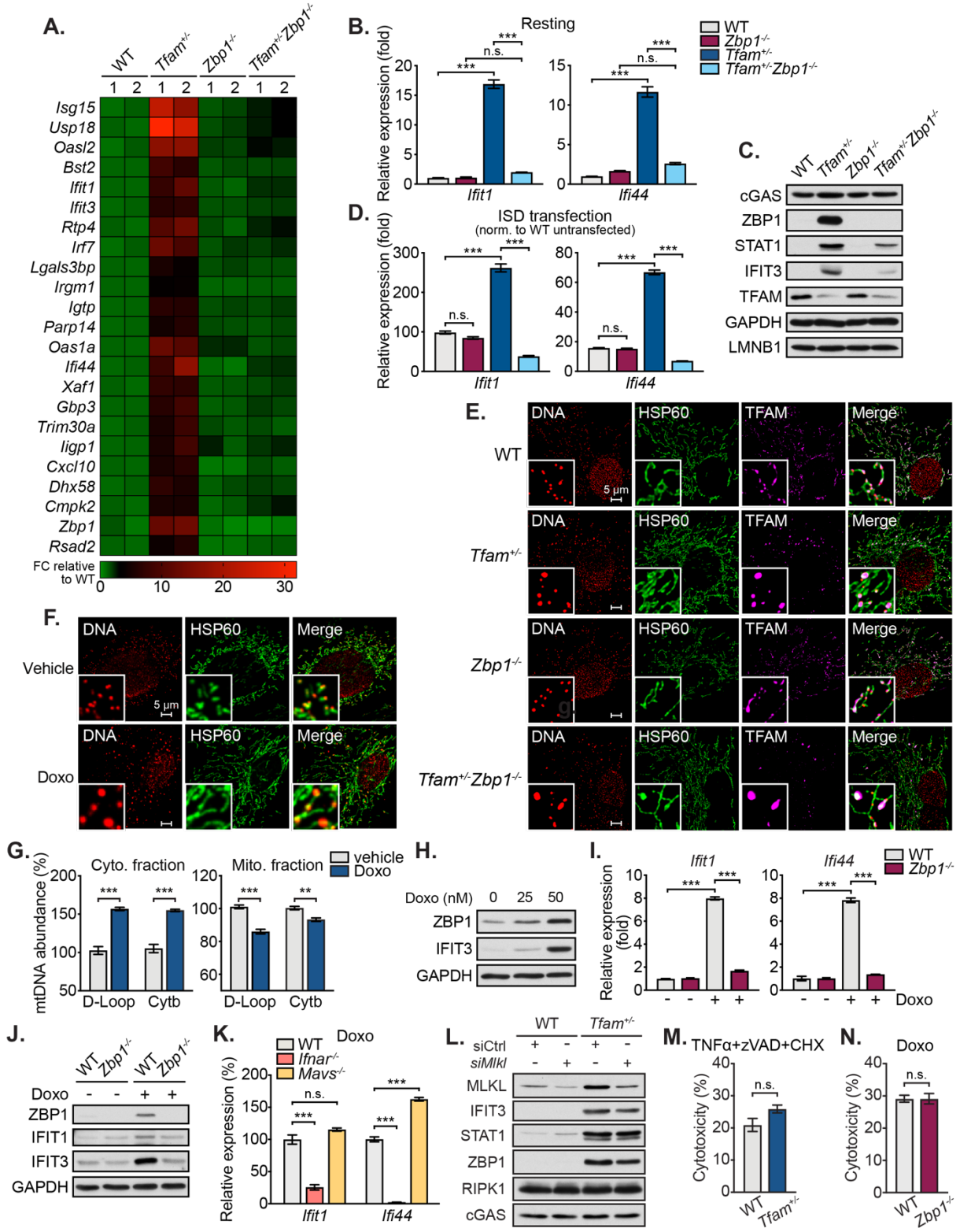
A.
WT
Tfam+/-
Zbp1-/-
Tfam+/-Zbp1-/-
Isg15
Usp18
Oasl2
Bst2
Ifit1
Ifit3
Rtp4
Irf7
Lgals3bp
Irgm1
Igtp
Parp14
Oas1a
Ifi44
Xaf1
Gbp3
Trim30a
Iigp1
Cxcl10
Dhx58
Cmpk2
Zbp1
Rsad2
FC relative to WT
B.
Resting
Relative expression (fold)
Ifit1
Ifi44
n.s.
C.
cGAS
ZBP1
STAT1
IFIT3
TFAM
GAPDH
LMNB1
D.
ISD transfection
(norm. to WT untransfected)
E.
DNA
HSP60
TFAM
Merge
5 μm
F.
Vehicle
Doxo
G.
Cyto. fraction
Mito. fraction
vehicle
Doxo
mtDNA abundance (%)
D-Loop
Cytb
H.
Doxo (nM)
0
25
50
I.
Relative expression (fold)
J.
K.
Ifnar-/-
Mavs-/-
L.
siCtrl
siMlkl
MLKL
RIPK1
M.
TNFα+zVAD+CHX
Cytotoxicity (%)
N.

1322 **Figure 1. ZBP1 is strongly induced by mtDNA stress and is essential to sustain mtDNA-**
1323 **mediated IFN-I responses, independently of cell death. A,** Heatmaps of RNA-seq data
1324 displaying the most up-regulated ISGs in WT, *Tfam*$^{+/-}$, *Zbp1*$^{-/-}$ and *Tfam*$^{+/-}$*Zbp1*$^{-/-}$ MEFs. Fold
1325 changes (FC) are normalized to the average of WT MEFs. **B, C,** qRT-PCR analysis (n = 3) (**B**)
1326 and western blots (**C**) of ISGs in resting WT, *Tfam*$^{+/-}$, *Zbp1*$^{-/-}$ and *Tfam*$^{+/-}$*Zbp1*$^{-/-}$ MEFs. **D,** qRT-
1327 PCR analysis (n = 3) of ISGs in Interferon Stimulatory DNA (ISD) transfected (2 μg/mL, 6 h) WT,
1328 *Tfam*$^{+/-}$, *Zbp1*$^{-/-}$ and *Tfam*$^{+/-}$*Zbp1*$^{-/-}$ MEFs. **E,** Representative images of WT, *Tfam*$^{+/-}$, *Zbp1*$^{-/-}$ and
1329 *Tfam*$^{+/-}$*Zbp1*$^{-/-}$ MEFs stained with anti-DNA, -HSP60 and -TFAM antibodies. Inset panels are
1330 magnified 4X. **F,** Representative confocal microscopy images of WT MEFs treated with vehicle
1331 or Doxo (500 nM, 24 h) and stained with anti-DNA and -HSP60 antibodies. Inset panels are
1332 magnified 4X. **G,** qPCR analysis (n = 3) of mtDNA abundance in cytosolic (Cyto.) and
1333 mitochondrial (Mito.) fraction from vehicle or Doxo treated WT MEFs. **H,** Western blots of ISGs
1334 in Doxo (48h) treated MEFs. **I, J,** qRT-PCR (n = 3) (**I**) and western blots (**J**) of ISGs in WT and
1335 *Zbp1*$^{-/-}$ MEFs treated with or without Doxo (50 nM, 48 h). **K,** qRT-PCR analysis (n = 3) of ISGs
1336 in WT, *Ifnar*$^{-/-}$ and *Mavs*$^{-/-}$ MEFs treated with or without Doxo (500 nM, 24h). **L,** Western blots of
1337 ISGs in WT and *Tfam*$^{+/-}$ MEFs transfected with siCtrl and si*Mlkl* for 96 h. **M,** LDH assay (n = 3)
1338 showing cytotoxicity in WT and *Tfam*$^{+/-}$ MEFs after 8 h of TNFα (25 ng/mL) + z-VAD-FMK
1339 (zVAD) (50 μM) + cycloheximide (CHX) (5 μg/mL) treatment. **N,** LDH assay (n = 3) showing
1340 cytotoxicity in WT and *Zbp1*$^{-/-}$ MEFs after 48 h of 500 nM Doxo treatment. Statistical significance
1341 was determined using analysis of variance (ANOVA) and Tukey post hoc test (**B, D, I**), or unpaired
1342 t-test (**G, K, M, N**). *P < 0.05, **P < 0.01, and ***P < 0.001. Error bars represent SEM.

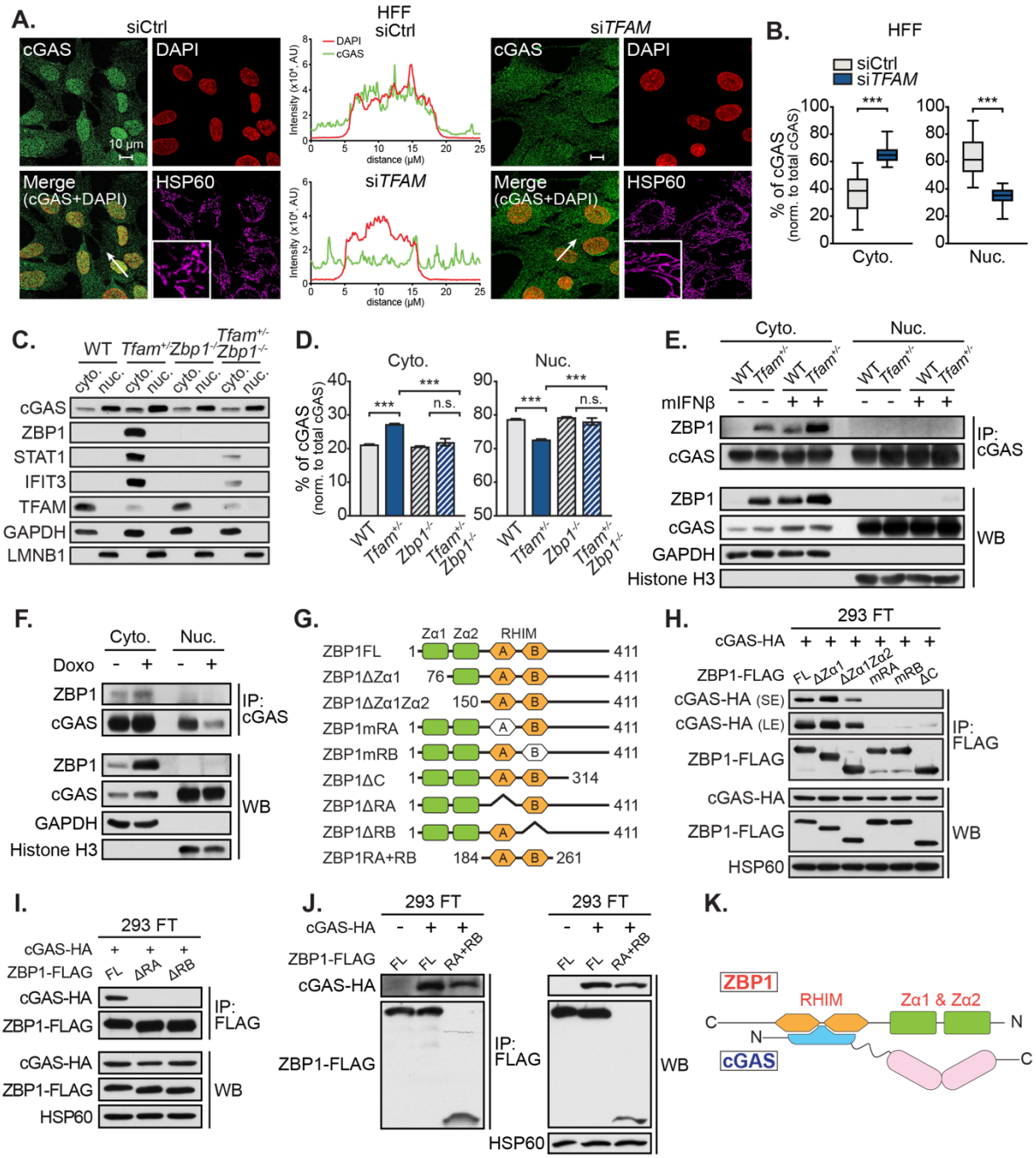
A.
siCtrl
cGAS
DAPI
10 µm
Merge (cGAS+DAPI)
HSP60
HFF siCtrl
DAPI
cGAS
Intensity (x10⁴, AU)
distance (µM)
siTFAM
B.
HFF
siCtrl
siTFAM
% of cGAS (norm. to total cGAS)
Cyto.
Nuc.
C.
WT
Tfam+/-
Zbp1-/-
Tfam+/- Zbp1-/-
cyto.
nuc.
cGAS
ZBP1
STAT1
IFIT3
TFAM
GAPDH
LMNB1
D.
Cyto.
Nuc.
% of cGAS (norm. to total cGAS)
n.s.
E.
mIFNβ
IP: cGAS
WB
Histone H3
F.
Doxo
G.
Zα1
Zα2
RHIM
ZBP1FL
ZBP1ΔZα1
ZBP1ΔZα1Zα2
ZBP1mRA
ZBP1mRB
ZBP1ΔC
ZBP1ΔRA
ZBP1ΔRB
ZBP1RA+RB
H.
293 FT
cGAS-HA
ZBP1-FLAG
cGAS-HA (SE)
cGAS-HA (LE)
IP: FLAG
HSP60
I.
ΔRA
ΔRB
J.
RA+RB
K.
ZBP1
RHIM
Zα1 & Zα2
cGAS

1343

1344 **Figure 2. ZBP1 directly interacts with cGAS and is required for cytoplasmic relocalization**
1345 **in response to mtDNA stress. A, B**, Representative images of human skin fibroblasts (HFF)
1346 transfected with Ctrl or *TFAM* siRNA for 72 h and stained with anti-cGAS and -HSP60 antibodies
1347 and DAPI (**A**). Inset panels are magnified 4X. Fluorescent intensity profiles of DAPI (red) and
1348 cGAS (green) along the white arrows are shown in the histogram. Cytosolic (Cyto.) and nuclear
1349 (Nuc.) fractions of cGAS are quantified in (**B**) (n ≥ 20 fields for each siRNA treatment). AU,
1350 arbitrary unit. **C, D,** Western blots of the cGAS and ZBP1 subcellular localizations in WT, *Tfam*$^{+/-}$,
1351 *Zbp1*$^{-/-}$ and *Tfam*$^{+/-}$*Zbp1*$^{-/-}$MEFs (**C**). Percentages of Cyto. and Nuc. cGAS are quantified in (**D**) (n
1352 = 3 different MEF lines of each genotype were used for quantification). **E,** Endogenous cytosolic
1353 and nuclear co-immunoprecipitations (co-IP) from WT and *Tfam*$^{+/-}$ MEFs with or without mouse
1354 IFNβ (mIFNβ) treatment (10 ng/mL, 6 h). **F,** Cytosolic and nuclear co-immunoprecipitation in
1355 WT MEFs with or without Doxo (50 nM, 48 h). **G,** Schematic representation of the mouse ZBP1
1356 full-length (FL), truncations and mutants used in **H-J**. **H-J,** co-IP showing interactions between
1357 mouse cGAS and mouse ZBP1 FL, truncations or mutants in 293FT. SE, short exposure; LE, long
1358 exposure. **K,** Interaction model of ZBP1 and cGAS indicating the RHIM domain of ZBP1
1359 interacting with N-terminus of cGAS. Statistical significance was determined using unpaired t-test
1360 (**B**), or analysis of variance (ANOVA) and Tukey post hoc test (**D**). *P < 0.05, **P < 0.01, and
1361 ***P < 0.001. Error bars represent SEM.
1362

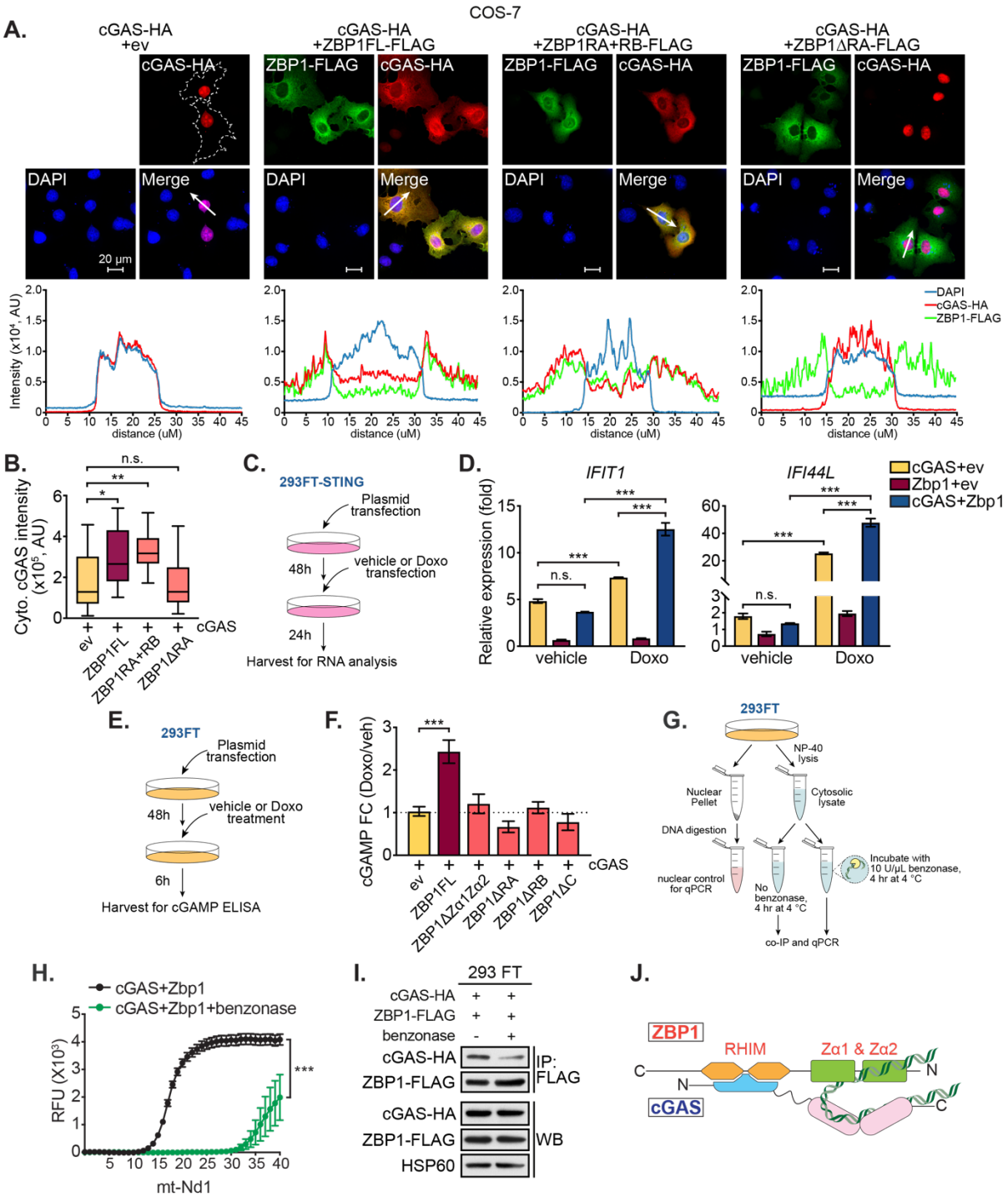
A.
COS-7
cGAS-HA +ev
cGAS-HA +ZBP1FL-FLAG
cGAS-HA +ZBP1RA+RB-FLAG
cGAS-HA +ZBP1ΔRA-FLAG
cGAS-HA
ZBP1-FLAG
DAPI
Merge
20 μm
Intensity (x10⁴, AU)
distance (uM)
DAPI
cGAS-HA
ZBP1-FLAG
B.
Cyto. cGAS intensity (x10⁵, AU)
n.s.
cGAS
ev
ZBP1FL
ZBP1RA+RB
ZBP1ΔRA
C.
293FT-STING
Plasmid transfection
48h
vehicle or Doxo transfection
24h
Harvest for RNA analysis
D.
IFIT1
IFI44L
Relative expression (fold)
cGAS+ev
Zbp1+ev
cGAS+Zbp1
vehicle
Doxo
E.
293FT
Plasmid transfection
48h
vehicle or Doxo treatment
6h
Harvest for cGAMP ELISA
F.
cGAMP FC (Doxo/veh)
cGAS
ev
ZBP1FL
ZBP1ΔZα1Zα2
ZBP1ΔRA
ZBP1ΔRB
ZBP1ΔC
G.
293FT
NP-40 lysis
Nuclear Pellet
Cytosolic lysate
DNA digestion
nuclear control for qPCR
No benzonase, 4 hr at 4 °C
Incubate with 10 U/μL benzonase, 4 hr at 4 °C
co-IP and qPCR
H.
cGAS+Zbp1
cGAS+Zbp1+benzonase
RFU (X10³)
mt-Nd1
I.
293 FT
cGAS-HA
ZBP1-FLAG
benzonase
IP: FLAG
WB
HSP60
J.
ZBP1
RHIM
Zα1 & Zα2
cGAS

1363

1364 **Figure 3. The RHIM and Z-DNA binding domains of ZBP1 are required for full activation**
1365 **of cGAS in response to mtDNA stress. A, B,** Representative images of COS-7 cells expressing
1366 indicated proteins and stained with anti-HA and -FLAG antibodies and DAPI (**A**). Fluorescent
1367 intensity profiles of DAPI (blue), HA (red) and FLAG (green) along the white arrows are shown
1368 in the histogram. Cytosolic cGAS-HA intensity is quantified in (**B**) ($n \geq 30$ fields for each group.
1369 AU, arbitrary unit). **C,** Schematic illustration of plasmid transfection and Doxo treatment in
1370 293FT-STING cells used in **D**. **D,** qRT-PCR analysis ($n = 3$) of ISGs in 293FT-STING transfected
1371 with indicated plasmids (0.4 μg/mL cGAS, 0.8 μg/mL ZBP1 or equivalent amount of empty vector)
1372 and with or without Doxo (200 nM) treatment. **E,** Schematic illustration of plasmid transfection
1373 and Doxo treatment in 293FT used in **F**. **F,** Fold change of cGAMP production in Doxo (200 nM)-
1374 treated, cGAS (0.4 μg/mL)- and ZBP1 (or empty vector, 0.8 μg/mL)-expressing 293FT compared
1375 to vehicle treated cells ($n = 10$). **G,** Schematic illustration of co-IP method used in **I**. **H,** qPCR
1376 analysis ($n = 3$) of mt-Nd1 abundance in cell lysates from **I**. RFU, relative fluorescent unit. **I,** co-
1377 IP between mouse cGAS and mouse ZBP1 in 293FT with or without benzonase treatment. **J,**
1378 Interaction model of ZBP1 and cGAS indicating the RHIM domain of ZBP1 interacting with N-
1379 terminus of cGAS, and DNA bridges the interaction. Statistical significance was determined using
1380 analysis of variance (ANOVA) (**H**) and Tukey (**B, D**), or Dunnett (**F**) post hoc test. *$P < 0.05$, **P
1381 < 0.01, and ***$P < 0.001$. Error bars represent SEM.

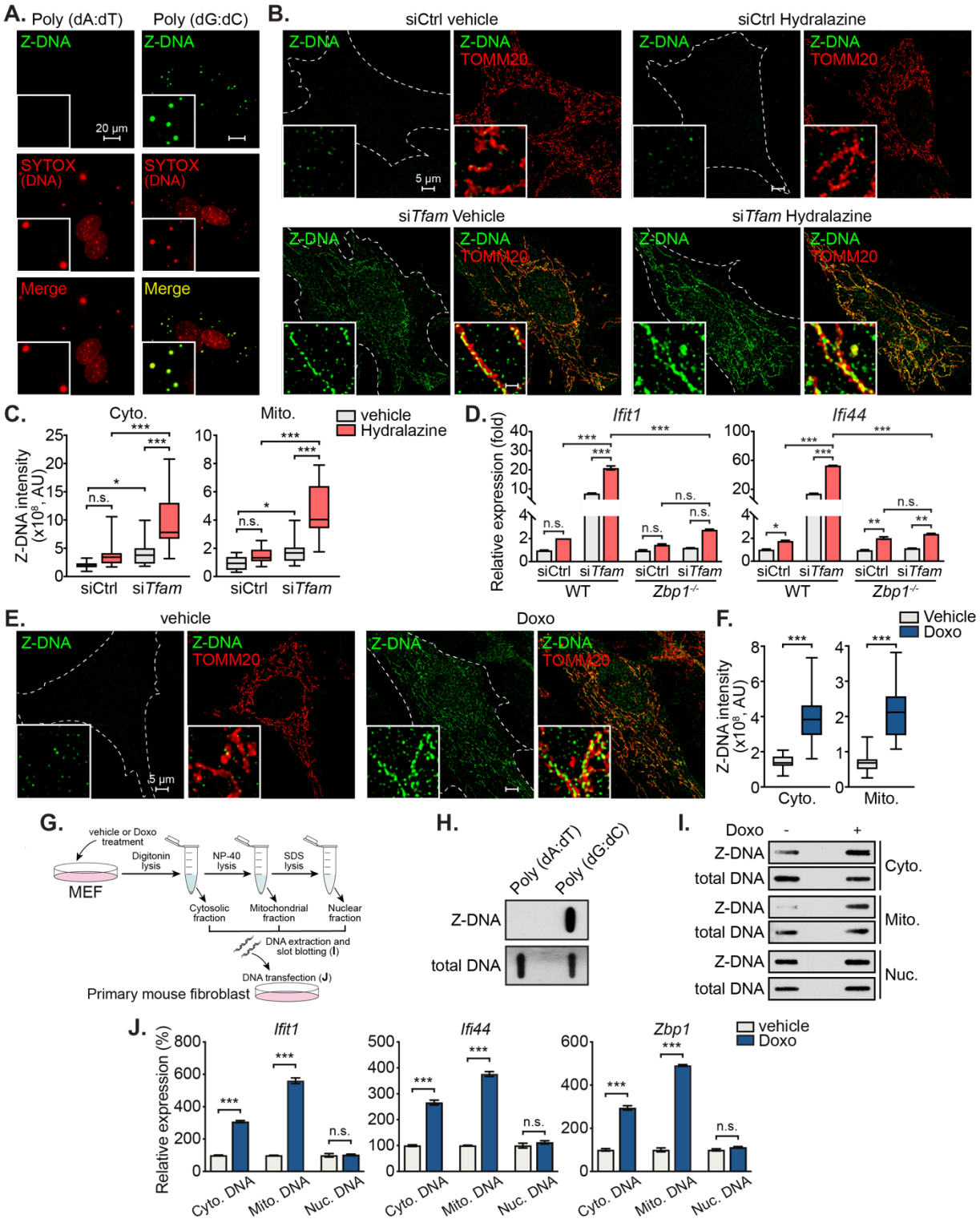
A.
Poly (dA:dT)
Poly (dG:dC)
Z-DNA
SYTOX (DNA)
Merge
20 µm
B.
siCtrl vehicle
siCtrl Hydralazine
siTfam Vehicle
siTfam Hydralazine
Z-DNA
TOMM20
5 µm
C.
Cyto.
Mito.
vehicle
Hydralazine
Z-DNA intensity (x10⁸, AU)
n.s.
siCtrl
siTfam
D.
Ifit1
Ifi44
Relative expression (fold)
WT
Zbp1-/-
E.
vehicle
Doxo
F.
Vehicle
Doxo
G.
vehicle or Doxo treatment
Digitonin lysis
NP-40 lysis
SDS lysis
MEF
Cytosolic fraction
Mitochondrial fraction
Nuclear fraction
DNA extraction and slot blotting (I)
DNA transfection (J)
Primary mouse fibroblast
H.
Poly (dA:dT)
Poly (dG:dC)
Z-DNA
total DNA
I.
Doxo
Cyto.
Mito.
Nuc.
J.
Zbp1
Relative expression (%)
Cyto. DNA
Mito. DNA
Nuc. DNA

1382

1383 **Figure 4. mtDNA stress promotes the accumulation and release of mitochondrial Z-form**
1384 **DNA that potentiates IFN-I responses. A,** Representative images of WT MEFs transfected with
1385 polyethylenimine (PEI) complexed Poly (dA:dT) (B-DNA) or Poly (dG:dC) (Z-DNA) and stained
1386 with anti-Z-DNA antibody and SYTOX. Inset panels are magnified 2.5X. **B, C,** Representative
1387 images of WT MEFs transfected with siCtrl or si*Tfam* for 72 h, treated with or without Hydralazine
1388 (100 μM) and stained with anti-Z-DNA and -TOMM20 antibodies (**B**). Inset panels are magnified
1389 4X. Cytosolic (Cyto.) and mitochondrial (Mito.) Z-DNA fluorescent intensities are quantified in
1390 (**C**) (n ≥ 20 fields for each group). **D,** qRT-PCR analysis (n = 3) of ISGs in WT and *Zbp1*$^{-/-}$ MEFs
1391 transfected with siCtrl or si*Tfam* for 72 h and treated with or without Hydralazine (100 μM) for 24
1392 h. **E, F,** Representative images of WT MEFs treated with vehicle or Doxo and stained with anti-
1393 Z-DNA and -TOMM20 antibodies (**E**). Cyto. and Mito. Z-DNA fluorescent intensities are
1394 quantified in (**F**). (n ≥ 20 fields for each group). **G,** Schematic illustration of DNA extraction and
1395 transfection from different subcellular pools in **I-J**. **H,** Slot blots of Poly (dA:dT) (B-DNA) or Poly
1396 (dG:dC) (Z-DNA) with anti-Z-DNA or anti-DNA antibody. **I,** Slot blots of cytosolic,
1397 mitochondrial, and nuclear DNA isolated from WT MEFs treated with vehicle or Doxo. **J,** qRT-
1398 PCR analysis (n = 3) of ISGs in primary mouse fibroblasts transfected with cytosolic,
1399 mitochondrial or nuclear DNA. Statistical significance was determined using analysis of variance
1400 (ANOVA) and Tukey (**C**) or Šídák (**D, J)** post hoc test, or unpaired t-test (**F**). *P < 0.05, **P <
1401 0.01, and ***P < 0.001. Error bars represent SEM.

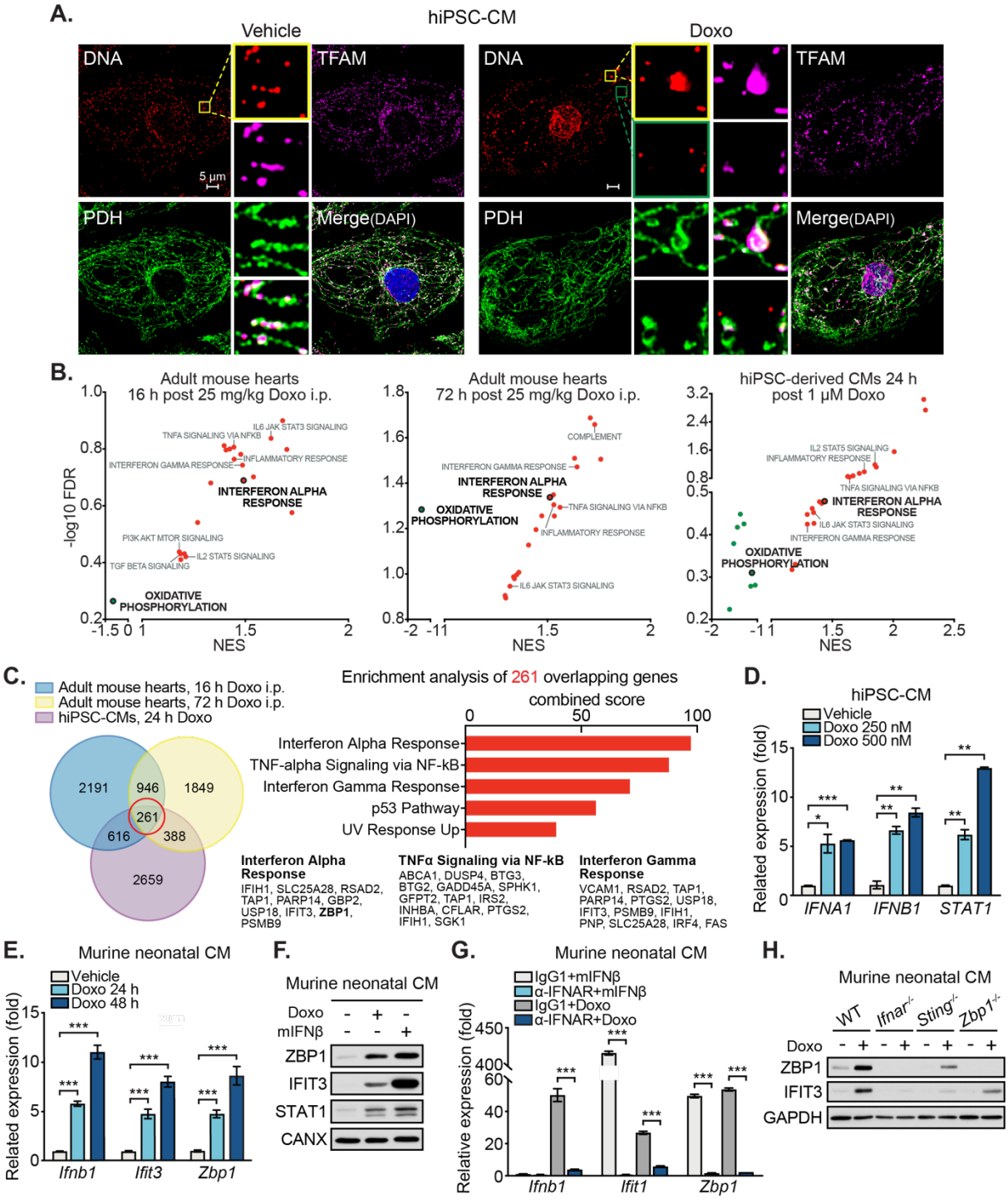
A.
hiPSC-CM
Vehicle
Doxo
DNA
TFAM
PDH
Merge(DAPI)
5 µm
B.
Adult mouse hearts
16 h post 25 mg/kg Doxo i.p.
Adult mouse hearts
72 h post 25 mg/kg Doxo i.p.
hiPSC-derived CMs 24 h
post 1 µM Doxo
-log10 FDR
NES
INTERFERON ALPHA RESPONSE
OXIDATIVE PHOSPHORYLATION
INTERFERON GAMMA RESPONSE
INFLAMMATORY RESPONSE
TNFA SIGNALING VIA NFKB
IL6 JAK STAT3 SIGNALING
IL2 STAT5 SIGNALING
PI3K AKT MTOR SIGNALING
TGF BETA SIGNALING
COMPLEMENT
C.
Adult mouse hearts, 16 h Doxo i.p.
Adult mouse hearts, 72 h Doxo i.p.
hiPSC-CMs, 24 h Doxo
2191
946
1849
261
616
388
2659
Enrichment analysis of 261 overlapping genes
combined score
Interferon Alpha Response
TNF-alpha Signaling via NF-kB
Interferon Gamma Response
p53 Pathway
UV Response Up
Interferon Alpha Response
IFIH1, SLC25A28, RSAD2, TAP1, PARP14, GBP2, USP18, IFIT3, ZBP1, PSMB9
TNFα Signaling via NF-kB
ABCA1, DUSP4, BTG3, BTG2, GADD45A, SPHK1, GFPT2, TAP1, IRS2, INHBA, CFLAR, PTGS2, IFIH1, SGK1
Interferon Gamma Response
VCAM1, RSAD2, TAP1, PARP14, PTGS2, USP18, IFIT3, PSMB9, IFIH1, PNP, SLC25A28, IRF4, FAS
D.
hiPSC-CM
Vehicle
Doxo 250 nM
Doxo 500 nM
Related expression (fold)
IFNA1
IFNB1
STAT1
E.
Murine neonatal CM
Vehicle
Doxo 24 h
Doxo 48 h
Related expression (fold)
Ifnb1
Ifit3
Zbp1
F.
Murine neonatal CM
Doxo
mIFNβ
ZBP1
IFIT3
STAT1
CANX
G.
Murine neonatal CM
IgG1+mIFNβ
α-IFNAR+mIFNβ
IgG1+Doxo
α-IFNAR+Doxo
Relative expression (fold)
Ifnb1
Ifit1
Zbp1
H.
Murine neonatal CM
WT
Ifnar-/-
Sting-/-
Zbp1-/-
Doxo
ZBP1
IFIT3
GAPDH

1402

1403 **Figure 5. Doxorubicin chemotherapy induces mtDNA stress and IFN-I responses in cardiac**
1404 **cells in vitro and in vivo. A,** Representative images of human induced pluripotent stem cell-
1405 derived cardiomyocytes (hiPSC-CMs) treated with vehicle or Doxo and stained with anti-DNA, -
1406 TFAM and -PDH antibodies and DAPI. Inset panels are magnified 7X. **B,** Volcano plots of the
1407 Gene Set Enrichment Analysis (GSEA) showing the differentially regulated pathways in 3 datasets:
1408 adult mouse hearts challenged with 25 mg/kg Doxo for 16 or 72 h vs saline controls, and hiPSC-
1409 CMs treated with 1 μM Doxo for 24 h vs controls (NES = Normalized Enrichment Score; FDR =
1410 False Discovery Rate). **C,** (left) Venn diagram of differentially expressed genes overlapping across
1411 three datasets analyzed in **B**. The top 5 pathways identified from the 261 commonly expressed
1412 genes from all three datasets (right). Shared gene lists from the top 3 pathways are shown (bottom).
1413 **D,** qRT-PCR analysis (n = 3) of ISGs in Doxo (24h) treated hiPSC-CMs. **E,** qRT-PCR analysis (n
1414 = 3) *Ifnb1* and ISGs in Doxo (250 nM) treated murine neonatal CMs. **F,** Western blots of ISGs in
1415 Doxo (500 nM, 24h) or mouse IFNβ (1 ng/mL, 4 h) treated murine neonatal CMs. **G,** qRT-PCR
1416 analysis (n = 3) of *Ifnb1* and ISGs in anti-IgG1 or -interferon receptor 1 (α-IFNAR) antibody-
1417 blocked murine neonatal CMs exposing to mouse IFNβ or Doxo. CMs were pre-treated with anti-
1418 IgG1 or -IFNAR antibody at 15 μg/mL for 5 h before subjecting to IFNβ (1 ng/mL, 4 h) or Doxo
1419 (500 nM, 24h) treatment. **H,** Western blots of ISGs in Doxo (500 nM, 24h) treated WT, *Ifnar*$^{-/-}$,
1420 *Sting*$^{-/-}$ and *Zbp1*$^{-/-}$ murine neonatal CMs. Statistical significance was determined using unpaired
1421 t-test (**D, E, G**). *P < 0.05, **P < 0.01, and ***P < 0.001. Error bars represent SEM.

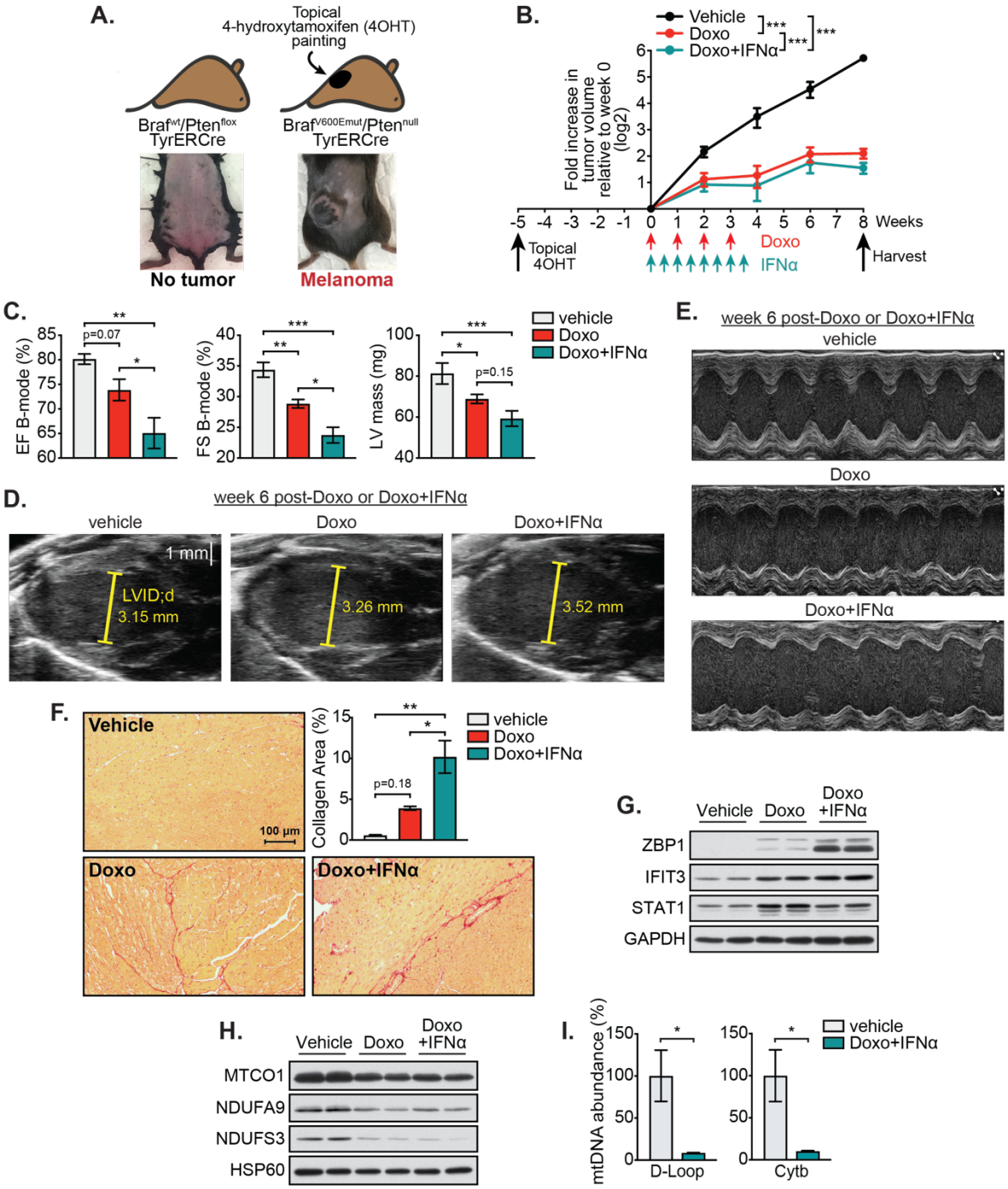
A.
Topical
4-hydroxytamoxifen (4OHT)
painting
Braf^wt/Pten^flox
TyrERCre
Braf^V600Emut/Pten^null
TyrERCre
No tumor
Melanoma
B.
Vehicle
Doxo
Doxo+IFNα
Fold increase in tumor volume relative to week 0 (log2)
Weeks
Topical 4OHT
Doxo
IFNα
Harvest
C.
EF B-mode (%)
FS B-mode (%)
LV mass (mg)
p=0.07
p=0.15
vehicle
Doxo
Doxo+IFNα
D.
week 6 post-Doxo or Doxo+IFNα
vehicle
Doxo
Doxo+IFNα
1 mm
LVID;d
3.15 mm
3.26 mm
3.52 mm
E.
week 6 post-Doxo or Doxo+IFNα
vehicle
Doxo
Doxo+IFNα
F.
Vehicle
Doxo
Doxo+IFNα
100 µm
Collagen Area (%)
p=0.18
vehicle
Doxo
Doxo+IFNα
G.
Vehicle
Doxo
Doxo +IFNα
ZBP1
IFIT3
STAT1
GAPDH
H.
Vehicle
Doxo
Doxo +IFNα
MTCO1
NDUFA9
NDUFS3
HSP60
I.
mtDNA abundance (%)
D-Loop
Cytb
vehicle
Doxo+IFNα

1422

1423 **Figure 6. Adjuvant IFNα synergizes with Doxorubicin to enhance cardiac and mitochondrial**
1424 **dysfunction in tumor-bearing mice. A,** Schematic illustration of melanoma induction. **B,**
1425 Primary melanoma volume of each treated group measured every other week starting from 5 weeks
1426 post 4OHT induction. Mice were i.p. injected with 5 mg/kg Doxo once a week for 4 weeks.
1427 Recombinant mouse IFNα was administered twice weekly for 4 weeks via i.p. injection of 20,000
1428 U per dose. **C,** Left ventricular EF, FS, and mass at week 4 were calculated from parasternal long
1429 axis B-mode. (n = 5 per group). **D, E,** Representative parasternal long axis (**D**) and short axis (**E**)
1430 images from each treatment at week 6 post vehivle, Doxo or Doxo+IFNα challenge. **F,**
1431 Representative Picrosirius Red staining images of heart sections from vehicle-, Doxo- and
1432 Doxo+IFNα treat melanoma mice. Collagen area of each group are quantified and shown at up-
1433 right corner. **G,** Western blots (n = 2) of ISGs in cardiac extracts from vehicle, Doxo and
1434 Doxo+IFNα challenged tumor-bearing mice at week 8. **H, I,** Western blots of mitochondrial
1435 OXPHOS components (n = 2) (**H**) and qPCR analysis (n = 3) of mtDNA abundance (**I**) in cardiac
1436 extracts from vehicle, Doxo and Doxo+IFNα challenged tumor-bearing mice at week 8. Statistical
1437 significance was determined using analysis of variance (ANOVA) and Tukey post hoc test (**B, C,**
1438 **F**) or unpaired t-test (**I**). *P < 0.05, **P < 0.01, and ***P < 0.001. Error bars represent SEM.

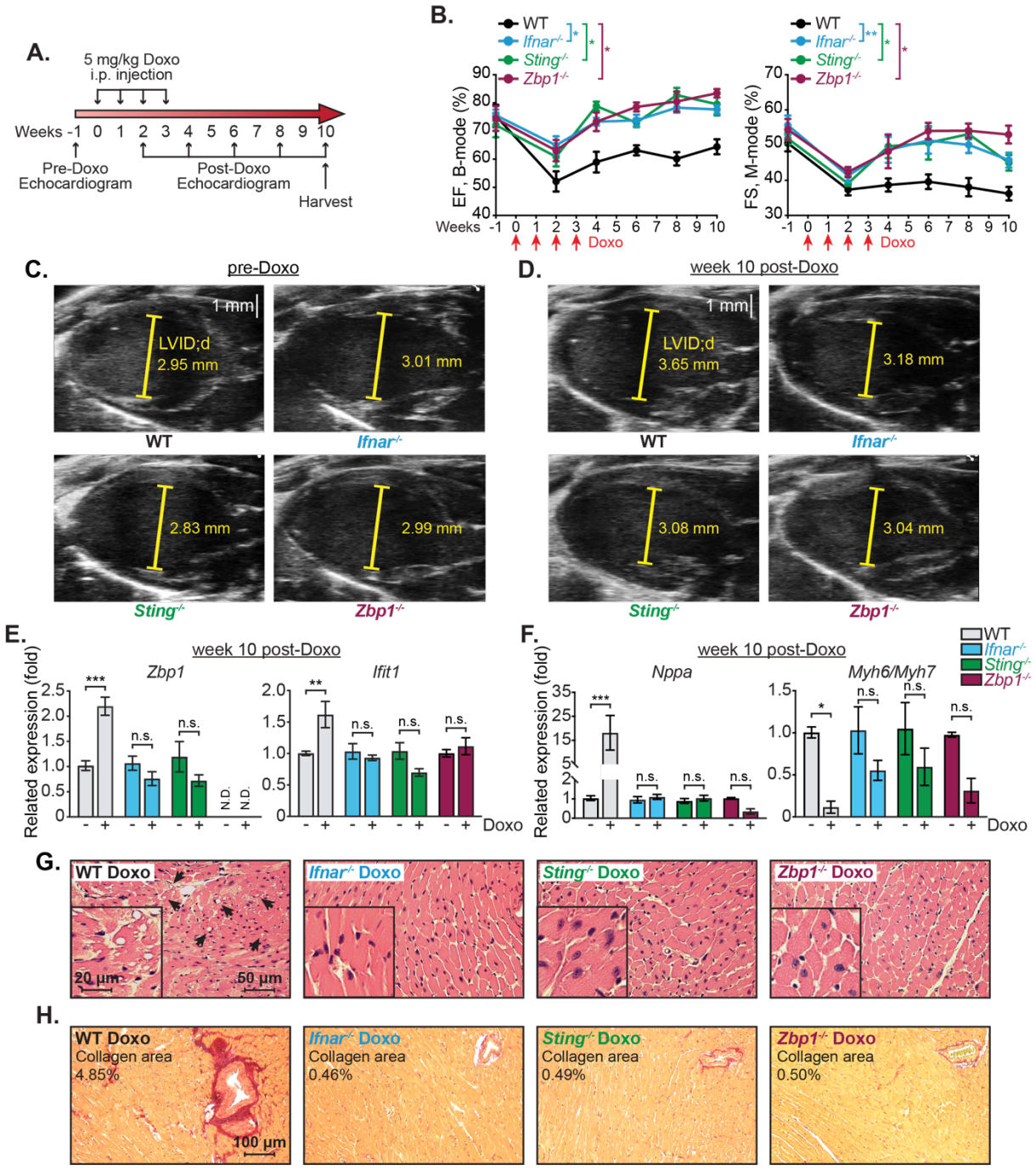
A.
5 mg/kg Doxo
i.p. injection
Weeks -1 0 1 2 3 4 5 6 7 8 9 10
Pre-Doxo
Echocardiogram
Post-Doxo
Echocardiogram
Harvest
B.
WT
Ifnar-/-
Sting-/-
Zbp1-/-
EF, B-mode (%)
FS, M-mode (%)
Weeks
Doxo
C.
pre-Doxo
1 mm
LVID;d
2.95 mm
3.01 mm
2.83 mm
2.99 mm
D.
week 10 post-Doxo
LVID;d
3.65 mm
3.18 mm
3.08 mm
3.04 mm
E.
week 10 post-Doxo
Zbp1
Ifit1
Related expression (fold)
N.D.
Doxo
F.
week 10 post-Doxo
Nppa
Myh6/Myh7
Related expression (fold)
Doxo
G.
WT Doxo
Ifnar-/- Doxo
Sting-/- Doxo
Zbp1-/- Doxo
20 µm
50 µm
H.
WT Doxo
Collagen area
4.85%
Ifnar-/- Doxo
Collagen area
0.46%
Sting-/- Doxo
Collagen area
0.49%
Zbp1-/- Doxo
Collagen area
0.50%
100 µm

1439

1440 **Figure 7. The ZBP1-STING-IFN-I axis is a novel driver of chemotherapy-related heart**
1441 **failure. A,** Doxo i.p. challenge regimen, longitudinal cardiac monitoring, and cardiac harvest
1442 timepoint diagram. **B,** Left ventricular ejection fraction (EF) and fractional shortening (FS)
1443 calculated from B-mode or M-mode images using Vevo Lab software (n = 6 per genotype). **C, D,**
1444 Representative parasternal long axis images from each genotype pre-Doxo (**C**) and at week 10 post
1445 Doxo challenge (**D**). **E, F,** qRT-PCR analysis of ISGs (**E**) or atrial natriuretic peptides *Nppa* and
1446 the *Myh6/7* expression ratio (**F**) in vehicle- or Doxo-treat WT, *Ifnar*$^{-/-}$, *Sting*$^{-/-}$ and *Zbp1*$^{-/-}$ cardiac
1447 extracts. (n = 3 per genotype per treatment). **G,** Representative H&E staining of heart sections
1448 from 10-week post Doxo WT, *Ifnar*$^{-/-}$, *Sting*$^{-/-}$ and *Zbp1*$^{-/-}$ mice. Arrows indicate significant
1449 cardiomyocyte vacuolization in Doxo-treated WT heart section. **H,** Representative Picrosirius Red
1450 staining images of heart sections from 10-week post WT, *Ifnar*$^{-/-}$, *Sting*$^{-/-}$ and *Zbp1*$^{-/-}$ mice.
1451 Percentages of fibrosis (Collagen area) are shown. Statistical significance was determined using
1452 analysis of variance (ANOVA) and Dunnett (**B**) or Šídák (**E,F**) post hoc test. *P < 0.05, **P <
1453 0.01, and ***P < 0.001. Error bars represent SEM.

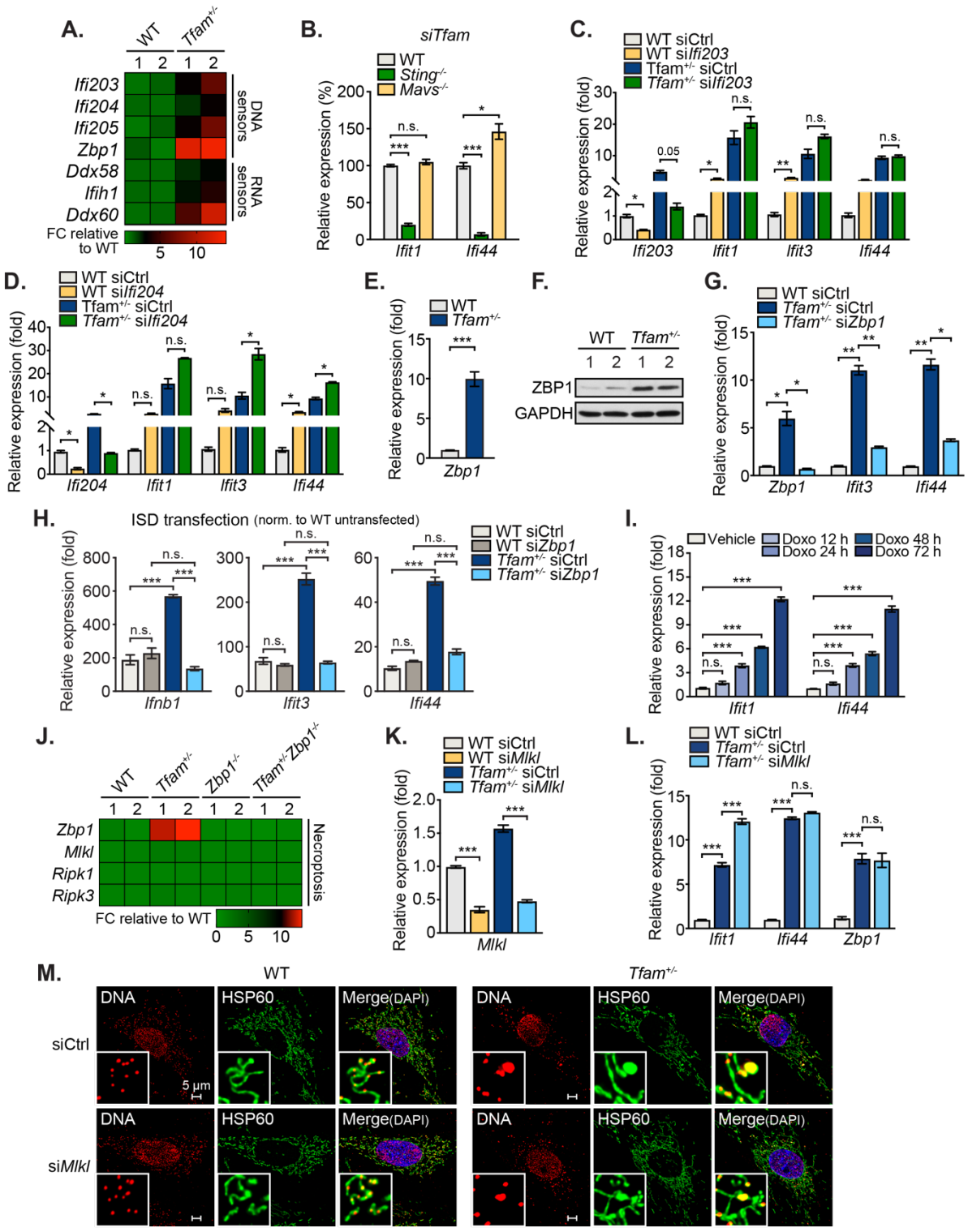
A.
WT
Tfam+/-
1 2 1 2
Ifi203
Ifi204
Ifi205
Zbp1
Ddx58
Ifih1
Ddx60
DNA sensors
RNA sensors
FC relative to WT
5 10
B.
siTfam
WT
Sting-/-
Mavs-/-
Relative expression (%)
Ifit1
Ifi44
C.
WT siCtrl
WT siIfi203
Tfam+/- siCtrl
Tfam+/- siIfi203
Relative expression (fold)
Ifi203
Ifit1
Ifit3
Ifi44
D.
WT siCtrl
WT siIfi204
Tfam+/- siCtrl
Tfam+/- siIfi204
Relative expression (fold)
Ifi204
Ifit1
Ifit3
Ifi44
E.
WT
Tfam+/-
Relative expression (fold)
Zbp1
F.
WT
Tfam+/-
ZBP1
GAPDH
G.
WT siCtrl
Tfam+/- siCtrl
Tfam+/- siZbp1
Relative expression (fold)
Zbp1
Ifit3
Ifi44
H.
ISD transfection (norm. to WT untransfected)
WT siCtrl
WT siZbp1
Tfam+/- siCtrl
Tfam+/- siZbp1
Relative expression (fold)
Ifnb1
Ifit3
Ifi44
I.
Vehicle
Doxo 12 h
Doxo 24 h
Doxo 48 h
Doxo 72 h
Relative expression (fold)
Ifit1
Ifi44
J.
WT
Tfam+/-
Zbp1-/-
Tfam+/-Zbp1-/-
1 2 1 2 1 2 1 2
Zbp1
Mlkl
Ripk1
Ripk3
Necroptosis
FC relative to WT
0 5 10
K.
WT siCtrl
WT siMlkl
Tfam+/- siCtrl
Tfam+/- siMlkl
Relative expression (fold)
Mlkl
L.
WT siCtrl
Tfam+/- siCtrl
Tfam+/- siMlkl
Relative expression (fold)
Ifit1
Ifi44
Zbp1
M.
WT
Tfam+/-
siCtrl
siMlkl
DNA
HSP60
Merge(DAPI)
5 µm

1454

1455 **Figure S1. ZBP1 mediates mtDNA stress-induced IFN-I responses independently of MLKL.**
1456 **A,** Heatmaps of RNA-seq data displaying up-regulated DNA and RNA sensors in WT and *Tfam*$^{+/-}$
1457 MEFs. Fold changes (FC) are normalized to the average of WT MEFs. **B,** qRT-PCR analysis (n =
1458 3) of ISGs in WT, *Sting*$^{-/-}$ and *Mavs*$^{-/-}$ MEFs transfected with siCtrl, siTfam for 72 h. **C,D,** qRT-
1459 PCR analysis (n = 3) of ISGs in WT and *Tfam*$^{+/-}$ MEFs transfected with siCtrl, si*Ifit203* (**C**) or
1460 si*Ifi204* (**D**) for 72 h. **E, F,** qRT-PCR analysis (n = 3) (**E**) and western blots (n = 2) (**F**) of Zbp1
1461 expression in WT and *Tfam*$^{+/-}$ MEFs. **G, H,** qRT-PCR analysis (n = 3) of ISGs in resting (**G**) or
1462 ISD transfected (2 μg/mL, 6 h) (**H**) WT and *Tfam*$^{+/-}$ MEFs transfected with siCtrl or si*Zbp1* for 96
1463 h. **I,** qRT-PCR analysis (n = 3) of ISGs in Doxo (125 nM) treated MEFs. **J,** Heatmaps of RNA-
1464 seq data displaying necroptosis mediator variations in WT, *Tfam*$^{+/-}$, *Zbp1*$^{-/-}$ and *Tfam*$^{+/-}$*Zbp1*$^{-/-}$
1465 MEFs. Fold changes (FC) are normalized to the average of WT MEFs. **K, L,** qRT-PCR analysis
1466 (n = 3) of *Mlkl* (**K**) or ISG (**L**) expression in WT and *Tfam*$^{+/-}$ MEFs transfected with siCtrl and
1467 si*Mlkl* for 96 h. **M,** Representative fluorescence images of WT and *Tfam*$^{+/-}$ MEFs transfected with
1468 siCtrl and si*Mlkl* for 96 h and stained with anti-DNA and -HSP60 antibodies and DAPI. Inset
1469 panels are magnified 4X. Statistical significance was determined using analysis of variance
1470 (ANOVA) and Tukey post hoc test (**C-D, G-I, K-L**) or unpaired t-test (**B, D**). *P < 0.05, **P <
1471 0.01, and ***P < 0.001. Error bars represent SEM.

1472

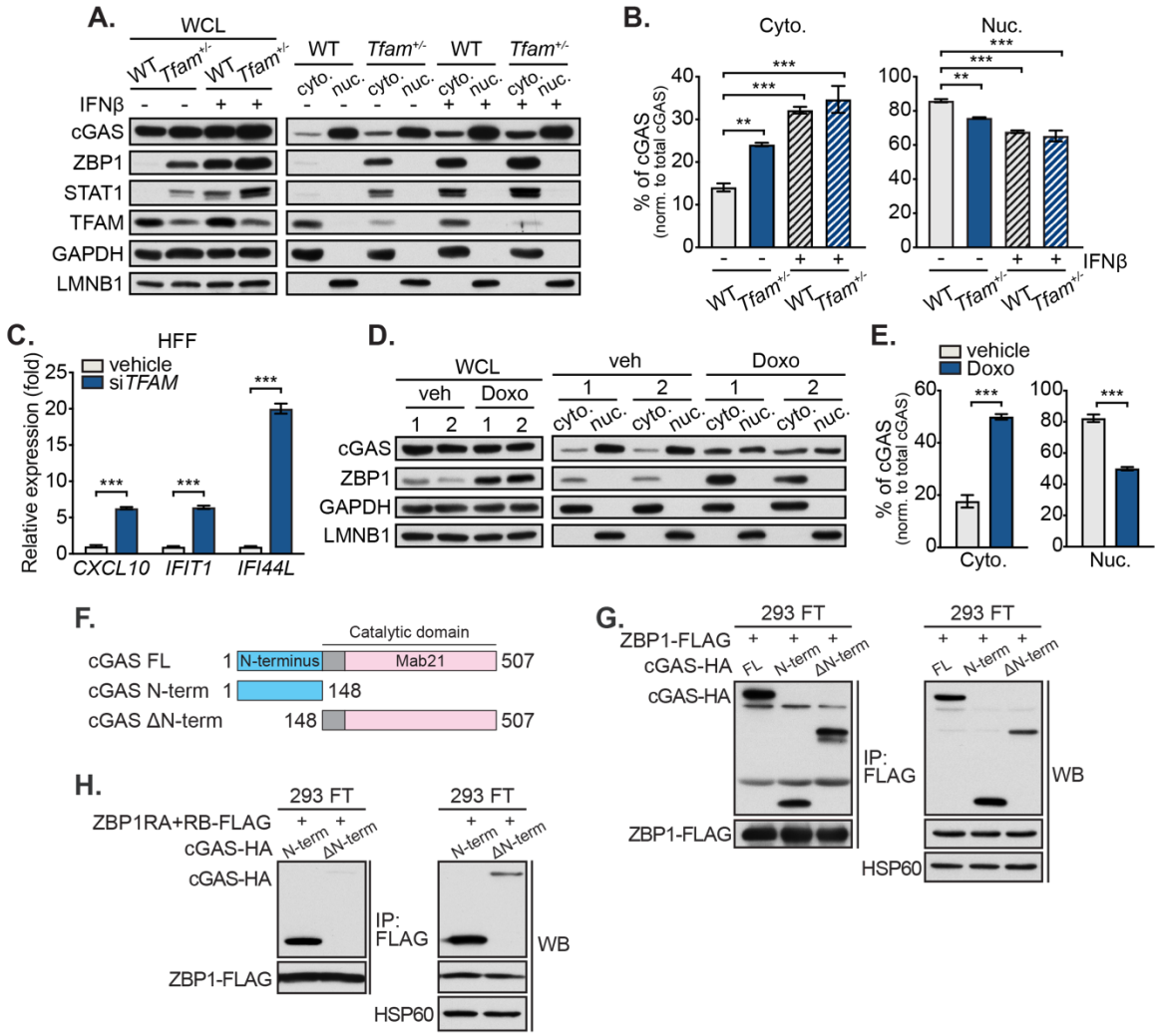
A.
WCL
WT
Tfam+/-
IFNβ
cGAS
ZBP1
STAT1
TFAM
GAPDH
LMNB1
cyto.
nuc.
B.
Cyto.
Nuc.
% of cGAS
(norm. to total cGAS)
IFNβ
C.
HFF
vehicle
siTFAM
Relative expression (fold)
CXCL10
IFIT1
IFI44L
D.
WCL
veh
Doxo
E.
vehicle
Doxo
F.
Catalytic domain
cGAS FL
N-terminus
Mab21
cGAS N-term
cGAS ΔN-term
G.
293 FT
ZBP1-FLAG
cGAS-HA
FL
N-term
ΔN-term
IP:
FLAG
WB
HSP60
H.
ZBP1RA+RB-FLAG

1473

1474 **Figure S2. Cytoplasmic localization of cGAS is dependent on direct binding to ZBP1. A, B,**
1475 Western blots of cytosolic (Cyto.) and nuclear (Nuc.) proteins in WT and *Tfam*$^{+/-}$ MEFs with or
1476 without IFNβ treatment (10 ng/mL, 6 h) (**A**). Percentages of cytosolic and nuclear cGAS in WT
1477 and *Tfam*$^{+/-}$ MEFs are quantified in (**B**). 4 different MEF lines of each genotype were used for
1478 quantification. **C,** qRT-PCR analysis (n = 3) of ISGs in HFF transfected with Ctrl or *TFAM* siRNA
1479 for 72 h. **D, E,** Western blots of cytosolic and nuclear proteins in vehicle (veh) or 50 nM
1480 Doxorubicin (Doxo) treated WT MEFs (**D**). Percentages of cytosolic and nuclear cGAS in vehicle
1481 or Doxo treated WT MEFs are quantified in (**E**). 2 different MEF lines are shown in the western
1482 blots, n = 3 different MEF lines were used for quantification. **F,** Schematic representation of the
1483 mouse cGAS full-length (FL) and truncations used in **G-H**. **G, H,** co-IP showing interactions
1484 between mouse ZBP1 and mouse cGAS FL and truncations in 293FT. Statistical significance was
1485 determined using analysis of variance (ANOVA) and Tukey (**B**) post hoc test or unpaired t-test (**C,**
1486 **E**). *P < 0.05, **P < 0.01, and ***P < 0.001. Error bars represent SEM.

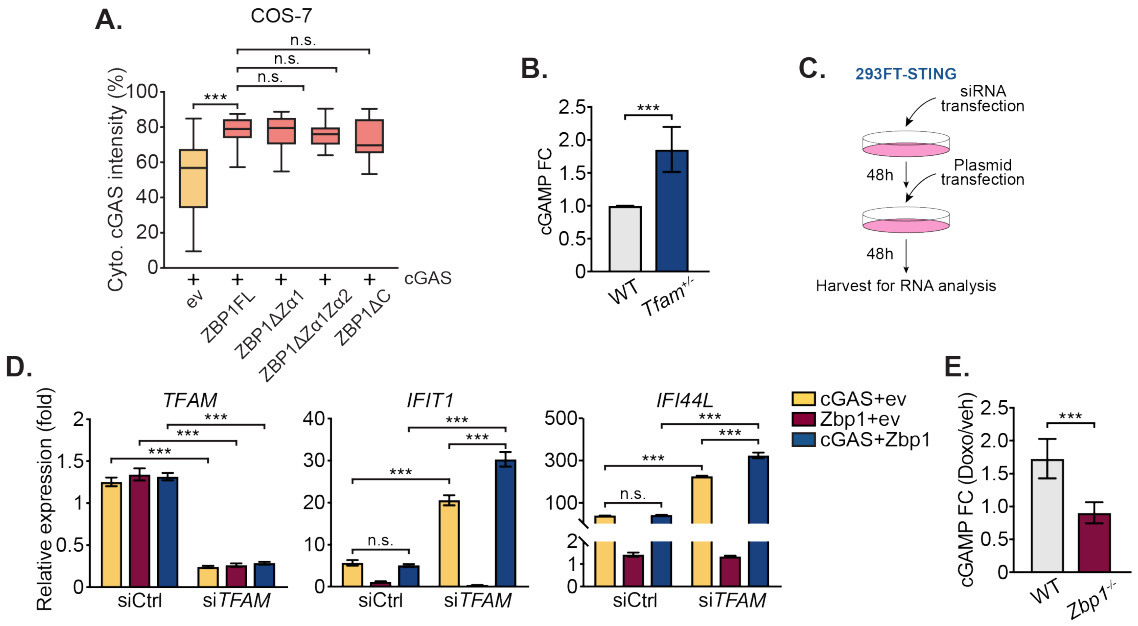
A.
COS-7
Cyto. cGAS intensity (%)
n.s.
n.s.
n.s.
***
cGAS
ev
ZBP1FL
ZBP1ΔZα1
ZBP1ΔZα1Zα2
ZBP1ΔC
B.
cGAMP FC
***
WT
Tfam+/-
C.
293FT-STING
siRNA transfection
48h
Plasmid transfection
48h
Harvest for RNA analysis
D.
Relative expression (fold)
TFAM
IFIT1
IFI44L
cGAS+ev
Zbp1+ev
cGAS+Zbp1
siCtrl
siTFAM
n.s.
E.
cGAMP FC (Doxo/veh)
WT
Zbp1-/-

1487

1488 **Figure S3. Complexing with ZBP1 enhances cGAS activity in the cytosol. A,** Percentages of
1489 cytosolic cGAS intensity in COS-7 transfected with indicated plasmid (n ≥ 30 fields for each
1490 group). **B,** Fold change (FC) of cGAMP production in *Tfam*$^{+/-}$ MEFs compared to WT MEFs (n =
1491 6). **C,** Schematic illustration of siRNA and plasmid transfection in 293FT-STING used in **D**. **D,**
1492 qRT-PCR analysis (n = 3) of ISGs in 293FT-STING transfected with indicated siRNA and plasmid
1493 (0.25 μg/mL cGAS, 0.25 μg/mL ZBP1 or equivalent amount of empty vector). **E,** Fold change of
1494 cGAMP production in Doxo-treated WT and *Zbp1*$^{-/-}$ MEFs compared to vehicle treated cells (n =
1495 6). Statistical significance was determined using analysis of variance (ANOVA) and Tukey post
1496 hoc test (**A, D**), or unpaired t-test (**B, E**). *P < 0.05, **P < 0.01, and ***P < 0.001. Error bars
1497 represent SEM.

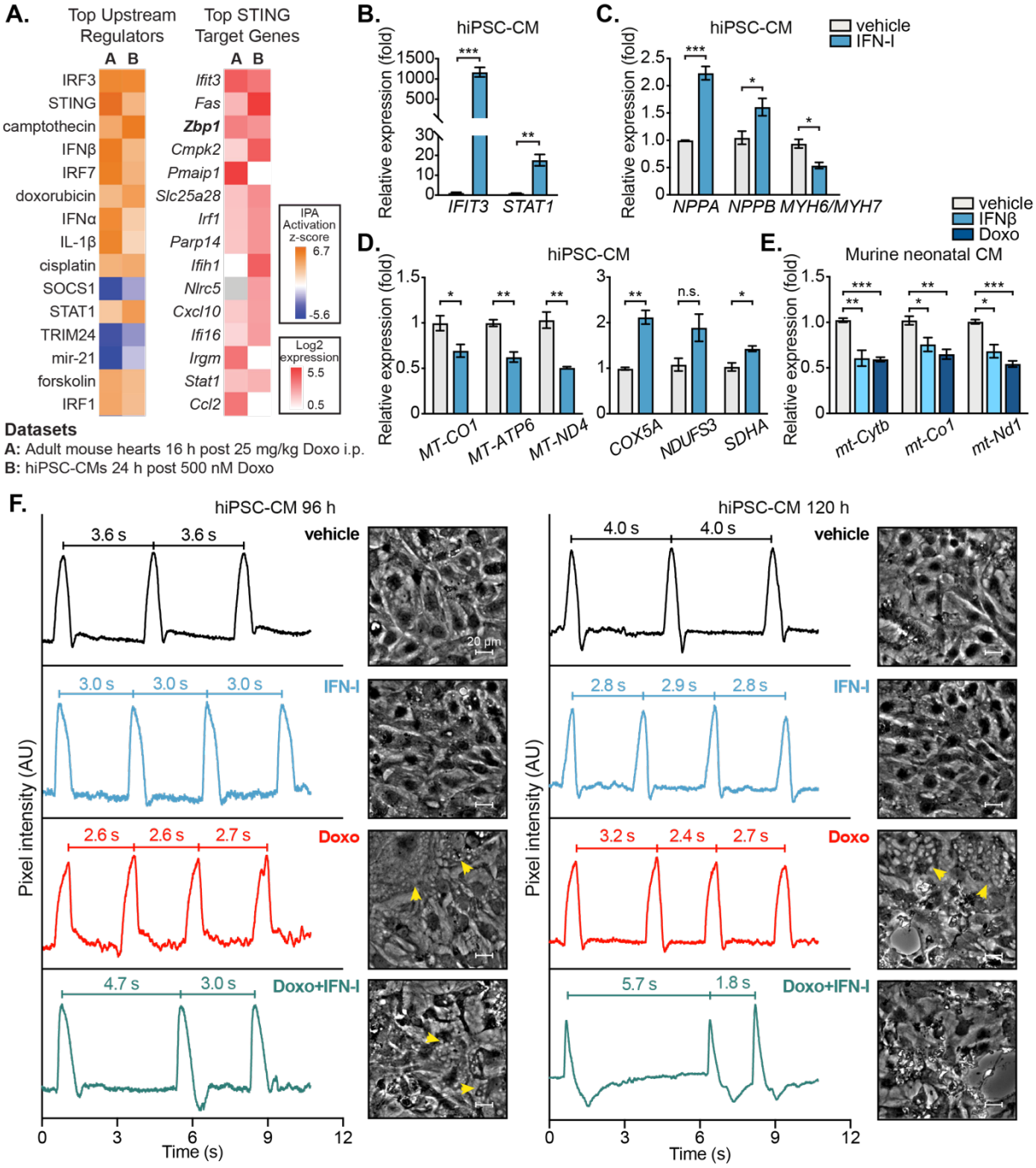
A.
Top Upstream Regulators
Top STING Target Genes
A B
IRF3
STING
camptothecin
IFNβ
IRF7
doxorubicin
IFNα
IL-1β
cisplatin
SOCS1
STAT1
TRIM24
mir-21
forskolin
IRF1
Ifit3
Fas
Zbp1
Cmpk2
Pmaip1
Slc25a28
Irf1
Parp14
Ifih1
Nlrc5
Cxcl10
Ifi16
Irgm
Stat1
Ccl2
IPA Activation z-score
6.7
-5.6
Log2 expression
5.5
0.5
Datasets
A: Adult mouse hearts 16 h post 25 mg/kg Doxo i.p.
B: hiPSC-CMs 24 h post 500 nM Doxo
B.
hiPSC-CM
Relative expression (fold)
IFIT3
STAT1
C.
hiPSC-CM
vehicle
IFN-I
NPPA
NPPB
MYH6/MYH7
D.
hiPSC-CM
vehicle
IFNβ
Doxo
MT-CO1
MT-ATP6
MT-ND4
COX5A
NDUFS3
SDHA
n.s.
E.
Murine neonatal CM
mt-Cytb
mt-Co1
mt-Nd1
F.
hiPSC-CM 96 h
hiPSC-CM 120 h
vehicle
IFN-I
Doxo
Doxo+IFN-I
3.6 s
3.0 s
2.6 s
4.7 s
4.0 s
2.8 s
3.2 s
5.7 s
1.8 s
20 µm
Pixel intensity (AU)
Time (s)

1498

1499 **Figure S4. Type I interferons and Doxorubicin synergize to imbalance cardiomyocyte**
1500 **mitochondrial gene expression and disrupt contractility. A,** Ingenuity Pathway Analysis (IPA)
1501 analysis of top upstream regulators and the most enriched STING target genes from adult mouse
1502 hearts challenged with 25 mg/kg Doxo for 16 h vs saline controls and hiPSC-CMs treated with 1
1503 μM Doxo for 24 h vs controls datasets. White indicates no change in expression and gray indicates
1504 $p < 0.05$ for a given gene. IPA Z-score > 2 or < -2 is significant. **B-D,** qRT-PCR analysis (n = 3)
1505 of ISGs (**B**) cardiac damage markers (**C**) and mitochondrial DNA- or nuclear DNA-encoded
1506 mitochondrial transcripts (**D**) in hiPSC-CMs treated with or without human recombinant IFNα (10
1507 ng/mL) and IFNβ (10 ng/mL) for 96 h. **E,** qRT-PCR analysis (n = 3) of mitochondrial DNA-
1508 encoded mitochondrial transcripts in murine neonatal CMs treated with mouse IFNβ (1 ng/mL) or
1509 Doxo (500 nM) for 24h. **F,** Camera-capture assay showing CM beat periodicity and images of
1510 hiPSC-CMs after indicated treatments (100 nM Doxo and/or 10 ng/mL of both human recombinant
1511 IFNα and IFNβ) for 96 h and 120 h. Yellow arrows indicate cardiomyocyte vacuolization. AU,
1512 arbitrary unit. Statistical significance was determined using unpaired t-test (**B-E**). *P < 0.05, **P
1513 < 0.01, and ***P < 0.001. Error bars represent SEM.

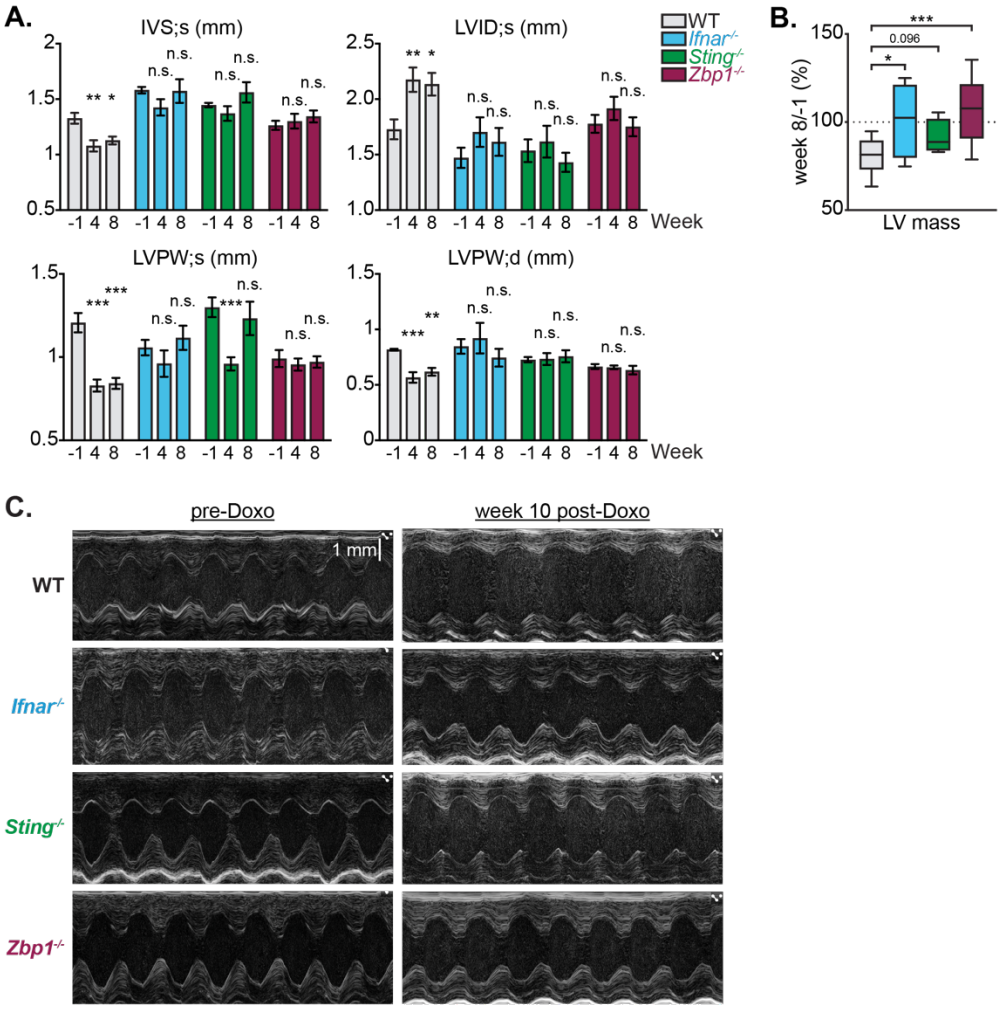
A.
IVS;s (mm)
LVID;s (mm)
LVPW;s (mm)
LVPW;d (mm)
WT
Ifnar-/-
Sting-/-
Zbp1-/-
Week
n.s.
B.
week 8/-1 (%)
LV mass
0.096
C.
pre-Doxo
week 10 post-Doxo
1 mm

1514

1515 **Figure S5. Doxorubicin disrupts cardiac structure and function in a ZBP1-STING-IFNAR-**
1516 **dependent manner. A,** Left ventricle wall thickness and internal diameter measurements were
1517 made pre-Doxo (week -1) and at week 4 and 8 weeks post challenge in short axis M-mode (n = 6
1518 of *Ifnar*$^{-/-}$ and *Sting*$^{-/-}$ groups, n = 12 of WT and *Zbp1*$^{-/-}$ groups). **B,** Heart weight changes in WT,
1519 *Ifnar*$^{-/-}$, *Sting*$^{-/-}$ and *Zbp1*$^{-/-}$ mice at week 8 compared to pre-Doxo treatment (week -1) (n = 6 of
1520 *Ifnar*$^{-/-}$ and *Sting*$^{-/-}$ groups, n = 12 of WT and *Zbp1*$^{-/-}$ groups). **C,** Representative short axis images
1521 from each genotype pre- and 10 weeks post- Doxo treatment. Statistical significance was
1522 determined using analysis of variance (ANOVA) and Tukey post hoc test (**A**), or unpaired t-test
1523 (**B**). *P < 0.05, **P < 0.01, and ***P < 0.001. Error bars represent SEM.

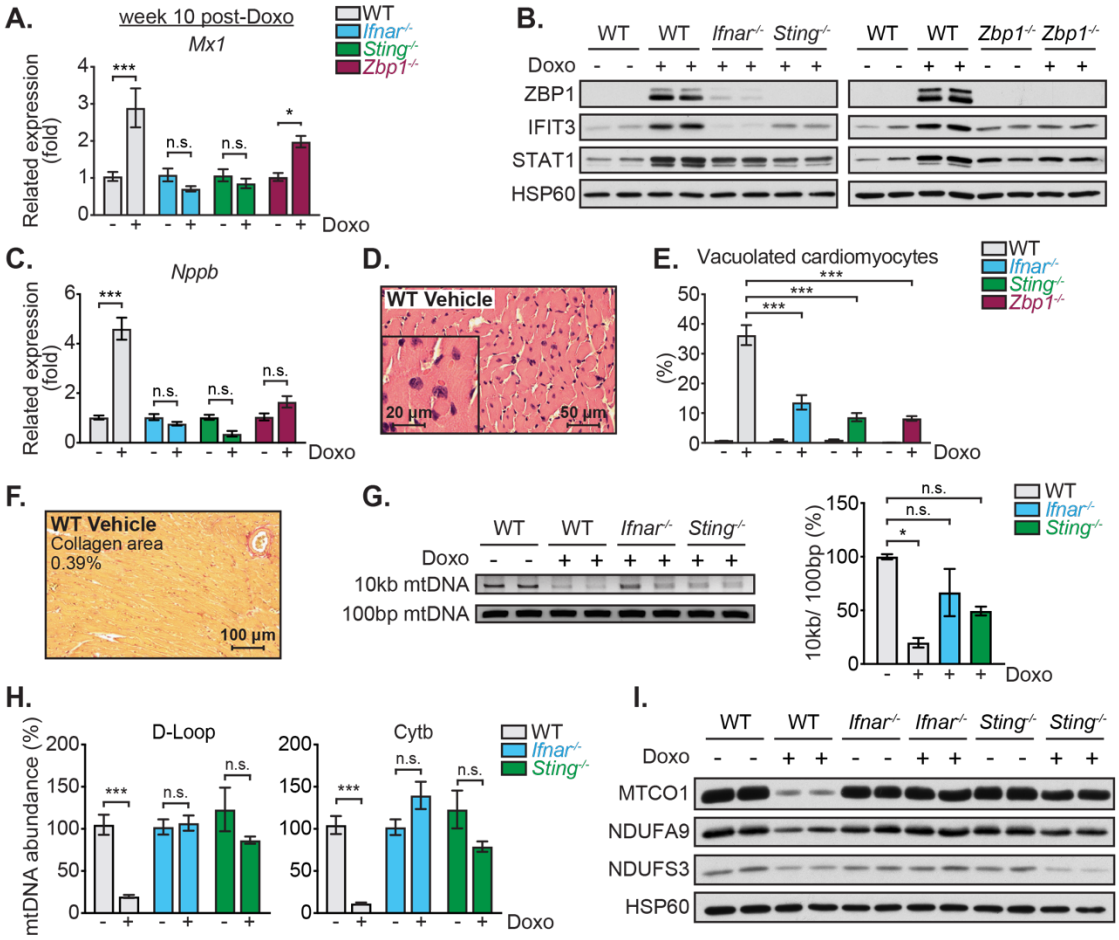
A.
week 10 post-Doxo
Mx1
Related expression (fold)
WT
Ifnar-/-
Sting-/-
Zbp1-/-
Doxo
B.
WT
Ifnar-/-
Sting-/-
Zbp1-/-
Doxo
ZBP1
IFIT3
STAT1
HSP60
C.
Nppb
Related expression (fold)
Doxo
D.
WT Vehicle
20 µm
50 µm
E.
Vacuolated cardiomyocytes
(%)
Doxo
F.
WT Vehicle
Collagen area
0.39%
100 µm
G.
Doxo
10kb mtDNA
100bp mtDNA
10kb/ 100bp (%)
Doxo
H.
D-Loop
Cytb
mtDNA abundance (%)
Doxo
I.
Doxo
MTCO1
NDUFA9
NDUFS3
HSP60

1524

1525 **Figure S6. Doxorubicin-induced ISG expression, cardiac fibrosis, and mitochondrial**
1526 **dysfunction are lessened in the absence of ZBP1-STING-IFNAR signaling. A, B,** qRT-PCR
1527 analysis (n = 3 per genotype per treatment) (**A**) or western blots (n = 2 per genotype per treatment)
1528 (**B**) of ISGs in cardiac extracts 10 weeks post Doxo challenge. **C,** Relative cardiac expression of
1529 atrial natriuretic peptides *Nppb* in RNA extracts 10 weeks post Doxo challenge (n = 3 per genotype
1530 per treatment). **D,** Representative H&E staining of heart sections from vehicle-treated WT mice
1531 10 weeks after the initial challenge. **E,** Percentages of cardiomyocytes exhibiting vacuolization
1532 from WT, *Ifnar*$^{-/-}$, *Sting*$^{-/-}$ and *Zbp1*$^{-/-}$ heart sections with or without Doxo challenge (n = 4 fields
1533 from 3 mice per genotype per treatment). **F,** Representative Picrosirius Red staining images of
1534 vehicle-treated WT heart sections 10 weeks after the initial challenge. Percentages of fibrosis
1535 (Collagen area) are shown. **G,** 10 kb and 100 bp (control) mtDNA fragments PCR (n = 2 per
1536 genotype per treatment) of vehicle- and Doxo-treated WT, *Ifnar*$^{-/-}$ and *Sting*$^{-/-}$ mice. Densitometry
1537 was used to calculate the 10 kb/100 bp ratio (bottom). **H,** qPCR analysis (n = 3 per genotype per
1538 treatment) of mtDNA abundance in cardiac extracts from vehicle- and Doxo- treated WT, *Ifnar*$^{-/-}$
1539 and *Sting*$^{-/-}$ mice. **I,** Western blots (n = 2 per genotype per treatment) of mitochondrial OXPHOS
1540 subunits in cardiac extracts from vehicle- and Doxo-treated WT, *Ifnar*$^{-/-}$ and *Sting*$^{-/-}$ mice.
1541 Statistical significance was determined using analysis of variance (ANOVA) and Šídák (**A, C, H**)
1542 or Tukey (**E, G**) post hoc test. *P < 0.05, **P < 0.01, and ***P < 0.001. Error bars represent SEM.
1543

1544 **KEY RESOURCES TABLES**

Table 1. Oligonucleotides used in cloning

Plasmid	Forward and reverse Oligo. sequences
p3xFLAG-CMV-14-Zbp1 FL	ATGCGTGAATTCGCCACCATGGCAGAAGCTCCTGTTGA ATGCGTGGATCCTTGCTTGCTCAGTCCTGTGT
p3xFLAG-CMV-14-Zbp1 ΔRHIMA	AACAGCCACTGTGGTGAGCCAGGTCCCAGGA CTCACCACAGTGGCTGTTGATGTGGCTGTTG
p3xFLAG-CMV-14-Zbp1 ΔRHIMB	GGAGCTCAGGCAGGGAAGCACCCCTCTTATA CTTCCCTGCCTGAGCTCCGTGGGCAACAGGG
p3xFLAG-CMV-14-Zbp1 RHIMA+B	ATGCGTGAATTCGCCACCATGATCTCCATTGCCAATTC ATGCGTGGATCCATCCCCCACGAGGCTCATCT
pcDNA3.1-cGAS FL-HA	ATGCGTGCGGCCGCGCCACCATGGAAGATCCGCGTAGAAG ATGCGTCTCGAGTCAAGCGTAATCTGGAACATCGTATGGG-TAAAGCTTGTCAAAAATTGGAA
pcDNA3.1-cGAS N-term-HA	ATGCGTGCGGCCGCGCCACCATGGAAGATCCGCGTAGAAG ATGCGTCTCGAGTCAAGCGTAATCTGGAACATCGTATGGG-TAGTCCGGTTCCTTCCTGGA
pcDNA3.1-cGAS ΔN-term-HA	ATGCGTGCGGCCGCGCCACCATGGACAAGCTAAAGAAGGTGCT ATGCGTCTCGAGTCAAGCGTAATCTGGAACATCGTATGGG-TAAAGCTTGTCAAAAATTGGAA
pMXs-IRES-Blast-STING-HIS	ATGCGTCTCGAGGCCACCATGCCATACTCCAACCTG AACGCTGCGGCCGCTTAGTGGTGGTGGTGGTGGTGGAT-GAGGTCAGTGCGGA

1545

Table 2. Dicer substrate siRNA used

Gene	Oligo. Sequence
Control	rCrGrUrUrArArUrCrGrCrGrUrArUrArCrGrCrGrUAT rArUrArCrGrCrGrUrArUrUrArUrArCrGrCrGrArUrUrArArCrGrArC
Tfam	rGrCrUrArUrCrCrArArArGrArArArCrCrUrArUrGrArGrUTC rGrArArCrUrCrArUrArGrGrUrUrUrCrUrUrUrGrGrArUrArGrCrUrA
TFAM	rGrCrArGrArArCrUrCrArUrCrUrArGrGrUrArArArUrUrACA rUrGrUrArArUrUrUrArCrCrUrArGrArUrGrArGrUrUrCrUrGrCrCrU
Ifi203	rArArCrUrCrArGrUrUrCrUrUrCrUrGrArArUrCrUrCrUrUTT rArArArArGrArGrArUrUrCrArGrArArGrArArCrUrGrArGrUrUrCrA
Ifi204	rCrUrGrArArArArCrArArUrUrGrArCrArGrGrCrArArCrCAA rUrUrGrGrUrUrGrCrCrUrGrUrCrArArUrUrGrUrUrUrUrCrArGrGrU
Zbp1	rArUrCrArArGrUrCrCrUrUrUrArCrCrGrCrCrUrGrArArGAA rUrUrCrUrUrCrArGrGrCrGrGrUrArArArGrGrArCrUrUrGrArUrUrG
Mlkl	rArUrCrArUrUrGrGrArArUrArCrCrGrUrUrUrCrArGrArUGT rArCrArUrCrUrGrArArArCrGrGrUrArUrUrCrCrArArUrGrArUrArA

*27-mers synthesized by Integrated DNA Technologies (IDT), 10 nmol, standard desalting. For working solution, diluted to 20 μM in nuclease-free duplex buffer (IDT, 11-05-01-12).

1546

Table 3. Oligonucleotides used in qPCR for mouse samples

Gene	Forward and reverse Oligo. sequences
Ifnb1	CCCTATGGAGATGACGGAGA CCCAGTGCTGGAGAAATTGT
Ifit1	CAAGGCAGGTTTCTGAGGAG GACCTGGTCACCATCAGCAT
Ifit3	TTCCCAGCAGCACAGAAAC AAATTCCAGGTGAAATGGCA
Ifi44	CTGATTACAAAAGAAGACATGACAGAC AGGCAAAACCAAAGACTCCA
Zbp1	TCAAAGGGTGAAGTCATGGA GTGGAGTGGCTTCAGAGCTT
Mx1	TCTGAGGAGAGCCAGACGAT ACTCTGGTCCCCAATGACAG
Ifi203	TCCAGAATCCTCATAAGTCTCCA TGGTACAGTTCCTCTCCTTGGT
Ifi204	GCCAGCCCTAAGATCTGTGAT TCTTTCGGTTCACTGTTTTCTTG
Mlkl	CCTCTGTGGACGGTAGGAGT TGGATTCTTCAACCGCAGA
Tnfa	CCACCACGCTCTTCTGTCTAC AGGGTCTGGGCCATAGAACT
Il6	TGATGCACTTGCAGAAAACA ACCAGAGGAAATTTTCAATAGGC
Nppa	AGCCGAGACAGCAAACATCAG CAAAAGGCCAGGAAGAGGAAG
Nppb	CAGCTCTTGAAGGACCAAGG AGAGACCCAGGCAGAGTCAG
Myh6	CATCGACCTCATCGAGAAGC GCCTTGAAGGTCATGTCTGAG
Myh7	GATGTTTTTGTGCCCGATGA TGTCGAACTTGGGTGGGTT
mt-Cytb	AGTAGACAA AGCCACCTTGA CCGCGATAATAAATGGTAAG
mt-Co1	GCCCCAGATATAGCATTCCC GTTCATCCTGTTCCTGCTCC
mt-Nd1	CACCTACCCTATCACTCACACTAGC GGCTCATCCTGATCATAGAATGGAG
Rpl37	CATCCTTTGGTAAGCGTCGCA TGGCACTCCAGTTATACTTCCT
mtDNA D-Loop	AATCTACCATCCTCCGTGAAACC TCAGTTTAGCTACCCCCAAGTTTAA
mtDNA Cytb	GCTTTCCACTTCATCTTACCATTTA TGTTGGGTTGTTTGATCCTG
nucDNA Tert	CTAGCTCATGTGTCAAGACCCTCTT GCCAGCACGTTTCTCTCGTT

1547

Table 4. Oligonucleotides used in qPCR for human sample

Gene	Forward and reverse Oligo. sequences
IFNA1	CCCTCTCTTTATCAACAAACTTGC TTGTTTTCATGTTGGACCAGA
IFNB1	CTTTCGAAGCCTTTGCTCTG CAGGAGAGCAATTTGGAGGA
CXCL10	CACCATGAATCAAACTGCGA GCTGATGCAGGTACAGCGT
IFIT1	GCAGCCAAGTTTTACCGAAG GCCCTATCTGGTGATGCAGT
IFIT3	TGGGAACAGCAGAGACACAG AAGTTCCAGGTGAAATGGCA
IFI44L	CAATTTAAGCCTGATCTAACCCC CAGTTGCGCAGATGATTTTC
STAT1	AGGAAGACCCAATCCAGATGT TGAATATTCCCCGACTGAGC
NPPA	CAGGATGGACAGGATTGGAG TCCTCCCTGGCTGTTATCTTC
NPPB	GATGGTGCAAGGGTCTGG TAATGCCGCCTCAGCACT
MYH6	CTCAAGCTCATGGCCACTCT GCCTCCTTTGCTTTTACCACT
MYH7	CCATCCCCACTTTGTACGTT ACCAGGGGGTTGTCCATC
MT-CO1	TTAGCTGACTCGCCACAGTC GGCCACCTACGGTGAAAAGA
MT-ATP6	TCATTCAACCAATAGCCCTGG GCCTGCAGTAATGTTAGCGGT
MT-ND4	CCTAAAGCCCATGTCGAAGC TGCGGCAAGTACTATTGACCC
COX5A	GAGGCCTCCTGCACTCC GCGAGCATCAAACTCCTCAT
NDUFS3	ACAGATTATGGCTTCGAGGG ACCCGCTTCACTTCATCATC
SDHA	AAACTCGCTCTTGGACCTGG TCTTCCCCAGCGTTTGGTTT
TFAM	CCAAAAAGACCTCGTTCAGC TCCAGTTTTCCTTTACAGTCTTCAG
RPL37	AGTGCCTTCTCTTCCGGTCT TTCCAAACGATGACGTTCC
mtDNA ND1	GAACTAGTCTCAGGCTTCAACATCG CTAGGAAGATTGTAGTGGTGAGGGTG
nucDNA 18s	CTTAGAGGGACAAGTGGCG ACGCTGAGCCAGTCAGTGTA

1548

Table 5. Antibody dilution and application

Name	Company	Cat. #	Dilution	Application
IFIT3	Gift from G. Sen at Cleveland Clinic		1:5000	WB
cGAS	Cell Signaling Technology	31659	1:1000	WB
cGAS	Cell Signaling Technology	D1D3G	1:200	IF
STAT1	Cell Signaling Technology	9172	1:1000	WB
MLKL	Cell Signaling Technology	37705	1:1000	WB
GAPDH	Proteintech	60004-1	1:20000	WB
Histone H3	Proteintech	17168-1-AP	1:1000	WB
LMNB1	Proteintech	66095-1	1:1000	WB
HA	Proteintech	51064-2-AP	1:1000/1:600	WB/IF
TFAM	Proteintech	22586-1-AP	1:200	IF
CANX	Proteintech	10427-2-AP	1:1000	WB
TFAM	Millipore	MABT166	1:1000/1:200	WB/IF
DNA	Millipore	CBL186	1:300/1:250	IF/SB
TOMM20	Millipore	MABT166	1:200	IF
FLAG	Millipore	F1804	1:4000/1:800	WB/IF
PDH	Abcam	ab110333	1:800	IF
RIP	BD Biosciences	610458	1:1000	WB
ZBP1	Adipogen	AG-20B-0010-C100	1:1000	WB
HSP60	Santa Cruz Biotechnology	N-20	1:2000/1:300	WB/IF
Z-DNA	absolute	Ab00783-23.0	1:1000	SB
Z-DNA	Capralogics	P00008	1:200	IF
MTCO1	ThermoFisher Scientific	459600	1:1000	WB
NDUFA9	ThermoFisher Scientific	459100	1:1000	WB
NDUFS3	ThermoFisher Scientific	459130	1:1000	WB

1549 *WB: western blot; IF: immunofluorescence; SB: slot blot